A MODEL SYSTEM TO GIVE AN INSIGHT INTO THE BEHAVIOUR OF GOLD NANOPARTICLES UNDER ION IRRADIATION

Yaasiin Ramjauny

▶ **To cite this version:**

Yaasiin Ramjauny. A MODEL SYSTEM TO GIVE AN INSIGHT INTO THE BEHAVIOUR OF GOLD NANOPARTICLES UNDER ION IRRADIATION. Materials Science [cond-mat.mtrl-sci]. Ecole Polytechnique X, 2010. English. NNT : . pastel-00565145

HAL Id: pastel-00565145
https://pastel.hal.science/pastel-00565145

Submitted on 11 Feb 2011

HAL is a multi-disciplinary open access archive for the deposit and dissemination of scientific research documents, whether they are published or not. The documents may come from teaching and research institutions in France or abroad, or from public or private research centers.

L'archive ouverte pluridisciplinaire **HAL**, est destinée au dépôt et à la diffusion de documents scientifiques de niveau recherche, publiés ou non, émanant des établissements d'enseignement et de recherche français ou étrangers, des laboratoires publics ou privés.

PhD THESIS OF THE ECOLE POLYTECHNIQUE

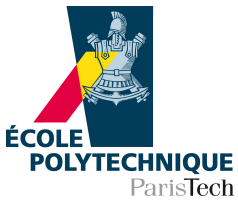

Specialization
PHYSICS

Presented by
Yaasiin RAMJAUNY

To obtain the degree of
DOCTOR OF THE ECOLE POLYTECHNIQUE

Title of the thesis:

A MODEL SYSTEM TO GIVE AN INSIGHT INTO THE BEHAVIOUR OF GOLD NANOPARTICLES UNDER ION IRRADIATION

Defended in public on 7 July 2010
with the following thesis committee:

GACOIN Thierry	President
THOME Lionel	Reviewer
BEAUFORT Marie-France	Reviewer
MONNET Isabelle	Examiner
BONAFOS Caroline	Examiner
DUNLOP Annie	Supervisor
RIZZA Giancarlo	Co-supervisor

Thesis completed at Laboratoire des Solides Irradiés
Ecole Polytechnique, Palaiseau

PhD THESIS OF THE ECOLE POLYTECHNIQUE

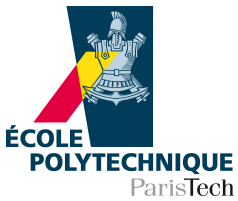

Specialization
PHYSICS

Presented by
Yaasiin RAMJAUNY

To obtain the degree of
DOCTOR OF THE ECOLE POLYTECHNIQUE

Title of the thesis:

A MODEL SYSTEM TO GIVE AN INSIGHT INTO THE BEHAVIOUR OF GOLD NANOPARTICLES UNDER ION IRRADIATION

Defended in public on 7 July 2010
with the following thesis committee:

GACOIN Thierry	President
THOME Lionel	Reviewer
BEAUFORT Marie-France	Reviewer
MONNET Isabelle	Examiner
BONAFOS Caroline	Examiner
DUNLOP Annie	Supervisor
RIZZA Giancarlo	Co-supervisor

Thesis completed at Laboratoire des Solides Irradiés
Ecole Polytechnique, Palaiseau

A toute ma famille,

Remerciements

Dans le cadre de ce travail je voudrais remercier :

- Guillaume Petite, ancien directeur du Laboratoire des Solides Irradiés (LSI), pour m'avoir accueilli et permis d'effectuer cette thèse.

- Martine Soyer, directrice du LSI, qui a remarquablement bien repris la direction du laboratoire. Je tiens en particulier à souligner ses implications dans la vie du laboratoire. A ce titre, j'ai personnellement apprécié les journées des doctorants qu'elle a mises en place afin de créer une meilleure cohésion entre les divers groupes du laboratoire. De plus, je tiens personnellement à la remercier pour son soutien, tant moral qu'administratif, durant la période délicate que j'ai traversé à la fin de ma thèse.

- Giancarlo Rizza, mon co-directeur de thèse, qui m'a suivi depuis mon stage de master jusqu'à la fin de ce travail de thèse. J'ai pu obtenir avec lui une première vision de la recherche scientifique sur un sujet particulièrement passionnant. J'ai beaucoup apprécié les longues discussions scientifiques que nous avons eues. Nous avons la même envie de vouloir comprendre dans les moindres détails comment évolue un système . Par ses conseils, il m'a énormément appris sur la manière d'organiser un travail scientifique, de la pratique expérimentale à l'écriture d'un manuscrit. Il a également su m'apporter beaucoup de son temps et son soutien dans les moments où j'en avais besoin afin de franchir toutes les étapes que comporte un tel travail.

- Annie Dunlop, ma directrice de thèse, pour sa gentillesse, ses conseils et pour son soutien durant toutes ces années.

- Gérard Jaskierowicz, qui nous a malheureusement quittés. Je lui suis reconnaissant pour sa gentillesse ainsi que tous les précieux conseils et l'aide qu'il m'a apporté pour l'utilisation du microscope électronique et du PIPS.

- Thierry Gacoin, du laboratoire PMC, qui m'a beaucoup aidé lors de mes diverses manipulations en chimie. J'ai appris à apprécier la chimie à sa juste valeur. Je le remercie pour sa disponibilité et sa gentillesse.

- Laetitia Vieille, du laboratoire PMC, qui m'a beaucoup aidé à lors de la synthèses de nanoparticules. Je la remercie entre autres pour tout le temps qu'elle m'a consacré en chimie, pour sa patience et pour sa gentillesse.

- Sandrine Perruchas, du laboratoire PMC, qui a toujours été disponible à chaque fois que j'avais besoin d'aide. Je la remercie notamment pour son assistance concernant la synthèse et le dépôt de la silice sol-gel, mais également pour la correction de mon manuscrit, pour tous ses précieux conseils, et pour sa gentillesse.

- Sylvain Henry du laboratoire CNSNM d'Orsay, pour ses explications sur le fonctionnement de l'accélérateur ARAMIS et pour son aide et ses conseils lors des irradiations.

- Marc Hayoun avec qui j'ai passé de très bons moments à développer le code de calcul du type Monte-Carlo cinétique. De cette collaboration, est née une passion pour les calculs numériques. Je laisse cependant une parenthèse ouverte concernant les bugs informatiques.

- Vincent Metayer pour son aide lors des recuits sur mes nombreux échantillons.

- Farah Attouchi pour sa gentillesse et son dévouement à effectuer certaines synthèses dont la tâche me revenait au moment où je n'étais plus apte à me rendre au laboratoire. Pour son aide afin de visualiser mes échantillons au microscope électronique à balayage.

- Daniel Caldemaison, pour son aide lors de l'utilisation du microscope électronique à balayage du laboratoire LMS..

- Gerrit Coddens pour toutes les discussions scientifiques et ses conseils, ainsi que pour les bons moments et les fous rires que j'ai eus lorsque je partageais son bureau. J'ai été particulièrement assidu à tous ses cours et à tous ses discours.

- Peter Vajda, pour sa gentillesse, sa sagesse et tous les conseils qu'il a su me donner.

- Bruno Boizot, pour les discussions concernant les défauts dans les verres, et pour tous ses conseils concernant la correction de mon manuscrit.

- Andréa Cucca, pour toute son aide technique.

- Pierre Lombard, pour toute son aide technique concernant les installations de divers logiciels.

- Nadège Ollier, pour toutes les discussions et ses conseils apportés.

- Ekaterina Antoshchenkova, pour tous ses conseils et renseignements.

Contents

List of Tables

List of Figures

Chapter 1

General Introduction

1.1 Ion-matter interaction

1.1.1 Equilibrium charge

When an ion penetrates into a matrix, it acquires an equilibrium charge Z_1^*. This charge results from the interactions of the impinging particle with the target atoms, [1]. Considering the velocity of the ion, two extreme regimes can be identified:

i) when the ion velocity v is less than the Bohr velocity of the atomic electrons, v_0 (v$\ll$v$_0$), the impinging particle captures electrons becoming neutral.

ii) when v is larger than v_0 (v$\gg$v$_0$) the incoming ion looses its electrons through excitation and ionization processes. The impinging particle becomes bared, and can be considered as punctual charge, Z_1e.

For intermediate ion velocities, i.e. $v\sim v_0$, the processes of electronic capture comes into concurrence with those of the electronic loss. The result is the creation of an equilibrium charge, $Z_1^*(v)$, whose value is related to the ion velocity.

1.1.2 Energy deposition

Charged particles strongly interact with matter progressively transferring their energy to the atoms of the matrix. This energy is lost by following two different pathways: i) elastically or ii) inelastically. The former process is also called nuclear energy loss, whereas the latter, electronic energy loss. The dominating process will depend on the energy, or the velocity, of the charged particle.

Elastic or nuclear collision

Elastic collisions with target atoms are characterized by the conservation of both total energy and impulsion of the system and dominate in the low

ion velocity regime, $v \ll v_0$. A nuclear (elastic) collision can be seen as a two-body interaction associated with a force field, V(r). V(r) takes different forms depending on the approach distance, r, between the ion and the atom at rest:

i) when r is less than the screening radius, e.g. the Bohr radius a, ($r \ll a$), nuclear, Colombian, repulsion is the dominating process.

ii) when r is larger than the screening radius ($r \gg a$), the atom in the matrix is seen by the incident ion to be neutral and a hard sphere interaction occurs.

iii) in the intermediary case, ($r \sim a$), a more complex potential, taking into account the screening effects, must be considered.

Elastic collisions can lead to displacement damage, whereby a knocked-on atom recoils away from its initial lattice site. The threshold energy for displacement is defined as E_d. Typically an atom must receive an energy of $E_d \sim 25$eV to create a primary knock-on atom (PKA). As many PKAs receive from the impinging ion an energy larger than E_d, these can generate secondary recoils. Many of these secondary recoils may in turn create additional displacements, giving rise to a displacement cascade. The shape and extension of a cascade depends on both the irradiation parameters and the physico-chemical properties of the target atoms. In a simple model based on hard sphere interactions, the number of atoms displaced in a cascade is given by the Kinchin-Pease formula, [2]. More detailed information on the displacement cascades can obtained having recourse to the SRIM Code, [3, 4] (figure 1.1).

Inelastic or electronic excitation

If during the ion-atom interaction the energy of the system is not conserved, the process is inelastic, or electronic. Inelastic interactions dominate in the high ion velocity regime, $v \gg v_0$. During inelastic processes, impinging ions mainly interact with the electronic clouds of the target atoms favoring atomic excitations and/or ionizations. In general, only the ions having an impact parameter sufficiently weak may interact with the target atoms, ($r \leq a$). However, since the electron masses are small, the ion trajectory is not sensibly modified. In other words, the ion trajectory remains a straight line. Moreover, the inelastic collisions cannot usually result in atomic displacements into the matrix. In most materials, therefore, these inelastic collisions can be treated simply by assuming that the electrons form a viscous background that extracts energy from the fast moving ions, [5]. For high ion energies, the high density of energy deposited within a cylindrical region along the ion trajectory results in the formation of an ion-damaged *latent track*.

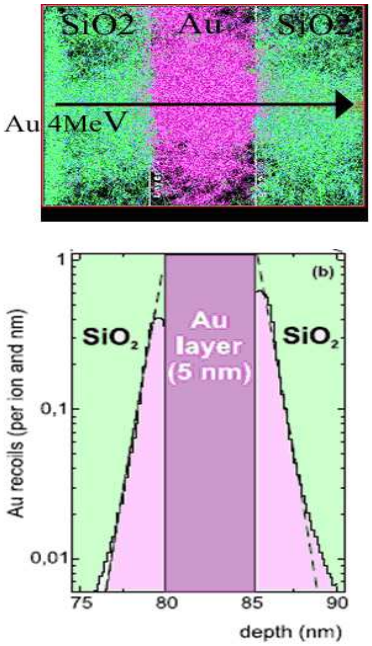

Figure 1.1: Distribution of Au atoms displaced into the SiO_2 matrix through ballistic processes calculated using SRIM code, [3, 4]. The initial system is a SiO_2/Au/SiO_2 multilayer irradiated with 4 MeV Au ions.

1.1.3 Total energy loss (dE/dx) or stopping power (S)

The slowing down of the ion through the matter is associated with the dissipation of its energy. The energy loss is defined as the mean energy transferred by the ion to the target atoms within a layer of thickness dx. This value is weighted by the interaction probability $dP = Ndxd\sigma$, where N is the atomic concentration of the matrix and $d\sigma$ the ion-atom differential cross section. The stopping power is defined as the energy loss per unit of length, S=dE/dx. Furthermore, as the lifetime of an electronic excitation is shorter than the corresponding atom relaxation time, the two processes can be considered independent (Born approximation). The total energy loss, or stopping power, can then be written as the sum of the nuclear and electronic energy losses: $(dE/dx) = (dE/dx)_n + (dE/dx)_e$ or $S = S_n + S_e$.

The first correlation between the stopping power and the ion velocity was given by Bohr. He correlated the stopping power with the effective charge of the ion, Z_1^*, which in turn depends on its velocity, v. Figure 1.2 shows the typical evolution of the energy loss for both nuclear and electronic stopping powers. For low ion velocities, the impinging charged particle becomes neutral by capturing electrons from the target atoms. This favors the elastic interactions. Thus in the low velocity range, the nuclear energy loss is the dominating process. For high ion velocities, the incoming ion looses its

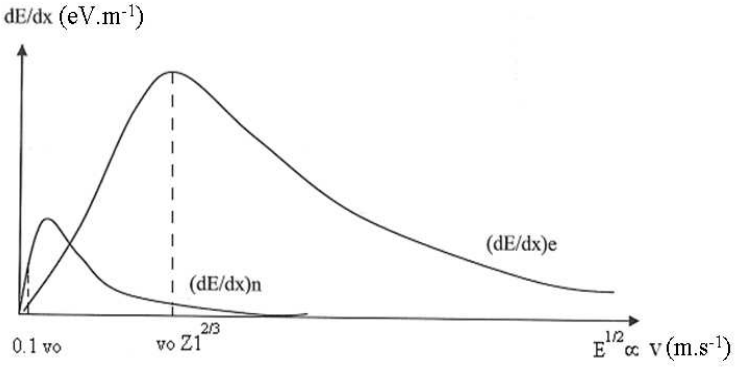

Figure 1.2: Evolution of both nuclear and electronic energy loss with ion velocity.

electrons becoming a punctual charge (bared atom) and the electronic energy loss becomes the dominating process. In both cases, stopping powers increase up to a maximum value, the Bragg peak, and then decrease for higher ion velocities. The Bragg peak is different from the nuclear and the electronic energy losses.

1.1.4 Ion stopping range

After each interaction with the target atoms, nuclear or electronic, the impinging particle losses part of its energy until it implants into the matrix. The total path traveled by the ion, due to all the random collisions, is R. However, the important distance is the projected range along the axis normal to the matrix surface, R_p. During the implantation process, the ions species are distributed into the matrix according to a Gaussian law: ions are distributed around the mean projected range R_p with a mean square deviation given by ΔR_P.

1.2 Nanocomposite materials properties and applications

Particles with a diameter in the range of 1-100 nm are in an intermediate state between the solid and the molecular ones. Much of interest in NPs is stimulated by the fact that the transition from bulk to NP can lead to a number of changes in physical properties. These arise from two principal factors: i) the increase of the surface-to-volume ratio, and ii) the spatial confinement of the electrons imposed by the volume reduction of the NPs. Besides, the properties of the NPs are also strongly dependent upon their composition, structure, aggregation and chemical environment.

i) The increase of the surface-to-volume ratio leads to an increasing importance of the surface effects with respect to the bulk ones. This results in a significant modification of melting temperature, novel phase transitions, increased catalyst properties and enhanced strength and chemical/heat resistance.

ii) Conversely, the main difference between single atom and a bulk material is the existence of quantized energy levels for the former and of continuous valence and conduction bands for the latter. The energy levels for a NP are in between these two extreme case. They are degenerated in comparison to the single atom remaining however discrete, or quantized. The transition from classical to quantum mechanics results in a variety of novel optical, electronic and magnetic effects. In particular for metallic NPs the optical properties result from the electrodynamic effects and from the modification of dielectric environment. In particular, the electronic confinement results in an amplification of the absorption and the appearance of a resonance, [6].

1.2.1 Optical properties of metallic NPs: the plasmon resonance

The interaction between an electromagnetic field and a metallic NP leads to the excitation of conduction electrons localized at the particle surface. These electrons oscillate as a group with a characteristic frequency that depends on the electronic properties of the particles and of the host matrix. Such collective oscillation is known as surface plasmon resonance (SPR). During an oscillation, a part of the metal surface is enriched with negative charge of electrons, the other part is endowed with positive charge thus creating a dipole moment. This dipole is sustained under the electric field excitation by absorbing energy according to the material properties. Such properties are related to the material polarizability. For metallic NPs, the material response, i.e. the absorption band, is in the visible part of the optical spectrum, [7, 8, 9]. Moreover, the confining medium modifies the optical response of the NPs. Thus, the SPR position is a sort of fingerprint of the nanocomposite material. The SPR depends on both the NP composition, size and morphology and on the confining environment, i.e. the host matrix, figure 1.3(a-d).

A systematic study on the optical properties of metallic NPs reveals the following features:

•For particles less than 1nm, no absorption band is observed.

The increasing of Nps size leads to a competition between absorption and scattering of the incident field.

•For small NPs (<25nm) the absorption term dominates. In this range the optical field is nearly constant (quasi static approximation) as the particle size is sufficiently small in comparison to the electromagnetic wavelength λ ($R \ll \lambda$)). A small shift of the SPR and a broadening of the peak is observed.

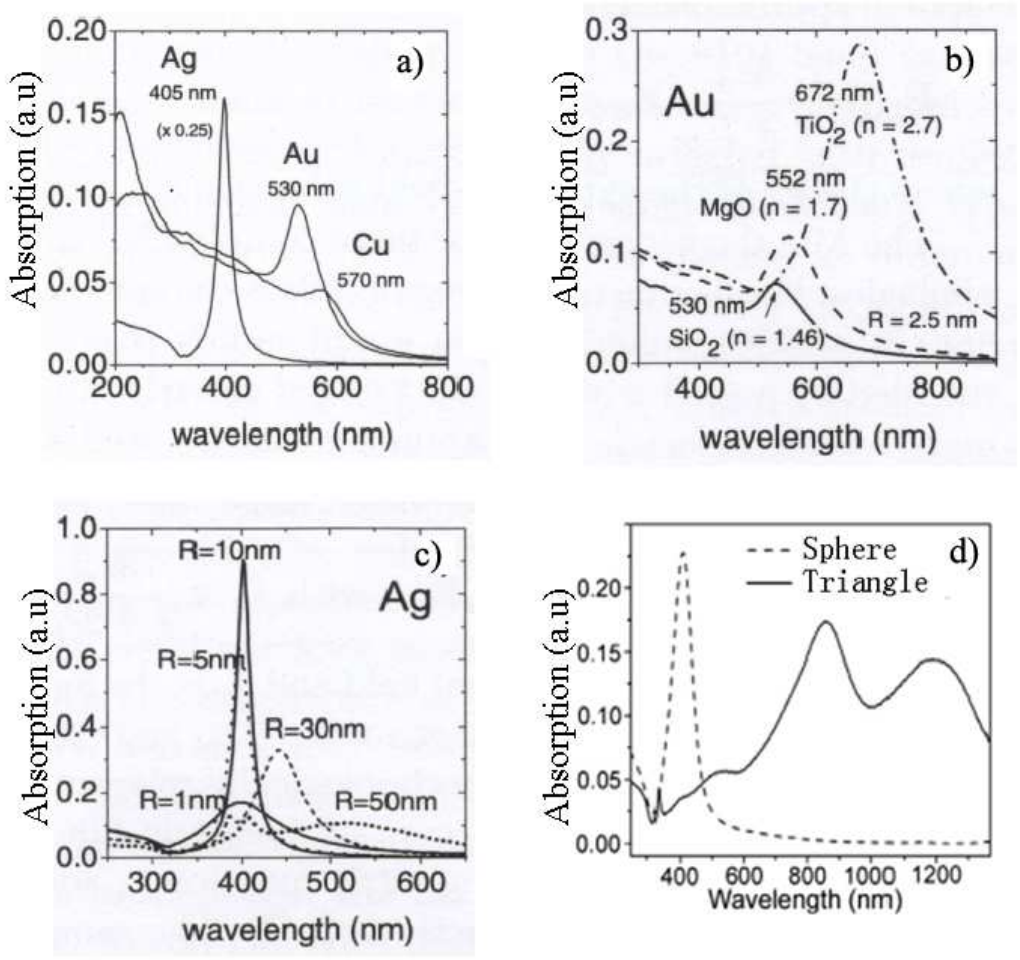

Figure 1.3: Absorption spectra of metallic NPs as a function of : a) their composition. 5 nm NPs Au, Ag , Cu in silica, b) the embedding matrix. 2.5nm Au NPs (n is the refractive index), c) their size. Ag NPs in silica and d) their shape (Au NPs), [10, 11].

•For larger NPs (>25nm) the SPR shows a red shift. Here, the scattering of the light is the dominant process. Thus a decrease of the absorption intensity is observed. In this range of size, a higher order multipole expansion should be taken into account [6], as retardation effects inside the NP create a phase shift with the applied field electromagnetic field ($R \leq \lambda$).

A short history

The first glasses containing metal clusters were fabricated by Roman glassmakers in the fourth century AD and the most celebrated example is the Lycurgus cup (figure 1.4). This cup was made of a soda-lime glass con-

taining Au and Ag NPs. The most fascinating aspect of this cup is its color which depends on the illumination mode: opaque green when illuminated in reflection but strong red when illuminated in transmission.

Figure 1.4: Lycurgus Cup illuminated in reflexion (left), in transmission (right).

In the seventeenth century, *Purple of Cassius*, a colloid of tin dioxide and gold particles, became a popular colorant in glasses. These early manifestations of the unusual colors displayed by metal particles prompted Faraday's investigations into the colors of colloidal gold in the middle of the last century, [12]. The work of Maxwell-Garnett achieved in 1904, introduced the effective medium description of a composite with a metallic NPs, [13]. In 1908 a first formal explanation of the color of glasses containing NPs of different sizes was given in the fundamental work published in *Annalen der physik* by Mie, [14]. The Mie theory allows to describe the scattering of a plane wave by a spherical isolated inclusions in a non-absorbing medium.

Potential applications

Surface plasmon effects may find applications in a wide range of domains as optical filters, including eyes glass coating, [15, 16], or devices based on *plasmon waveguide*, [17]. Surface plasmon oscillations of closely spaced and coupled NPs gives rise to a coherent energy propagation that can be guided along chains or arrays of NPs. This could represent a new way to transmit and guide optical signals on dimension smaller than the diffraction limit.

Another application of SPR is the submicrometer *plasmon printing lithography*, where a broad optical stimulus excites the surface plasmon resonance of strategically placed NPs, which in turn emit light at a wavelength that

develops photoresist in their immediate vicinity, [18, 19].

The non-linear optical properties of nanocomposites are attractive due to the short response time, and have potential applications in optoelectronics, in optical-memory or switching devices, [15, 20, 21].

1.2.2 Elaboration of nanocomposite materials

Since the critical properties of the nanocomposites are directly dependent on the NP size, for practical applications, is of primary importance to work with the narrowest size distribution. As a general rule, the improvement of the nanocomposite features are tightly associated to the NP synthesis. This, in turn, is related to the knowledge of the mechanisms of nucleation and growth of the confined NPs. Thus, first, we briefly review the precipitation mechanisms under thermodynamic conditions. Besides, we describe the NP synthesis when ion-beams are considered. Finally, we discuss the advantages and the drawbacks of the ion-related techniques and we give the motivations for this thesis work.

1.2.3 Elaboration of nanocomposite materials under thermodynamic conditions

The stability of a thermodynamic system can be described using the Gibbs free energy:

$$G = H - TS \tag{1.1}$$

where H is the enthalpy, T the temperature and S the entropy of the system. The most stable phase will correspond to the best compromise between a small enthalpy and a large entropy, e.g. H$\ll$S. A thermodynamic transformation is possible when the Gibbs free energy difference between the initial and the final states is negative, $\triangle$G=G$_f$-G$_i$<0. In other words, when the total Gibbs energy is reduced. Thus, a system in a metastable state can minimize its energy through a phase transition. One example is the liquid-solid phase change. Another example is the phase separation in a solid solution leading to the nucleation and growth of NPs within the host matrix.

The decomposition of a binary solution into two separate phases occurs by following several steps. The key parameter is the supersaturation, S(t), defined as S(t)=(C(t)-C$_\infty$)/C$_\infty$, where C(t) is the solute concentration at a given time and C$_\infty$ is the bulk solubility, figure 1.5.

• **Accumulation**. As soon as the solute is introduced into the host matrix, S(t) increases linearly as a function of the amount of monomers deposited. However, below a critical value S$_c$, the concentration of solute atoms increases without any phase change.

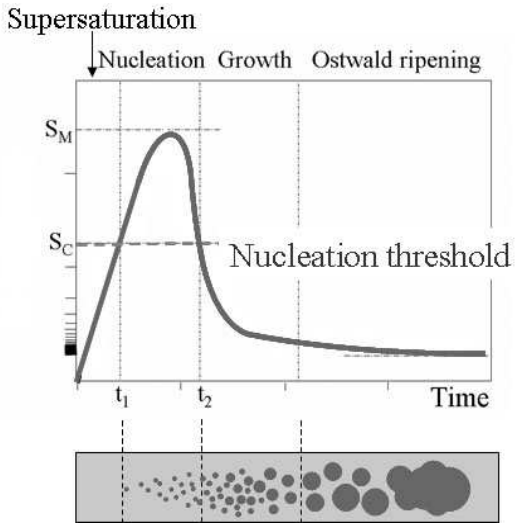

Figure 1.5: Time evolution of the supersaturation of solute atoms into a matrix.

• **Supersaturation and nucleation.** When the solute concentration S(t) exceeds S_c, the system becomes metastable. Local fluctuations of the solute concentration, or thermal fluctuations, or defects present within the matrix, drive the system into a new equilibrium phase, and stable embryos start to form.

• **Growth regime.** Owing to the occurrence of nucleation and subsequent growth of the nuclei (e.g., the precipitates act as a sink for the diffusing solute), S(t) starts to decrease despite the ongoing monomer deposition, and the supersaturation eventually drops below the nucleation threshold. Below S_c, the nucleation of new particles is inhibited and all the existing NPs grow by incorporating the incoming monomers.

• **Ostwald ripening regime.** Since the critical radius of the particles scales as the inverse of the supersaturation level, i.e., $R_c \sim 1/S(t)$, when the supersaturation reaches a sufficiently low value, the smaller particles become instable and eventually dissolve. This regime is called Ostwald ripening (OR). Here, precipitates evolve through a mass redistribution, i.e. larger NPs growth at the expense of the smaller ones.

1.2.4 Irradiation-based nanocomposite materials

Ion-irradiation can be used as a tool to synthesize NPs within an host matrix or to modify their physical and chemical properties. The synthesis of materials based NPs performed by using ion-beam processing can be exploited using three different methodologies:

•**Ion-beam direct synthesis**. Ion implantation allows to introduce a

foreign element A into the near surface region of a solid B, for the purpose of modifying the electronic structure by addition of a doping element in low concentration or for obtaining a supersaturated solid solution. The impurity supersaturation can be controlled by varying the implantation conditions. Ion implantation may be used for single, [22, 23, 24], or sequential implantations, [25, 26, 27, 28, 29, 30, 31, 32, 33, 34, 35] and is generally followed by an annealing treatment to promote the precipitation of the NPs. The overall process is called *ion-beam synthesis* and the final feature of the NPs depends on the following parameters:

i) *ion flux and implantation temperature.* For Au NPs within a silica matrix, when the implantation temperature is increased and the ion flux is kept constant, the formation of larger NPs is observed, [36]. Conversely, when the flux is increased and the temperature is maintained constant, smaller NPs are synthesized. For multiple implantations at different temperatures, the size distribution of the NPs depends on the sequence of the implantations. By decreasing the implantation temperature in the second implantation step, a broad peak, due to the overlap of the two individual distributions, is obtained. On the other hand, by increasing the temperature during the implantation, a narrower peak is observed.

ii) *post-implantation annealing time, temperature, and atmosphere.* The dependence of these parameters for Au NPs in SiO_2 has been studied in detail by Demarchi et al., [37, 38].

- For annealing treatments between 1h and 12h in air at 900°C, the size of the NPs is found to increase with time. Moreover, two growth regimes are observed: a) the NPs start to grow in a regime limited by the diffusion b) followed by their coarsening (Ostwald ripening regime) when the solute concentration becomes sufficiently low.

- for isochronal annealing, 1h, in air atmosphere, the temperature increasing from 400°C to 900°C results in a significant widening of the NPs size distribution and its shift toward larger sizes.

- Finally, annealing under inert gas atmosphere, Ar, results in the formation of smaller precipitates.

• **Ion-beam indirect synthesis.** Here, ion-irradiation is used to promote the nucleation of NPs within an already supersaturated host matrix, [39, 40, 25]. This can be done by tailoring the energy deposited into the matrix, for example by controlling the nuclear-to-electronic energy loss ratio. Several doping methods can be used to achieve this objective:

- A first doping method is the ion-exchange technique. Here, thermal ionic diffusion or electric field assisted process are used to introduce metallic ions into the glass, [41]. The precipitations of the metal clusters is triggered by the irradiation of doped samples to high fluence with light ions as He, H or Ar to insure inelastic energy transfer to the system, [41, 42, 43].

- A second method is to use metal oxide-containing glasses. Room temperature MeV ion irradiation of a glass containing copper oxide initiates

nucleation of pure Cu clusters via the inelastic electronic component of the ion energy loss, when the latter is above a threshold value, [39].

- A third method consists in irradiating a pre-implanted sample. For example, Ila et al., [44], pre-doped a silica glass matrix with a single ion-implantation (2 MeV Au ions at fluence of $1.2\text{x}10^{17}\text{cm}^{-2}$) . The following irradiation with 5 MeV Si ions results in the formation of small NPs already at low irradiation fluences. At higher fluences the increasing of NPs volume fraction and size was attributed to the electronic energy deposited by the Si ions.

• **Ion-beam modification.** The energy (electronic or nuclear) deposited by the ions is used to modify already formed NPs by changing their shape, composition, spatial and size distribution.

High-energy ion-beam mixing can be applied as an alternative to the ion-beam synthesis to form metallic nanoclusters without the drawbacks of direct ion implantation. Thin SiO_2-metal multilayers were irradiated at room temperature with MeV heavy ions in order to produce an homogeneous SiO_2 layer containing metallic NPs over the whole sample thickness, [45, 46].

Irradiation in the nuclear stopping regime of NPs already present within the silica matrix leads to the formation of both cluster-satellite topology or to promote selective dealloying in bimetallic NPs [47, 25].

Finally, irradiation in the electronic stopping regime may result in the transformation of pristine spherical metallic NPs into prolate nanorods and nanowires along the ion beam [48, 49, 50, 51]

1.2.5 Advantages and drawbacks of ion-beam synthesis techniques

Nanocomposite materials produced by ion-beam processes have a number of attractive characteristics. They provide a wide variety of single-element or compound NPs within virtually any solid host matrix [52]. Besides, as the particles are formed below the sample surface, the NPs are protected from the environment and the resulting composites are durable in time. Moreover, the research activity in this field is stimulated by the possibility to produce high-purity materials with large NPs volume fraction and with accurately determined dopant concentration. On the other hand, using the ion-beam techniques nucleation and growth stages can be, to some extent, temporally separated. Seed nuclei formed during the irradiation step can be afterward ripen during the subsequent thermal processing. Finally, nanocomposite materials can be ion-driven into novel experimental configurations that are far off-equilibrium.

However, despite the many potential applications, there are currently no commercial NPs-based devices that make use of the ion-beam synthesis concept. The main and most crucial difficulty is the inability to produce a suitable narrow size and spatial NP distributions. Additional difficulties arise

from the damages introduced within the host matrix during the irradiation. Thus, a post-implantation thermal treatment is generally imposed to remove the irradiation-induced defects. The annealing process is also necessary to promote the precipitation of the NPs. However, it results in an enlargement of the final NPs size distribution according to the classical thermodynamic.

1.3 This thesis

Although, nucleation and growth during implantation can be controlled to some extent by varying ion flux and substrate temperature, the control of the NPs size distribution remains a challenging task. To overcome this difficulty, new ion-based methodologies have been developed either i) by combining the electronic energy deposition and the thermal annealing, or ii) by having recourse to multiple implantation steps and intermediate annealing. In this thesis, the rationalization and the improving ion beam synthesis of NPs has been studied in detail. The objectives of this thesis are twofold: i) to go further in the description of the behavior of the ion-driven NPs and ii) to overcome the limitations related to the ion-beam techniques providing a guideline methodology to rationalize the synthesis of NPs when ion-beams are used.

In *Chapter 2* experimental conditions are introduced. To obtain an insight into the evolution of a precipitate phase under ion irradiation, not only a control of the irradiation parameters but also of the initial NP properties is required. Thus, the fabrication of a model system is described in detail.

In *Chapter 3 and 4* samples composted of chemically synthesized Au NPs embedded within a planar silica film are used as model system to investigate the evolution of the second phase under irradiation when the temperature and the ion stopping power are changed.

In *Chapter 5* we study how the evolution of satellites clusters is related to the initial size of the pristine NPs. In particular, when the initial NP size is increased both the size and the density of the satellites are modified. Thus, the growth kinetic of the satellites can only be studied when NP size dispersion is narrow and for fluences lower than a threshold value.

In *Chapter 6* we use the results obtained in the previous chapter to give an insight into the evolution of a precipitate phase under irradiation. We show that the satellites evolve in an Ostwald ripening regime limited by the diffusion in an open system. In addition, the complete evolution of the gold supersaturation is obtained and the temporal window for the nucleation regime is determined. It allows us to give a guideline method to improve the control of the particles monodispersity during the ion beam synthesis. Moreover, an estimation of the threshold concentration for nucleation, an effective value for the surface tension of the Au NPs and the gold diffusivity under irradiation are given.

In *Chapter 7* direct and inverse Ostwald ripening (IOR) processes under irradiation are systematically investigated. Our experimental results are compared to those of the Heinig's model. Moreover, using our model system, all the parameters contained into the Heinig's model are estimated, i.e. the evolution of the capillarity length with temperature, the diffusivity under irradiation and the steady-state concentration for both planar and curved interfaces. We show that the Heinig's model correctly describes the IOR process. However, the threshold temperature for the OR-to-IOR transition is not correctly defined and that two new intermediate regimes must be introduced. Finally, we redefine the concept of IOR showing that, depending on the steady state size, NPs can either to grow or to be dissolved

Bibliography

[1] M. Nastasi, J.W. Mayer, J.K. Hirvonen, Ion-Solid Interaction, Cambridge University Press (1996)

[2] G.H. Kinchin and R.S. Pease, "The Displacement of Atoms in Solids by Radiation," Reports on Progress in Physics, vol. 18, pp. 1-51, 1955.

[3] J. F. Ziegler, J. P. Biersack, and U. Littmark, The Stopping Ranges and Ranges of Ions in Solids _Pergamon Press, New York,1985.

[4] http://www.srim.org

[5] P.Sigmund, Particle Penetration and radiation Effects (Springer, Heidelberg, 2006)

[6] U.Kreibig, M.Vollmer, Optical Properties of Metal Clusters (Springer, Berlin 1995)

[7] A.Kawabata, R.Kubo, J.Phys.Soc..Japan., 21, 1765 (1966)

[8] K.L.Kelly, E.Coronado, L.L. Zhao, G.C.Schatz, J.Phys.Chem.B 107,668 (2003)

[9] C.Dahmen, G.von Plessen , Aust.J.Chem., 60, 447 (2007)

[10] P. Mazzoldi and G. Mattei, Riv. Nuovo Cimento 28, 1 (2005)

[11] Y. Sun, B. Mayers, Y. Xia , Nano Letters, 3, 675 (2003).

[12] M.Faraday, Philos. Trans. R.Soc. 147, 145 (1857)

[13] J.C. Maxwell-Garnett, Philos. Trans. R.Soc. 203, 385 (1904)

[14] G.Mie, Ann.Phys. (Leipzig) 25, 377 (1908)

[15] C.Flytzanis, F.Hache, M.C.Klein, D.Ricard, P.Roussignol, E.Wolf (ed.), Prog.Optics 29, Amsterdam, North Holland, 321 (1991)

[16] M.Mennig, K.Endres, M.Schmitt, H.Schmidt, J.Non-crys. Solids 218, 373 (1997)

[17] S.A. Maier, M.L. Brongersma, P.G. Kik, S.Meltzer, A.A.G.Requicha, H.A. Atwater, Adv.Mater., 13, 1501(2001)

[18] Kik PG, Martin AL, Maier SA, Atwater HA , Properties of metals and nanostructures, 4810, 7 (2002)

[19] P.G. Kik, S.A. Maier, H.A. Atwater, 2001 MRS Fall Meeting Abstracts (Materials Research Society, Warrendale, 2001)

[20] P.Chakraborty, J.Mater.Sci. 33, 2235 (1998)

[21] L.Yang, D.H. Osborne, R.F.Haglund Jr., R.H.magruder, C.W.White, R.A.Zuhr, H.Hosono, Apll.Phys.A, 62, 403 (1996)

[22] P.Kluth, B. Joannessen, D.J. Cookson, G.J. Foran, M.C. Ridgway, Nucl. Instr.and Meth. B, 246, 30 (2006)

[23] C.W.White, D.S. Zhou, R.A. Zhur, R.H.Magruder, Trans.Mat.Res.Soc.Jpn., 17, 553 (1994)

[24] G.Battaglin, Nucl. Instr.and Meth. B, 116, 102 (1996)

[25] F. Gonella, G.Mattei, P. Mazzoldi, C.Sada, G.Battaglin, E.Cattaruzza, Appl.Phys.Lett. 75, 55 (1999)

[26] G.Bataglin, M.Catalano, E.Cattaruzza, F.D'acapito, C. De julian Fernandez, G.Demarchi, F.Gonella, G.Mattei, C.Maurizio, P.Mazzoldi, A.Miotello, C.Sada, Nucl.Instr.and Meth. B, 178, 176 (2001)

[27] C. De julian Fernandez, G.Mattei, G.Bataglin, C.Maurizio, P.Mazzoldi, C.Scian, Nucl.Instr.and Meth. B, in press

[28] C. De julian Fernandez, M.Tagliente, G.Mattei, C.Sada, V.Bello, C.Maurizio, G.Bataglin, C.Sangregorio, D. Gatteschi, L.Tapfer, P.Mazzoldi, Nucl.Instr.and Meth. B, 216, 245 (2004)

[29] G.Mattei, G.Bataglin, V.Bello, E.Cattaruzza, C. De julian Fernandez, G.Demarchi, C.Maurizio, P.Mazzoldi, M.Parolin, C.Sada, Nucl.Instr.and Meth. B, 218, 433 (2004)

[30] C. De julian Fernandez, G.Mattei, C.Sangregorio, M.Tagliente, V.Bello, G.Bataglin, C.Sada, L.Tapfer, D. Gatteschi, P.Mazzoldi , J.Non-Cryst.Solids 345-346 (2004) 681

[31] G.Mattei, C.Maurizio, P.Mazzoldi, F.D'acapito, G.Bataglin, E.Cattaruzza, C. De julian Fernandez, C.Sada, Phys.Rev.B, 71 (2005) 195418

[32] E.Cattaruzza, F.D'acapito, F.Gonella, A.Longo, A.Martorana, G.Mattei, C.Maurizio, D. Thiaudiere, J.Appl.Cryst. 33 (2000) 740

[33] C. De julian Fernandez, C.Sangregorio, G.Mattei, C.Maurizio, G.Bataglin, F.Gonella, A.Lascialfari, S.Lorusso, D. Gatteschi, P.Mazzoldi, J.Gonzales, F.D'acapito, Nucl.Instr.and Meth. B, 175-177, 479 (2001)

[34] R.Bertoncello, S.Gross, F.Trivillin, F.Caccavale, E.Cattaruzza, P.Mazzoldi, S.Daolio, J.Mater.Res. 14 (1999) 2449

[35] E.Borsella, S. Dal Toe, G.Mattei, C.Maurizio, P.Mazzoldi, A. Saber, G.Bataglin, E.Cattaruzza, F.Gonella, A.Quaranta, F.D'acapito , Mat.Res.Eng. 82 (2001) 148

[36] M.Strobel, K.H.Heinig, W.Moller, A.Meldrum, D.S.Zhou, C.W.White, R.A.Zuhr, Nucl. Instr.and Meth. B, 147, 343 (1999)

[37] G.De Marchi, G.Mattei, P.Mazzoldi, C.Sada, J.Appl.Phys. 92, 4249 (2002)

[38] A.Miotello, G.De Marchi, G.Mattei, P.Mazzoldi, C.Sada, Phys. Rev. B,63, 075409 (2001)

[39] E.Valentin, H.Bernas, C.Ricolleau, F.creuzet, Phys.Rev.Lett. 86 (2001) 99

[40] E.K Lipinska-Kalita, D.M.Krol, R.J Hemley, G.Mariotto, P.E.Kalita, Y.Ohki, J.Appl.Phys. 98, 054301 (2005)

[41] F.Caccavale, G.De Marchi,F. Gonella,P. Mazzoldi, C.Meneghini, A.Quaranta, G.W.Arnold, G.Battaglin,G.Mattei, Nucl. Instr.and Meth. B, 96, 382 (1995)

[42] G.Demarchi, F.Gonella, P.Mazzoldi, G.Bataglin, E.J. Knystautas, C.Meneghini, J.Non-Cryst.Solids 196 (1996) 79

[43] F.Gonella, E.J. Knystautas, G.Mattei, P.Mazzoldi, C.Meneghini, E.Cattaruzza , F.Garrido, D.Osborne, Nucl. Instr.and Meth. B, 127, 562 (1997)

[44] D.Ila, E.K.Williams, C.C.Smith, D.B. Poker, D.K. Hensley, C.Klatt, S.Kalbitzer, Nucl. Instr.and Meth. B, 148, 1012 (1999)

[45] F.Garrido, J.C. Dran, L.Thome, C. Meneghini, F.Gonella, A.Quaranta, Nucl. Instr.and Meth. B, 115, 561 (1996)

[46] J.C.Pivin, G.Rizza, Thin Solid Films, 366,284 (2000)

[47] G.Mattei, G. De Marchi, P.Mazzoldi, C.Sada, V.Bello, G.Battaglin, Phys.Rev.Lett., 90, 085502 (2003)

[48] C. D'Orléans, J. P. Stoquert, C. Estournès, C. Cerruti, J. J. Grob, J. L. Guille, F. Haas, D. Muller, M. Richard-Plouet, Phys. Rev. B 67, (2003)220101R

[49] R. Giulian, P. Kluth, L.L. Araujo, D.J. Sprouster, A.P. Byrne, D.J. Cookson, M.C. Ridgway, Phys. Rev. B 78 (2008) 125413

[50] G. Rizza, E.A. Dawi, A.M. Vredenberg, I. Monnet, Appl. Phys. Lett. 95 (2009) 043105

[51] E.A. Dawi, G. Rizza, M.P. Mink, A.M. Vredenberg, F.H.P.M. Habraken, J. Appl. Phys. 105 (2009) 074305

[52] A. Meldrum, L.A. Boatner and C.W. White, Nucl. Instr. and Meth. B **178**, 7 (2001)

Chapter 2

Sample fabrication and characterization

Abstract

To obtain an insight into the evolution of a precipitate phase under ion irradiation, the sample must be prepared in a very controlled way. In this chapter we will describe how to fabricate a model system. In our approach, metallic NPs are first chemically synthesized and then sandwiched between two layers. Au NPs in amorphous SiO_2 were chosen as a model system because of the low solubility of Au in SiO_2 and its relative large mass difference with respect to Si and O which facilitates the particle observation in transmission electron microscopy (TEM) analysis. The synthesis of the gold NPs and the silica elaboration are introduced in sections 2.1 and 2.2. The grafting of the NPs onto the silica layer and their confinement into the silica matrix are described in sections 2.3 and 2.4. Finally, sample characterization and irradiation conditions are described in sections 2.6 and 2.7.

2.1 Gold nanoparticle synthesis

Noble metal nanoparticles (NPs) have been intensively studied within the past 15 years, [1]. The optical properties of metallic NPs are appealing for materials applications, as well as engineering and biomedical applications. Some of the interest in gold NPs is a prominent optical resonance in the visible range. The latter depends on chemical environmental, size, and shape of the particles. Therefore, applications require synthesis protocols, which deliver well-defined shapes and sizes. Several classes of chemical synthesis routes exist, which display different characteristics of the final products. Among them, the reduction of a gold salt by citrate, introduced by Turkevich et al. and refined by Frens, produces almost spherical particles over a tunable range of sizes. In this section we will describe the different chemical methods to synthesize gold NPs. In this thesis, the model system will be studied for pristine NP sizes ranging from 4 up to 15 nm. It worth mentioning that, optimal conditions for studying the evolution of the nanophase under irradiation is achieved when nearly monodisperse NPs are considered. For this reason, Jana et al., [2], seeding growth synthesis was chosen for obtaining 4 nm NPs, whereas Turkevich protocol, [3], has been employed to form 15 nm NPs.

2.1.1 Synthesis and TEM analysis of 4nm Au NPs

For the synthesis of Au NPs having an average size of about 4 nm we used the method developed by Jana et al [2]. The chemical synthesis of the NPs is very sensitive to the impurities, thus the glassware and the magnetic stirring beads are cleaned with freshly prepared aqua regia (1:3 HNO_3:HCl) and rinsed with distilled water. The synthesis protocol is as follows: to 20 ml of a 2.5×10^{-4}mol.l^{-1} solution of tetrachlorauric acid ($HAuCl_4$, $3H_2O$, Aldrich), 1.5 mg of trisodium citrate ($C_6H_5O_7Na_3$, $2H_2O$, Fluka) were added. The mixture is cooled in an ice bath and 0.6 ml of a 0.1×10^{-4}mol.l^{-1} solution of sodium borohydride ($NaBH_4$, H_2O, Fluka) is then added. As soon as the sodium borohydride is added, the solution turns into pink. This is the signature that the gold has been reduced, e.g $Au^{3+}\rightarrow Au^0$. Neutral gold atoms can diffuse into the solution and eventually precipitate to form Au embryos. These can grow to colloids by solute accumulation. Finally, colloids are stabilized by the citrate acting as a capping agent. The citrate plays a twofold role: i) it allows the stabilization of the NPs and ii) owing to it negative charge prevents their aggregation.

For small NPs the optical absorption is weak and it was not possible to detect any absorption signal with the spectrometer. For this reason, the presence of colloidal Au NPs can only be determined by having recourse to the transmission electron microscopy. We observe NPs having an average size of 3.5$\pm$ 0.7 nm (figure2.1).

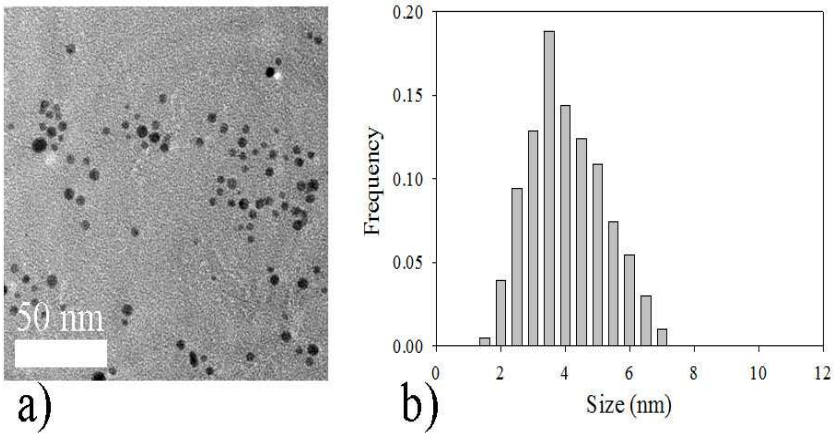

Figure 2.1: a) Bright field TEM micrograph of 3.5nm Au NP deposited onto a carbon film and b) the corresponding size distribution.

2.1.2 Synthesis of 15nm Au NPs: the Turkevich method

To obtain NPs having an average size of about 15nm, we have chosen the standard method developed by Turkevich, [3]. The reduction of $HAuCl_4$ in water is initiated by trisodium citrate upon heating. It plays the same role as the sodium borohydride ($NaBH_4$) in Jana's synthesis. The synthesis protocol is as follows: first, 2.52 ml of a 4×10^{-2}mol.l^{-1} solution of tetrachlorauric acid ($HAuCl_4$, $3H_2O$, Aldrich) were added in 92.5 ml of pure water into a 250 ml round bottom flask. The solution is then heated to 90°C using an oil bath. At this moment, 5 ml of 1 w% of trisodium citrate ($C_6H_5O_7Na_3$, $2H_2O$, Fluka) solution were added. The citrate permits to reduce Au^{3+} to neutral gold atoms, Au^0, [4]. After 2-4 minutes, the appearance of a light blue color attests the formation of gold embryos, figure 2.2. Upon heating, the solution turns then into a pink color, traducing the growth of embryos into larger NPs. The reaction stops whenever: i) the solute concentration becomes lower than the nucleation threshold and/or ii) the growth of the colloids is stopped, e.g. when the colloids are stabilized by the citrate. It occurs at a time of about 16 min. The final solution has a dark pink color corresponding to NPs having a size of 15.9±2.0 nm.

TEM analysis

TEM micrographs of figure 2.3 are related to the different solutions, e.g. reaction time, as shown in figure 2.2. TEM images are obtained by depositing a drop of the solution on a microscope grid coated with a carbon thin film. To avoid the diffusion of the NPs toward the edges of the grid, a hydrophile

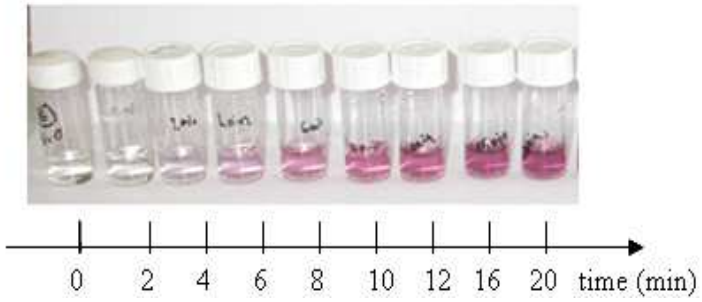

Figure 2.2: Kinetic of the Turkevich's synthesis. The solution color changes from light blue to dark pink following the nucleation and growth for the gold NPs.

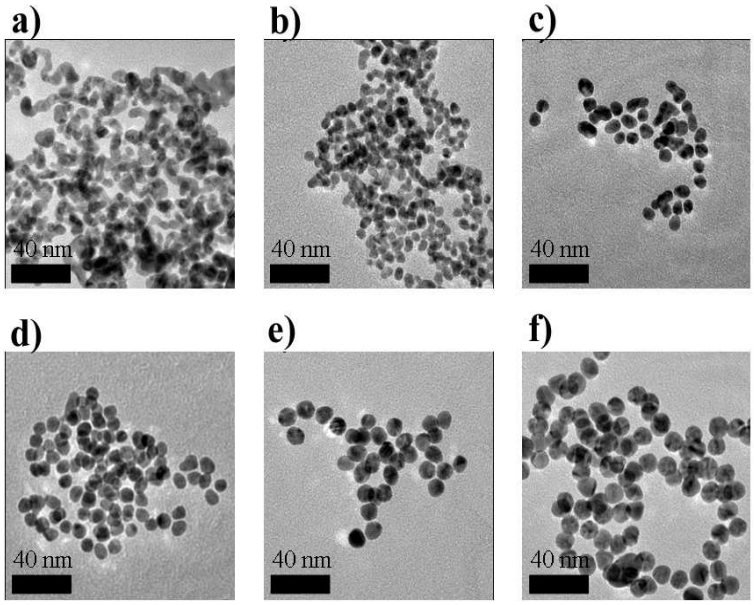

Figure 2.3: Bright field TEM micrographs of Au NPs for different reaction times: a) 2-5 min, b) 6 min, c) 8 min, d) 12 min, e) 16 min, f) $\geq$20min

polymer (polyethylenimine) has been previously deposited to stabilize the NPs onto the carbon film.

Within first minutes of the reaction (2-5 min), the solution, initially transparent, turns to blue. This corresponds to the nucleation of gold embryos and their aggregation into percolated nanostructures, figure 2.3a). After 6 minutes, figure 2.3b), the color of the solution turns into a light pink color. This corresponds to the end of the aggregation/percolation phase and to the beginning of the growth phase. In other words, the NPs start to grow independently. Within this step, NPs continue to grow independently to-

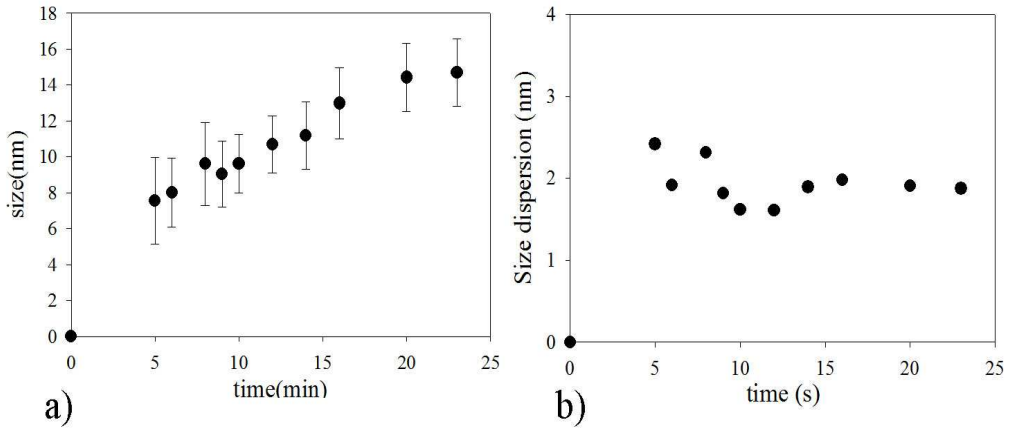

Figure 2.4: a) evolution of the mean NP size, and b) the corresponding size dispersion with reaction time.

ward an equilibrium size, figures 2.3 c-f). Correspondingly the solution color changes to dark pink.

Figure 2.4a) shows the evolution of the size of the NPs with the reaction time. The measure can be performed whenever the percolation of the NPs is strongly reduced and separated NPs are visible on the grid. This corresponds to a reduction time larger than about 5 minutes. We observe that the dimension of the NPs linear scales with time and saturates at about 15 nm for times larger than 20 minutes. This is the signature that the reaction is completed. In this final step, the NPs are completely capped by citrate, which prevents any further growth. The evolution of the size dispersion with the reaction time is shown in figure 2.4b). It shows a weak dependence on the reaction time, remaining close to 2 nm.

Optical absorption

Figure 2.5 shows the absorption spectra corresponding to the evolution of the NP synthesis with time. Spectra measurements have been carried out using a cary 50 spectrometer. At the beginning of the reaction, no absorption peak is visible. This may correspond either i) to the fact that nucleation did not start yet, or ii) that the formed NPs are very small. In this latter case the extinction coefficient is low and the plasmon resonance is difficult to detect.

As the NPs reach a *critical* size, an absorption peak appears at about 580 nm. As the synthesis goes on the plasmon band shifts toward smaller wavelengths until it reaches an equilibrium position at 520 nm, characteristic for 15 nm gold NP. It worth mentioning that this results is in opposition to what is reported in literature, [5]. Correspondingly, the intensity of the plasmon peak increases and its width shrinks with the reaction time. By

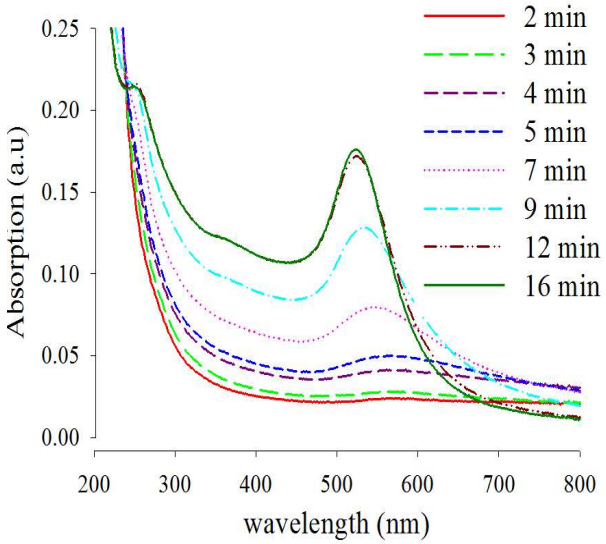

Figure 2.5: Evolution of absorption spectra with reaction time.

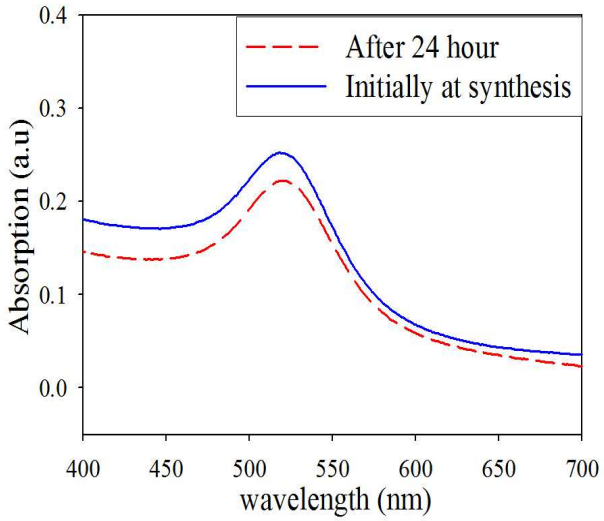

Figure 2.6: Stability of 15 gold NPs with time.

definition the intensity of the peak is proportional to the number of absorbing NPs, whereas its width is related to the NP size distribution. To check the stability of the solution, the optical absorption is done 24h after the synthesis, figure, 2.6. No differences between the two spectra are observed,

i.e. the maximum and the width of the spectra did not change, meaning that the NPs are stable within the solution.

2.2 Silica Elaboration

Amorphous silica has a large spectrum of applications ranging from windows glasses to more advanced micro- and nanotechnology applications. Amorphous silica is a disordered structure composed of silica and oxygen atoms, [6]. A silicon atom can bind with 4 oxygens atoms constituting a tetrahedron structure. Tetrahedrons are bind with each other creating a network associated to $\equiv Si - O - Si \equiv$ bonds. In the following sections, we will describe two methods for silica synthesis: i) the sol-gel and ii) the plasma enhanced chemical vapor deposition (PECVD).

2.2.1 Sol-gel synthesis

The sol-gel process is a wet chemical technique used for the fabrication of both glassy and ceramic materials, [7]. The sol-gel approach is a cheap and low-temperature technique (20 to 150°C) that maintains a high degree of chemical purity. During the synthesis, the sol (or solution) formed of discrete particles or continuous polymer network evolves gradually toward the formation of a gel-like network containing both a liquid phase and a solid phase. In both cases, a drying process serves to remove the liquid phase from the gel. Subsequent thermal treatment may be performed in order to favor further condensation of the system.

Sol-gel silica

The chemical reactions leading to the formation of silica can be described as a two steps process: i) the hydrolysis and ii) the condensation. Following one of these routes the formation of a material with increasing density is obtained either as silica colloids or continuous gel-like network. In general, the synthesis starts with alkolydes $Si(OR)_n$. In the following, we will describe these two reactions when a low molecular weight alkoxysilane, such as the tetraethoxysilane or TEOS ($Si(OC_2H_5)_4$) is used.

Hydrolysis

When water is added into an alcoholic solution containing TEOS, a hydrolysis process takes place allowing the transformation of ethoxy groups (Si-OR) into silanol groups (Si-OH) as shown in figure 2.7. This process can be catalyzed either in acid or basic medium, [8].

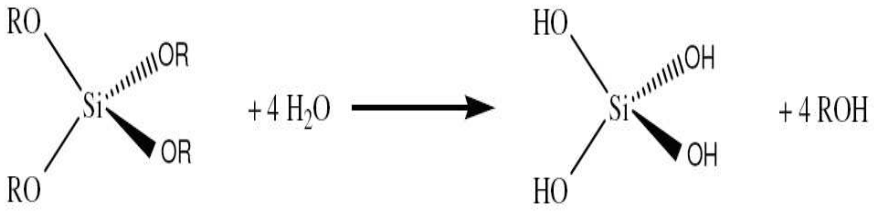

Figure 2.7: alkoxysilane hydrolysis reaction

Condensation

After the hydrolysis a condensation step takes place. Two condensation paths involving silanol group interactions are possible:

•From the condensation of two silanol groups (Si-OH), a siloxane bridge is formed (Si-O-Si) with the releasing of a water molecule (H_2O), figure2.8.

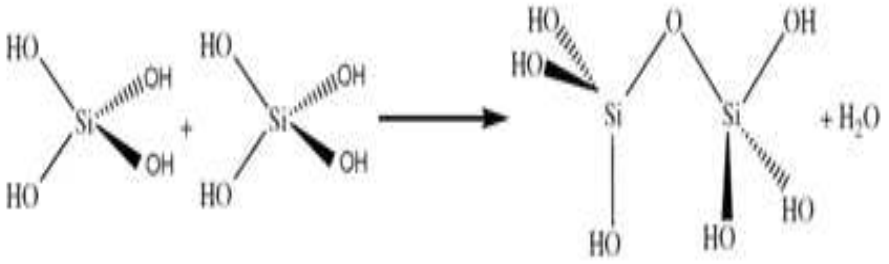

Figure 2.8: Water condensation

•From the condensation of an ethoxy group (Si-OR) and a silanol group (Si-OH) a siloxane bridge is created (Si-O-Si) with the releasing of an ethanol molecule (R-OH), figure2.9.

The synthesis of a silica thin film is achieved by a reaction catalysis in acid environment (PH<7), where the acid sol favors the condensation process through polymerization of monomers (figure2.10), [9]. The result is a gel, solid and transparent like a glass.

Protocol used for the synthesis of the sol-gel silica

Experimental protocol of silica sol gel synthesis is described in this section.

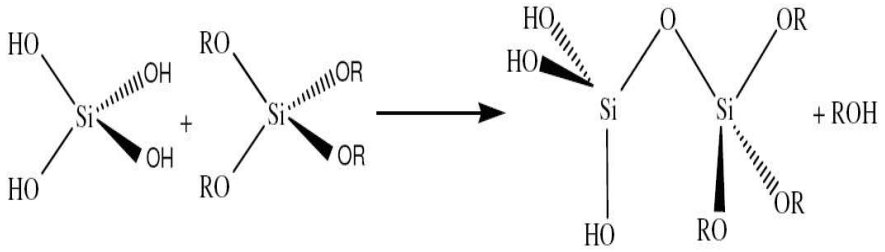

Figure 2.9: Alcohol condensation

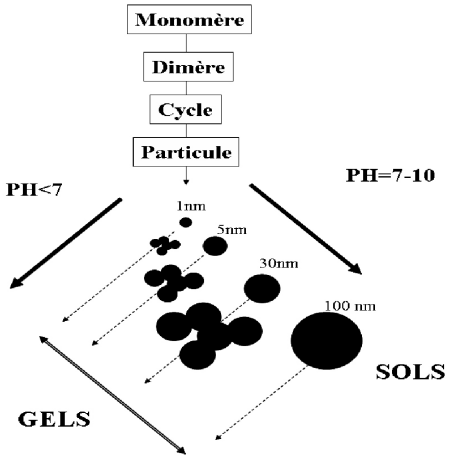

Figure 2.10: Polymerization of aqueous silica

First, a solution composed of 25 ml of tetraethoxysilane (TEOS), 15 ml of Ethanol and 8 ml of water in molar ratio 1, 2.4, 4, is prepared. Hydrolysis is obtained by heating the solution at 60°C for 1 hour. As the condensation kinetic depends on the PH, to slow-down the process a PH of 2.5 is used. Moreover, to avoid the rapid polymerization of the sol tetra-hydro-furanne (THF) is also used. Thus, after 1 hour the following actions are done: i) 50 ml of THF is added to the solution, which is then evaporated at 40°C until it becomes viscous. ii) 50 ml of THF are again added to the solution. A second evaporation step of about 5 minutes is done. iii) finally, after a third addition of 50 ml of THF, the solution is filtered to remove all impurities. The obtained sol is kept at low temperature and used shortly after the synthesis.

Silica deposition onto a silicon substrate

Once the sol is synthesized, it is used to obtain the first silica layer. The silica layer is deposited onto a silicon substrate to facilitate the following TEM preparation and observation. The deposition of the sol is obtained by using the spin coating method. This consists in depositing of a small drop of sol onto the substrate, which is fixed to a rotating holder. During the spin-coating process, most of the sol is ejected from the substrate. The remaining one favors the formation of a homogeneous thin film of silica. The thickness of the silica layer is function of the spin velocity and the duration of the spin-coating process, but also of the viscosity of the gel. Here, 4000 rpm for 120 s. Afterward, the silica layer is densified by annealing the sample in air at 450°C during 1 h, [10]. Finally, the thickness of the silica layer is measured by ellipsometry to be about 265 nm.

2.2.2 Plasma enhanced chemical vapor deposition (PECVD) silica synthesis

The second method is the plasma enhanced chemical vapor deposition (PECVD). PECVD was used as an alternative route to the sol-gel deposition as we found that at high temperature the sol-gel silica becomes instable. This will be discussed in section 5. The PECVD is a process used to deposit thin films in a solid phase using chemical reactions of precursors in the gaseous phase, [11]. A plasma is created by exciting with a microwave field a gas submitted to a magnetic field. During the excitation, energetic electrons can dissociate and ionize neutral precursors, e.g. atoms and molecules. The plasma commonly used in deposition reactors is the cold plasma, i.e. the temperature of the neutrals and ions is lower than 5000 K. It is composed of relatively hot electrons (several eV) and less energetic molecules, radicals and ions.

ECR-PECVD Reactor : Venus

Deposition of silica has been performed using the Venus reactor at PICM laboratory located at Palaiseau. A schematic of the venus reactor is presented in figure 2.11. It consists of a 70 liters cylindrical stainless steel chamber with an internal diameter of 40 cm. The chamber is equipped with a plasma source at the top, a manual gate valve at the bottom separating the reactor from the turbo-molecular pump, a front loading door and several vacuum, optical and electrical ports for vacuum gauges, plasma and deposition characterization and control.

The microwave discharge at 2.45 GHz is sustained by a set of sixteen water-cooled linear antennas arranged in a 4x4 matrix. Two magnetrons generating up to 2000 Watts each are used to supply power to the microwave antennas. The injection of precursor gases is done at two levels: oxidant gases

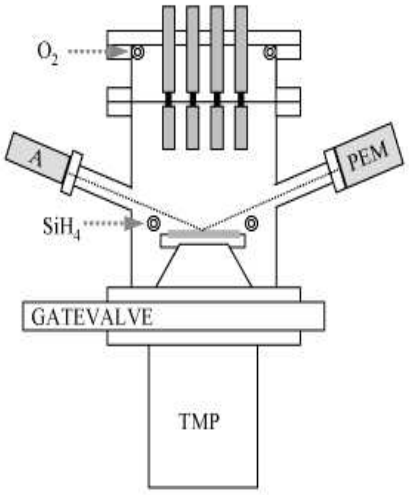

Figure 2.11: Venus reactor

(N_2 and O_2), etch-clean gases (SF_6/O_2 mixture) and argon are injected at the top of the reactor, where the most intense electron cyclotron resonance (ECR) regions are located. The silane (SiH_4) is injected downwards through a circular ring just above the level of substrate.

Deposition conditions

A 300 nm layer of silica is deposited onto a silicon wafer substrate (111) by ECR-PECVD technique. The precursor gases used during the deposition are SiH_4 and O_2. The gas flows are 8 and 40 sccm (standard cubic centimeter per minute), respectively. The pressure of initial gas introduced in the chamber is 1.5 mTorr and the power delivered by two magnetrons was set to 500 Watt. The deposition was performed at room temperature and the time required to depose 500 nm of silica is about 10 min. Ellipsometry was used afterward to check the thickness of the film.

2.3 Grafting of the NPs

In the previous sections, the first and the second steps in the fabrication of our model system have been detailed. Namely, the chemical synthesis of Au NPs with a defined size and a narrow size dispersion and the deposition of a thin silica layer onto a silicon substrate. In this section, we will describe the third step, i.e. the grafting of the NPs at the silica surface and the control of their density. First, we describe the protocol used for 15nm Au

NPs. For smaller (3.5nm) Au NPs, we only describe the differences with respect to this protocol.

2.3.1 15 nm gold NP

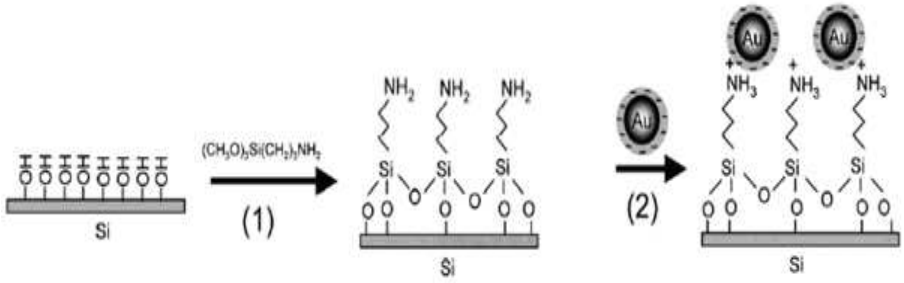

Figure 2.12: Grafting of gold NPs onto silica surface[12].

In order the Au NPs to be grafted, the silica surface is functionalized to create a chemical affinity with the citrate capping the NPs. Moreover, as the silicon substrate is not transparent to the light, Au NPs are also grafted onto microscopy glass slides for the optical absorption analysis.

Figure 2.12 illustrates the different steps to graft the Au NP at the silica surface. First, the silica surface is treated with a piranha solution (H_2S0_4+H_2O_2) to create silanol groups (Si-OH). The piranha solution is obtained by mixing one volume of hydrogen peroxide (H_2O_2) to three volumes of sulfuric acid (H_2S0_4). The sample is dived into the solution for few minutes (2-5 minutes) and then rinsed with distilled water. The importance of this treatment resides in the transformation of the surface from hydrophobic to hydrophile. The presence of Si-OH groups permits to functionalyze the surface with aminosilane groups (NH_2) by the reaction with alkoxysilane group. These will be used as surface coupling agents to trap the Au NPs at the silica surface. This process, called *silanisation*, consists in the immersion of the sample for 2h at room temperature into a solution containing 2.2 ml of amino-propyl trimethoxysilane (APTES) and 6 ml of absolute ethanol. The sample is then removed from the solution and cleaned in methanol and distilled water. At the end of the process, the amine functions (NH_2) are situated in the extremity of the molecular chains and connected to the surface through siloxane bridges (Si-O-Si).

The grafting of the NPs onto the silica surface is obtained by simple immersion of the functionalyzed sample into the solution containing the Au NPs. Within the solution, the negatively charged citrate thin film coating the Au NPs interacts with the positively charged amine functions of the silica. Thus, Au NPs are electrostatically trapped at the sample surface.

With this method, we obtain NPs which are homogeneously distributed and isolated throughout the silica surface. However, if the surface is not properly cleaned, the freely diffusing silane groups can favor the aggregation of Au NPs rather then their individual grafting. Finally, samples are annealed at 450°C for 1hour in order to calcinate all organic species present at the silica surface.

The relationship between the grafting time and the density of grafted NPs is studied using both optical absorption analysis and scanning electron microscopy (SEM) for three different grafting times: 15, 30 and 45 min. For the optical analysis the measurements were done on optically transparent microscopy glass slides. The changing of the color of the slides from transparent to red is the signature that NPs have been grafted. Correspondingly, the absorption spectra show an increase of the absorption peak with the time, underlying the fact the density of the grafted NPs increases with time, figure2.13. Finally, the stability of the grafted NPs is indicates by the fact that the width of the absorption band does not change with time.

Table 2.1: Density of grafted NPs onto silica surface as a function of the NP size.

NP size (nm)	NP density (μm^{-2})	Grafting time (minutes)
3.5	7500	120
15	370	30

Figure 2.14 shows SEM images corresponding to different grafting times. As expected, the longer the grafting time, the higher the NPs concentration at the sample surface. In table2.1 the NP density for the different initial sizes are reported. These values correspond to the optimum densities used in this thesis.

2.3.2 3.5 nm gold NPs

The synthesis for the 3.5nm Au NPs is nearly the same as for the 15nm Au NPs, thus they can be grafted following the protocol developed in the previous section, exploiting the electrostatic interactions between the citrate capping Au NPs and and the amine (NH_2) function of the functionalyzed silica surface.

However, because of the smallness of the NPs neither optical analysis nor SEM observation can be done. The pink color of the glass slide is the only indication that grafting succeeded. Thus, the density of the NPs can only be checked afterward, i.e. once the NPs are embedded within the silica matrix, using TEM analysis in planar view as explained in the following sections.

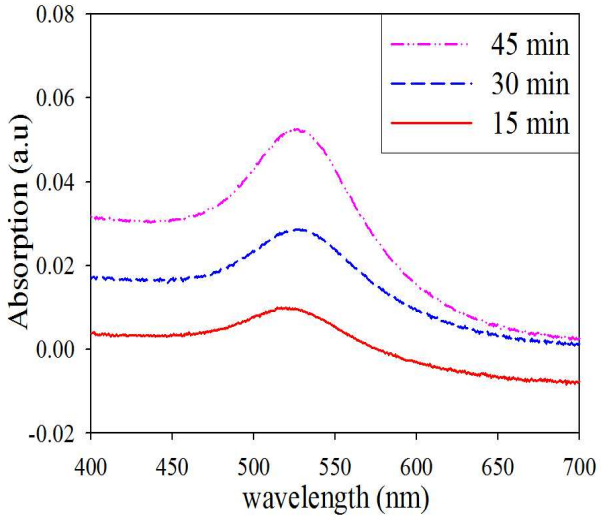

Figure 2.13: Optical absorption corresponding to different grafting times for 15 nm gold nanoparticles.

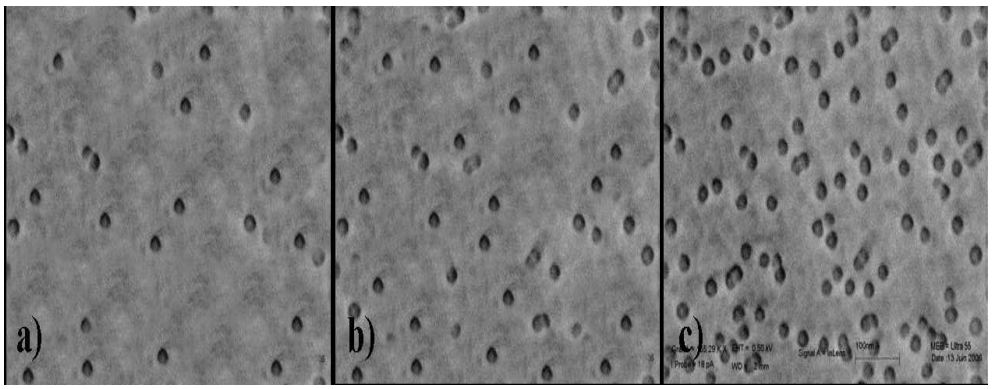

Figure 2.14: SEM view of grafted 15 nm NPs at different grafting times: a) 15 min, b) 30 min, c) 45 min.

2.4 Embedding NPs

The next step is the confinement of the NPs within the silica matrix. This is archived by deposing a second silica layer under the same conditions as the first one, i.e. using either sol-gel or PVECD deposition methods. In this way the NPs are confined at a unique plane below the sample surface at a depth that will depend on the thickness of the second layer. For our purposes the layer thickness was chosen to be of 300nm.

2.5 Annealing treatment and sample stability

The last step is the annealing treatment. It has a twofold objective: i) to densify the silica matrix and ii) to drain the residual gold solute toward the NPs. As they may influence the sample stability, annealing temperature, atmosphere and time must be accurately chosen. For this reason, the thermal stability of the samples has been be checked for both the deposition methods, i.e. sol gel and PECVD, and for the different NP sizes.

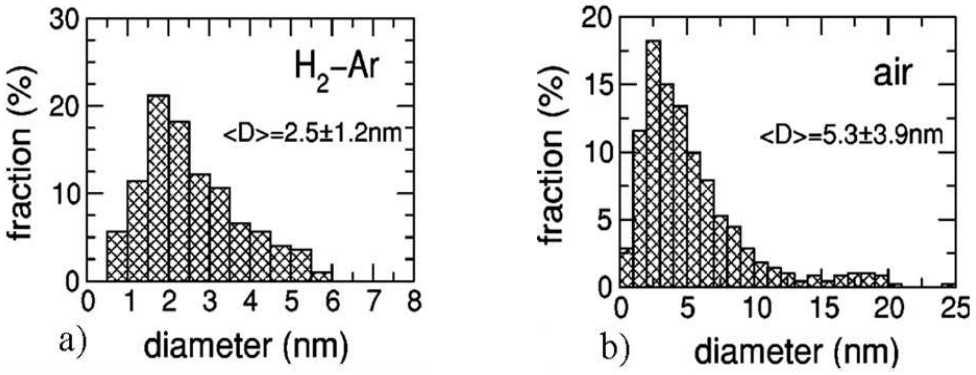

Figure 2.15: Size histograms after 1h annealing at 900°C in a) H_2-Ar and b) air, [13]

The influence of the annealing atmosphere on the evolution of embedded Au NPs has been studied in detail by Miotello et al, [13], figure 2.15. They observe that annealing at 900°C for 1 hour under air favors the growth of the NPs, whereas annealing under reducing atmosphere, H_2-Ar, does not appreciably change their size distribution. Thus, thermal treatment in H_2-Ar atmosphere during 1 hour is chosen.

Typically, silica is stabilized annealing the sample at 450°C for 1 hour. This treatment is also sufficient to deplete the matrix from the residual gold solute. This is shown for example in figure 2.16 for 15nm Au NPs embedded in both sol-gel and PECVD silica thin films. However, sol-gel silica becomes instable, e.g. bubbles are formed, when annealing is performed at higher temperatures, figure 2.17a). Moreover, for sol-gel silica some granular structures are also observed (figure 2.18). Electron diffraction analysis indicates that these grains are amorphous. Varying the annealing temperature between 500°C and 900°C, we observe that these structures are absents at 500°C and progressively *grow* with temperature to occupy about 60% of the sample surface at 900°C.

On the other hand, PECVD silica is stable at least up to 900°C, figure 2.17b). For this reason, PECVD silica is used for the irradiation at high temperature. To summarize, both systems have been annealed for 1 hour under Ar_2-H atmosphere. Sol-gel samples at 450°C, whereas PVECD samples

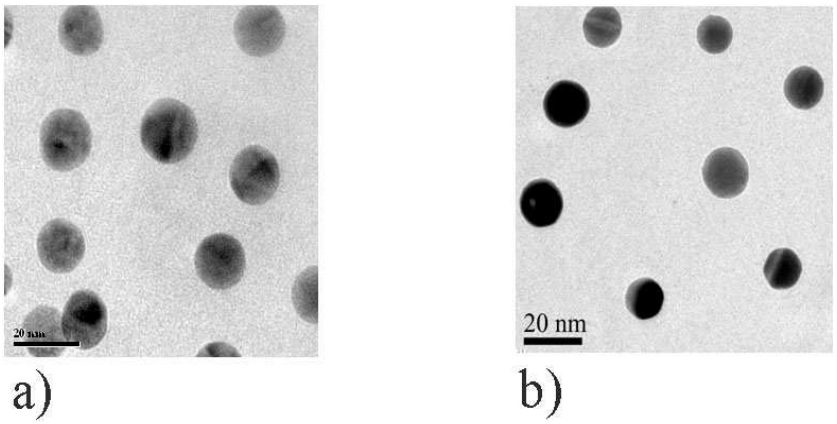

Figure 2.16: TEM plane view of 15 nm Au NPs embedded within a) a sol gel and b) a PECVD silica matrix. Sample has been annealed at 450°C for 1h.

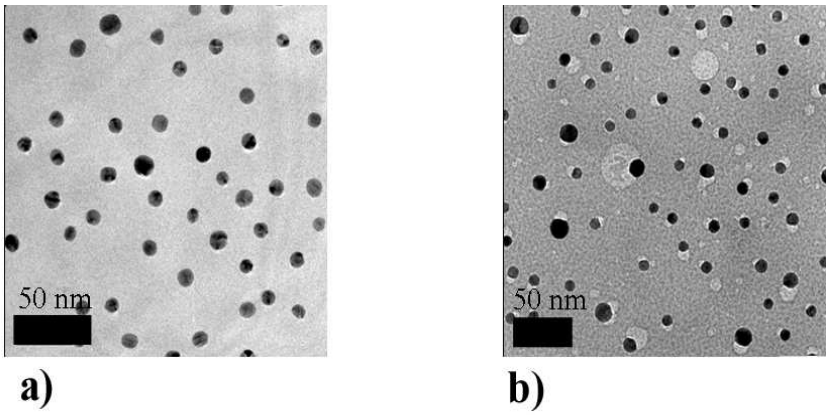

Figure 2.17: TEM plane view of 15 nm Au NPs embedded within a) PECVD, and b) sol-gel silica matrix after annealing at 900°C for 30 min under Ar/H atmosphere.

at 900°C, and then analyzed having recourse to the transmission electronic microscopy (TEM).

Concerning the thermal stability of the embedded NPs, the 15 nm Au NPs are stable up to 900°C. However, for 3.5nm Au NPs, we observe a spreading of the size distribution toward larger sizes associated with a decrease of the density of the NPs. This ripening process broads the size dispersion of the NPs, and thus reduces the *advantages* of using our model system. Thus, for 3.5 nm Au NPs annealing treatments were limited to 450°C.

All the annealing conditions have been reported in table2.2.

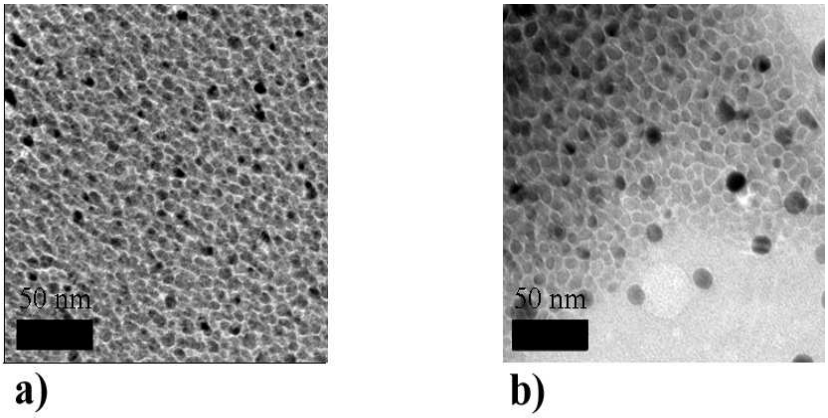

Figure 2.18: TEM plane view of Au 15 nm NPs embedded within a sol-gel silica matrix after annealing at a) 600°C, and b) 900°C for 30 min under Ar/H atmosphere.

Table 2.2: Annealing conditions.

Size (nm)	Sol-gel	PECVD	Atmosphere
3.5	-	450°C	H_2-Ar
15	450°C	900°C	H_2-Ar

2.6 Sample characterization

2.6.1 Transmission Electron Microscopy

The purpose of this section is to introduce the transmission electron microscopy (TEM) and the different related techniques used for the study of the embedded NPs under irradiation. When electrons are accelerated up to high energy levels (few hundreds keV) and focused on a material, they can scatter or backscatter elastically or inelastically, or produce many interactions, source of different signals such as X-rays, Auger electrons or light, see for example figure 2.19. Some of them are used in transmission electron microscopy (TEM). This section is concerned with electron diffusion and diffraction and the contrast image formation in a conventional TEM (bright/dark field modes, and diffraction patterns). Finally, the sample preparation both in plane and cross section are described as well as the protocol used for the treatment of the numerical images.

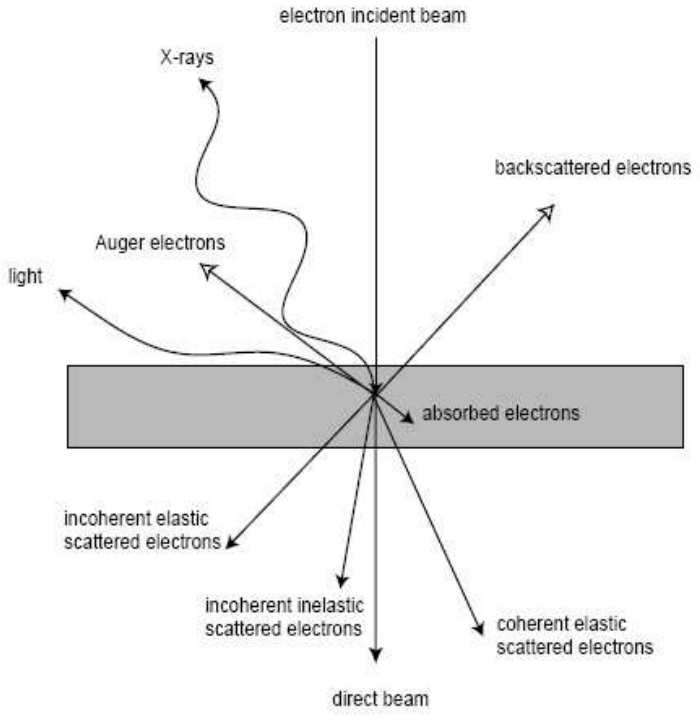

Figure 2.19: Signal generated by the impinging electrons interacting with the target atoms.

2.6.2 Historical introduction

The resolution ρ of a microscope is defined as the distance between two details just separable from one another. It can be calculated using the Abbe theory of images formation for optic systems. For incoherent light or electron beam:

$$\rho = \frac{0.61\lambda}{sin\alpha} \tag{2.1}$$

where λ is the wavelength of the light, and α the maximum angle between incident and deflected beam in the limit of the lens aberrations. For optical microscopy, the resolution is therefore limited by the wavelength of light (410-660 nm). The X or γ rays have lower wavelength, but unfortunately, high-performance lenses necessary to focus the beam to form an image do not exist yet (however, X-rays can reveal structural information of materials by diffraction techniques). In 1923, De Broglie showed that all particles have an associated wavelength linked to their momentum: $\lambda = h/\mathrm{m}\nu$ where m and ν are the relativist mass and velocity respectively, and h the Plank's constant. In 1927, Hans Bush showed that a magnetic coil can focus an

electron beam in the same way that a glass lens for light. Five years later, a first image with a TEM was obtained by Ernst Ruska and Max Knoll. In a TEM, the electrons are accelerated at high voltage (100-1000 kV) to a velocity approaching the speed of light (0.6-0.9 c); they must therefore be considered as relativistic particles. The associated wavelength is five orders of magnitude smaller than the light wavelength (0.04-0.008). This resolution enables material imaging and structure determination at the atomic level. Many different techniques based on TEM are used in materials science. Some of them will be detailed in the following sections.

2.6.3 The transmission electron microscope

A transmission electron microscope is constituted of: i) a vacuum system, ii) a gun to create the electron beam, iii) an ensemble of electromagnetic lenses and iv) a viewing system to capture the image, e.g. a fluorescent plate, a photographic film or a CCD camera. These elements will be briefly described in the next sections.

Vacuum system

To increase the mean free path of the electron gas interaction, a standard TEM is evacuated to low pressures, typically on the order of 10^{-5} Pa. The need for this is twofold: first the allowance for the voltage difference between the cathode and the ground without generating an arc, and secondly to reduce the collision frequency of electrons with gas atoms to negligible levels. The vacuum system for evacuating a TEM to an operating pressure level consists of several stages. Initially a low vacuum is achieved with either a rotary vane pump or diaphragm pumps bringing the TEM to a sufficiently low pressure to allow the operation of a turbo-molecular or diffusion pump which brings the TEM to its high vacuum level necessary for operations. Sections of the TEM may be isolated by the use of gate valves, to allow for different vacuum levels in specific areas. This can vary from 10^{-4} to 10^{-7} Pa or higher (10^{-9} Pa) in the electron gun field emission TEMs.

Electron gun

Two kind of sources, or filaments, can be used to generate the electron beam: i) the thermo-ionic and ii) the field emission sources. In the former electrons are produced when the source is heated in the latter they are produced when a large electric potential is applied.

These sources are part of an assembly which is called the gun. In particular, for this work we used a CM30 microscope equipped with a thermo-ionic gun. This is composed of three parts, namely the filament (cathode), the wehnelt and the anode as shown in figure 2.20). Among the different cathodes available our microscope is equipped with an LaB_6 crystal as a filament.

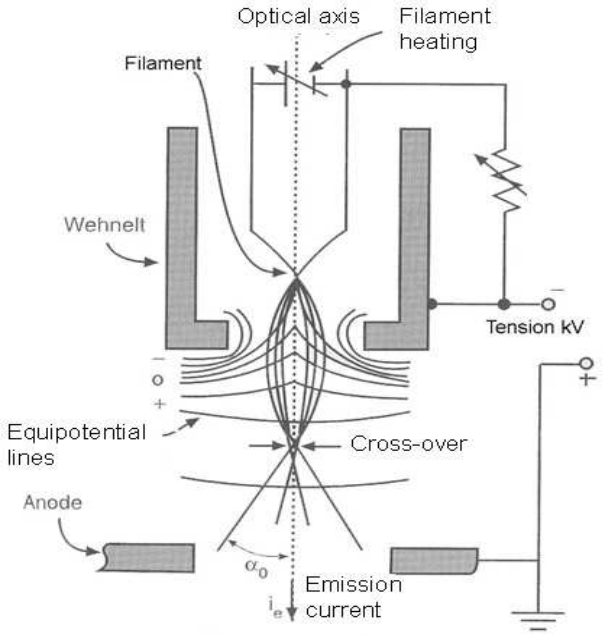

Figure 2.20: Schematic of an LaB_6 electron gun

The cathode is at negative potential, here 300kV, with respect to the anode which is at the earth potential. The electrons, extracted from the tip of the LaB_6 crystal by thermo-ionic emission, are accelerated toward the anode. A cylindrical grid (wenhelt), put at an intermediate position and to a more negative potential (Bias) than the cathode, is used as an electrostatic lens to focalize the beam into a virtual point above the anode. This point is called cross-over and can be considered as the virtual source of the electron beam. The electron beam is defined by certain characteristics which are controlled by the source itself. These are the brightness, the energy spread, the temporal and spatial coherency and the source size.

Electromagnetic lenses

Electromagnetic lenses are designed to act in a manner emulating that of an optical lens, by focusing parallel rays at some constant focal length. The lenses are cylindrical in shape with a hole in the center (the optical axis) to allow the passage of the electron beam. A coil inside the lens creates an magnetic field. Moreover, it acts directly on the electron trajectory, which are deviated following the Lorentz's law:

$$\mathbf{F} = e\mathbf{v} \times \mathbf{B} \tag{2.2}$$

where e is the electron charge, $\mathbf{v}$ the electron velocity and $\mathbf{B}$ the applied magnetic field. In particular, by changing the current inside the coil the magnetic field is changed and thus the lenses strength. It is critical that the electromagnetic lens is radially symmetric, as deviation from this configuration causes astigmatism and worsens spherical and chromatic aberrations, which in turn reduce the quality of the image. A conventional TEM possesses several electromagnetic lenses positioned at different stages along the column. From the top to the bottom, they can be divided in three categories: i) two condenser lenses (C1 and C2) to focus the electron beam on the sample, i.e. the illumination system, ii) an objective lens to form the diffraction pattern in the back focal plane and the image of the sample in the image plane, iii) some intermediate lenses to magnify the image or the diffraction pattern on the screen.

Imaging mode

TEM images were digitally acquired using a low-scan charge coupled device (CCD) camera GATAN multiscan.

2.6.4 Conventional transmission electron microscopy

Essentially, two observation methods can be use to investigate the NPs in conventional (low magnification) transmission electron microscopy: i) the imaging and ii) the diffraction mode. Imaging mode was applied to study the evolution of the NPs under irradiation whereas diffraction mode was used, when necessary, to check either the reaction products, or impurities, of the chemical synthesis or the crystallinity of the observed nano-objets.

Imaging mode

If the sample is thin, e.g. <200 nm, and constituted of light chemical elements, the image presents a very low contrast when it is focused. To obtain an amplitude contrasted image, an objective diaphragm is inserted in the back focal plane to select the transmitted beam (and possibly few diffracted beam): the crystalline parts in Bragg orientation appear dark and the amorphous or not Bragg oriented parts appear bright. This imaging mode is called bright field mode BF. If the diffraction is constituted by many diffracting phases, each of them can be differentiated by selecting one of its diffracted beams with the objective diaphragm. To do that, the incident beam must be tilted so that the diffracted beam is put on the objective lens axis. This mode is called dark field mode DF. The BF and DF modes are used for imaging materials to nanometer scale. In this work, most of the observations were done using magnifications in the range of 30-200kX.

Diffraction mode

The selected area diaphragm is used to select only one part of the imaged sample for example a particle or a precipitate. This mode is called selected area diffraction SAED. The spherical aberrations of the objective lens limit the area of the selected object to few hundred nanometers. Nevertheless, it is possible to obtain diffraction patterns of a smaller object by focusing the electron beam with the projector lenses to obtain a small spot size on the object surface (2-10 nm). The spots of SAED become disks whose radii depend on the condenser diaphragm. This is called microdiffraction. SAED and microdiffraction patterns of a crystal permit to obtain the symmetry of its lattice and calculate its interplanar distances using the Bragg law.

2.6.5 Sample preparation

For TEM observations, thin samples are required due to the important absorption of the electrons in the material. In order to observe the first phases of the nucleation and growth of the precipitates under irradiation the sample must be thin enough. We estimate this thickness to be of the order of 100nm. All our samples were prepared using the mechanical polishing (tripod) followed by an ion sputtering (PIPs) treatment:

Two different preparation methods were used here:

i) to study the nucleation and growth of the NPs under irradiation, the samples were prepared in plane section

ii) to study the depth distribution of the precipitates, the samples were prepared in cross section.

Plane section view

First, the sample is cut with a diamond saw to form a square of length $2.5mm$. The surface of the sample, i.e. the silica layer containing the Au NPs, is then glued onto a copper grid with an internal hole of $1.5mm$ with the G1/G2 GATAN epoxy resin and cured at 90°C for 30min. In the next step, the copper grid supporting the sample is glued with a crystal wax onto the pyrex insert of a tripod. The polishing process occurs when the sample is put in contact with a rotating diamond disk fixed on a polisher plate holder. Here, the tripod is used to maintain the sample on the disk during the mechanical grinding. The velocity of the polishing process will depend on both the grain size of the diamond disk and the angular velocity of the plate holder. Particular attention must be payed that the tripod is perfectly planar, in order to avoid preferential grinding of the sample. This method allows the silicon substrate to be mechanically removed down to few microns of thickness and the silica layer, embedding the NPs, to be preserved. We start with a disk containing diamond grains of about 30μm and with a velocity of 50 rpm (rotations per minute). Both are progressively reduced down to

0.5μm and 10 rpm for diamond disk and the rotation velocity, respectively. At the end of the process the sample thickness is about 2μm. The latter is controlled by using an inverted microscope and measuring the difference in focus between the surface of the sample and that of the supporting copper grid. The sensibility of the measure is about 1μm. Finally, the sample is removed from pyrex insert by simple immersion into acetone for few minutes.

Ion-polishing is then used to gently reduce the sample thickness down to electron transparency. For the ion milling process, a GATAN Precision Ion Polishing System (PIPS) is used. Here, two focussed Ar ion beams mill the sample in such a way that a hole results at the desired position. In general, the parameters for the ion milling process are rather specific for each material and have to be optimized. The ion milling rate increases with higher etching angle and higher etching voltage; however, the sample is also more severely damaged. Therefore, the angle as well as the voltage should be kept rather low. Generally, a higher voltage combined with lower angle is less harmful to the sample than lower voltage combined with higher angle.

For our samples in plane section, the two Ar guns are used to erode (sputter) the silicon substrate, i.e. both are directed toward the silica layer with an angle of $+7°$ and an energy of 3 keV. As soon as a hole is created, the two Ar guns are used in opposite directions with an attacking angle of $\pm$ 3° and an energy of 3 keV. For this second step, the ion-polishing time is generally limited to 5 minutes. This insures the sample to be sufficiently thin for TEM characterization.

Cross section view

The sample preparation in cross-section necessitates the following steps: two squares of surface $2.5\times2.5mm^2$ are cut with a diamond saw and then glued face to face with G1/G2 GATAN epoxy resin and cured at 90°C for 30min under a press. In general, to protect the sample, two additional silicon pieces are additionally glued to form a four layers sandwich. the sample is then cut into slices, e.g. 1mm thick. One of the face of the slice is then optically polished and glued onto a copper grid. At this point, the ensemble grid+slice is glued onto a tripod pyrex and mechanically polished till the thickness of the slice is reduced to 3-4μm. The samples are then put into a PIPs. For cross section preparation, the two Ar guns are used in opposite directions with an attacking angle of $\pm$ 3° and an energy of 3 keV till the hole reaches the interfaces containing the NPs.

Imaging treatment

Samples, either in plane or cross section, are observed in a transmission electron microscope, and the images are collected using a CCD camera (GATAN multiscan). To maximize the useful information contained in the

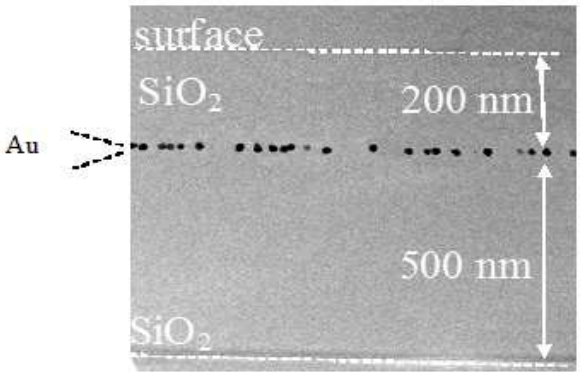

Figure 2.21: Cross-section TEM micrograph of Au NPs embedded within a unique plane at 200 nm below the silica surface.

micrographs an additional numerical treatment is necessary. The idea is to have all the worth information in black and the rest in white. This process is called binarization (figure 2.22).

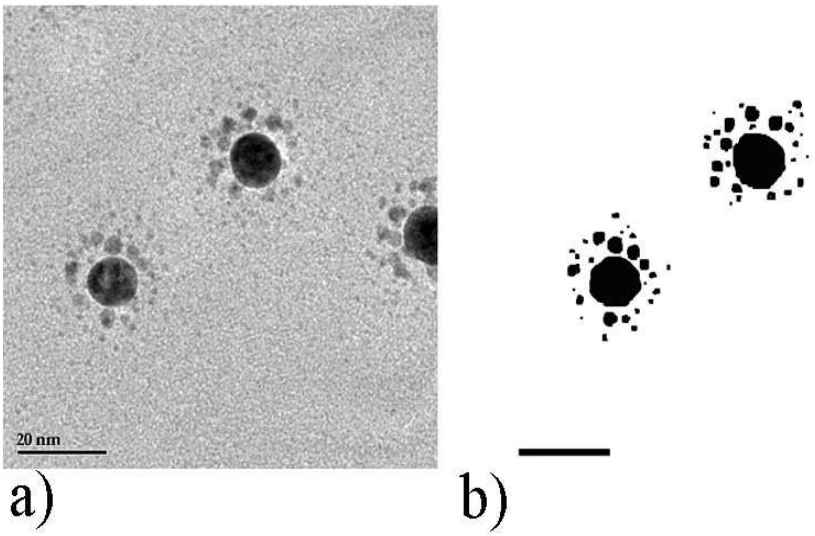

Figure 2.22: a) TEM micrograph of an irradiated samples, b) binarized image. All the worth information is in black the rest in white.

In general, this treatment is done using automatic or semi-automatic programs. However, in our case, the non homogeneity of the image contrast and, for the irradiated samples, the superposition of the precipitates, renders this approach difficult and in general not exploitable. For this reason, each TEM micrograph is manually treated using the following protocol: a numerical micrograph in TIFF format is imported to Photoshop program,

where a calque is generated, i.e. a transparent sheet which is superposed to the original image. The useful information is then obtained by individually coloring each particle. For superposed particles, two or more calques are used. The longer time required for the treatment is counterbalanced by the precision of the measure. The calque is then separated from the original image and imported to ImageJ program, which is used to obtain the important parameters associated to the NPs, i.e. diameter, area, density, etc. The scalebar of the original micrograph is used as a reference for the conversion pixels-to-nanometers. The effective dimension of a NP, e.g. its diameter, can be easily determined when it has a perfectly spherical morphology, i.e. a perfect circle on the micrograph. However, this is no true for particles of different shape. For this reason the mean diameter of a particle is estimated by considering the mean value of its minimum and maximum diameters:

$$D_i = \frac{D_i^{max} + D_i^{min}}{2} \tag{2.3}$$

The evolution of the size distribution function with fluence allows to investigate the nucleation and growth of a precipitate phase under irradiation. Thus, for each fluence, the size distribution function is obtained by importing the sheet containing the diameters of measured NPs to Sigma plot program. To have a good statistics generally 300 to 500 NPs are analyzed. Distributions are then normalized to the total number of measured NPs, such as f_i=N_i/N_{tot} represents the frequency of the event i. The average size of the precipitates is then given by:

$$\overline{D} = \frac{\sum_i n_i D_i}{N_{tot}} = \sum_i f_i D_i \tag{2.4}$$

and the standard deviation is:

$$\sigma = \sum_i \frac{n_i (D_i - \overline{D})^2}{N_{tot}} \tag{2.5}$$

2.7 Irradiation

2.7.1 ARAMIS accelerator

The ensemble of the irradiations were performed using the ARAMIS accelerator, located at the CSNSM laboratory in Orsay (France), [14], figure2.23. ARAMIS accelerator may work into two operation modes: i) the Tandem and ii) the Van der Graaf mode.

-**Tandem mode**: Negatively charged ions are produced by sputtering from a solid cathode target. Charged cesium ions, C_s^+, are used as incident beam: a plasma, created from Cs vapor from a molten C_s reservoir, is accelerated toward the negatively biased cathode (-5kV). The ejected ions are

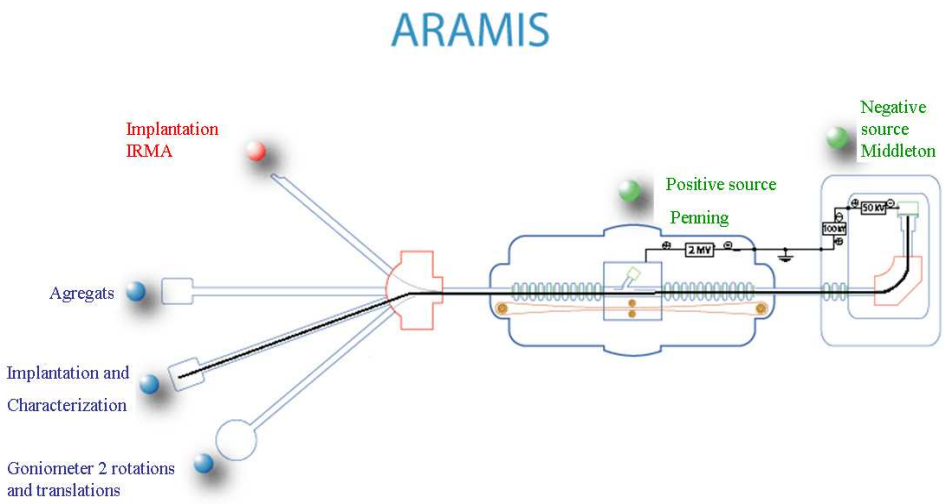

Figure 2.23: ARAMIS accelerator.

accelerated away from the cathode by a potential of 150kV and selected in mass and energy with a 90° bending magnet. They are then accelerated a first time within the accelerator tank using tunable voltage up to 2MV, figure 2.24. Negatively charged ions are stripped using a nitrogen gas becoming positively charged. The positive ions are then repelled by the positive terminal and receive an additional acceleration toward the end of tank reaching a total energy of (n+1)U MeV, where n is charge state and U the voltage of the terminal. An analyzing magnet is used to select the desired charge state of the ions and to direct the beam into the selected experimental chamber.

-**Van der Graaf mode**: In this mode the ion beam is produced into the terminal of the accelerator using a positive ion source, e.g. the Penning source. A plasma is created by introduction a gas (H, He or N) into the terminal of the accelerator tank. The positively charged ions are then accelerated toward the end of the tank, selected in charge and directed toward the experimental chamber.

2.7.2 Irradiation conditions

Irradiation was performed using the *implantation and characterization* line. The sample surface is homogeneously irradiated using an ion-beam scanning system. A diaphragm of $1cm^2$ is put in front of the sample in order to insure a good precision on the surface to irradiate. Samples were irradiated with 4MeV Au^{2+} and 4MeV Br^{2+} ions for fluences up to $8x10^{16}$

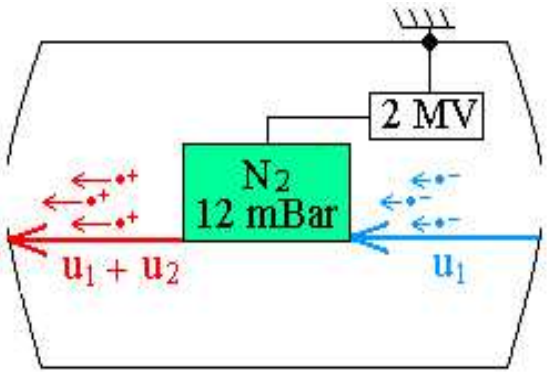

Figure 2.24: Ion accelerated into the tandem tank.

cm^{-2} under a flux 1 $\mu A.cm^{-2}$. The irradiation temperatures were varied from 30°C up top 800°C. (Table2.3).

Table 2.3: Summary of the irradiation conditions.

Ion	Temperature (°C)	Ion energy (MeV)	Flux (µA.cm^{-2})	NPs Size (nm)	NPs density (µm^{-2})
Au^{2+}	25	4	1	3.5	7500
				15	370
	500	4	1	3.5	7500
	600			15	370
	800				
Br^{2+}	600	4	1	15	370
	800				

The nuclear and the electronic stopping power for both Au and Br ions in both Au NPs and SiO_2 matrix were calculated with the code SRIM 2008, [15]. The values are reported in table2.4. In both cases, the implantation depth (R_p~1±0.1 μm) is at least 3 times the depth at which the NPs are confined (320 nm), thus preventing the interaction between the implanted species and the embedded NPs. The samples were analyzed in a 300 KeV Philips CM30 microscope. TEM micrographs were processed with a slow-scan CCD camera and analyzed with the Digital micrograph program. The

Table 2.4: Stopping powers for the used ions. Sn is the nuclear stopping power and Se the electronic stopping power as estimated from the code SRIM 2008, [15], for both Au NPs and SiO_2 matrix.

Ion	Energy MeV	Sn^{Au} (keV.nm^{-1})	Se^{Au} (keV.nm^{-1})	Sn^{SiO2} (keV.nm^{-1})	Se^{SiO2} (keV.nm^{-1})
Au^{2+}	4	7.5	3.6	2.0	2.2
Br^{2+}	4	1.2	3.3	0.32	1.9

average size of the NPs and their size dispersion have been estimated by considering the protocol of imaging treatment introduced in section 2.6.5.

2.8 Conclusion

In this chapter the fabrication of a model system had been described. This system is composed of chemically synthesized Au NPs sandwiched between two silica layers. The advantages of using this model system are of three kinds: i) nearly monodisperse NPs can be obtained using the chemical synthesis, ii) the NP density can be varied by changing the grafting time and iii) the depth at which NP are confined can be chosen by varying the thickness of the second silica layer. The thermal stability of the samples was investigated. It was shown that PECVD silica is stable up to 900°C, whereas sol-gel silica became instable above 450°C. Samples are characterized by conventional TEM in plane and cross section view. Finally, the TEM principles, the imaging treatment protocol and the ARAMIS accelerator are briefly introduced.

Bibliography

[1] M.C. Daniel, D.Astruc, Chem.Rev. 104, (2004) 293

[2] N.R Jana, L.Gearheart, C.J. Murphy, Langmuir 17 (2001) 6782

[3] J.Turkevich and al. Discuss. Faraday Soc. 11(1951)

[4] J.P Abid , Thesis (2003)

[5] U.Kreibig , M. Vollmer Optical Properties of Metal Clusters, springer ed. (1995)

[6] W.H Zachariasen, The atomic arrangement of glass J.Amer.Chem.soc. 54 (10) (1932) 3841-51

[7] Revue Verre, vol 6 issue 5(2000)

[8] C.J Brinker, G .W Scherer, Sol gel Science (1990)

[9] R K Iler, The chemistry of silica (Wiley, New York, 1979)

[10] R. Bruckner, J.of non cryst.solids 5 (1970) 123-175

[11] B. Haj Ibrahim, Thesis (2007), LPICM, Ecole Polytechnique.

[12] S. Liu, T.Zhu, R. Hu and Z. Liu, Phys. Chem. Chem. Phys., 2002, 4, 6059 - 6062

[13] A. Miotello, G.De Marchi, G.Mattei, P.Mazzoldi, C.Sada, Phys.Rev.B, 63, 075409 (2001)

[14] E.Cottereau, J.Camplan, J.Chaumont, R.Meunier and H.Bernas, Nucl. Instr. Meth. Phys. Res. B 246 (2006) 30

[15] J.F. Ziegler, J.P. Biersack, and U. Littmark, The Stopping Ranges and Ranges of Ions in Solids Pergamon Press, New York, 1985; www.srim.org.

Chapter 3

Ion Beam Irradiation of Embedded Nanoparticles: Toward an in-situ Control of Size and Spatial Distribution

Abstract

Irradiation of chemically synthesized Au nanoparticles (NPs) embedded within a dielectric matrix promotes the formation of a halo of satellites around the original cluster. We show that the complete dissolution of the NPs results in the formation of a narrow size distribution of small precipitates with a mean size of 2 nm and a standard deviation of 0.4 nm. By combining the chemical synthesis of the NPs and the irradiation to induce their dissolution and precipitation, we give a guideline method for overcoming the difficulty of controlling the size and spatial distribution of the embedded NPs associated with ion implantation technique. In particular, we show that the irradiation can be used to tailor the size of the already formed NPs. Moreover, we establish that the evolution of the satellite clusters under irradiation can be described by a two step process. These are discussed in terms of classical and inverse Ostwald ripening mechanisms.

3.1 Introduction

NPs embedded within a dielectric matrix are particularly interesting because of their non linear optical properties with high potential for application in optoelectronic field, [1]. Moreover, as the surface plasmon resonance depends on the NPs size as well as their chemical surrounding, tunable properties of metal particles became of primary importance for application in nanoelectronics, [2].

Among different possible techniques, ion-beam synthesis (ion-implantation and ion-mixing) proved to be suitable in obtaining NPs based materials. However, during ion implantation, the uncontrolled nucleation and growth processes result in a broad spatial and size distribution of NPs and reduces the possible practical applications, [2]. Although nucleation and growth during implantation can be controlled to some extent by varying ion flux and substrate temperature, the control of the NPs size distribution remains a challenging task. To overcome this difficulty, new ion-based methodologies have been developed to separate the nucleation and growth and to obtain a narrower distribution of NPs either i) by combining the electronic energy deposition and the thermal annealing, [3], or ii) by having recurse to multiple implantation steps and intermediate annealing, [4]. On the other hand, application of the ion beam mixing to obtain an homogeneous NPs distribution by the dissolution of a continuous metal layer embedded in a dielectric matrix, is limited by the balling up of the metal layer due to the surface tension effect, [5, 6]. Finally, although chemical synthesis techniques have been successfully developed to produce monodisperse NPs, such methods are not fully compatibles with optoelectronic technology, [4].

Recently the formation of nanocluster halo around large precipitate was observed in samples irradiated with energetic ions, [7, 8, 9, 10, 11]. Moreover, elemental-selective dealloying with preferential extraction and precipitation of one atomic element from the original NP was shown, [9]. Finally, Kluth at al. studied the stability of the metallic nanophase under MeV ion irradiation, [12]. On the other hand, a complete and coherent theoretical description of these phenomena is still lacking. In particular, an accurate control of the fabrication processes needs the knowledge of the underlying mechanisms of the NPs evolution under irradiation. In this regard, the first condition to be satisfied is to start with a model system. That is, a system where besides the control of the irradiation parameters, i.e. ion, energy, flux, we can also have an initial control of NPs parameters, e.g. the size, the concentration and the spatial distribution. With this purpose, we developed a new procedure which combines the chemical synthesis of metallic NPs and the ion irradiation. The main advantage with respect to other methods, e.g. the ion beam synthesis (IBS), [13], where the precise control of the NPs is challenging, is that the evolution of the system can be studied by varying only one parameter at the time.

The purpose of the present work is double: on one hand, we show that the precipitates spatial distribution can be controlled by embedding chemical synthesized NPs into a silica matrix. Moreover, we show that the complete dissolution of large NPs (15-20 nm) induced by the irradiation (Au 4MeV) results in the formation of a narrow size distribution (0.4 nm) of small precipitates with a mean size of 2 nm. On the other hand, we give an insight into the basic mechanisms of NPs dissolution followed by particles nucleation and growth in its surrounding.

3.2 Experimental

The samples were irradiated at room temperature (T=300K) with 4 MeV Au^{2+} ions (see Table3.1). The nuclear energy loss (Sn=7.5 keV.nm-1) as well as the implantation depth of the Au ions (R_p ~1±0.1 μm) were estimated using SRIM2000 CODE, [14, 15]. The R_p is at least five times the depth at which NPs were synthesized (200 nm). Thus implanted Au ions do not interact with the Au NPs. The irradiation fluence range was 0-8x10^{16}cm^{-2} to ensure that quasi-steady-state conditions were reached for precipitates.

Table 3.1: Characteristics of the irradiation conditions

Ion	Energy (MeV)	Current density (μA)	Temperature (K)	Sn (keV.nm^{-1})	Ion fluence (10^{16} cm^{-2})	NP size (nm)	Satellite Size (nm)
Unirradiated	-	-	-	-	0	15.9±2.1	-
Au^{2+}	4	2	300	7.5	0.5	14.5±2.3	2.1±1.2
					0.75	12.1±2.4	2.3±1.1
					1.0	10.8±1.2	2.2±1.3
					2.0	9.2±0.8	2.9±0.9
					4.0	4.4±0.8	2.3±0.6
					6.0	2.2±0.5	2.2±0.5
					8.0	2.0±0.4	2.0±0.4

3.3 Results

Figure 3.1a) shows the plane view TEM micrograph of the as-prepared NPs. They consist of almost spherical and isolated particles. The corresponding size distribution is nearly symmetric with a centroid at 15.9 nm and a small dispersion of 2.1 nm, figure3.1(f).

The NPs evolution as function of the irradiation fluence is shown in figure 3.1(b-e). The associated size distributions are reported in figure 3.1(f-j). The irradiation promotes the formation of a halo of satellite precipitates around

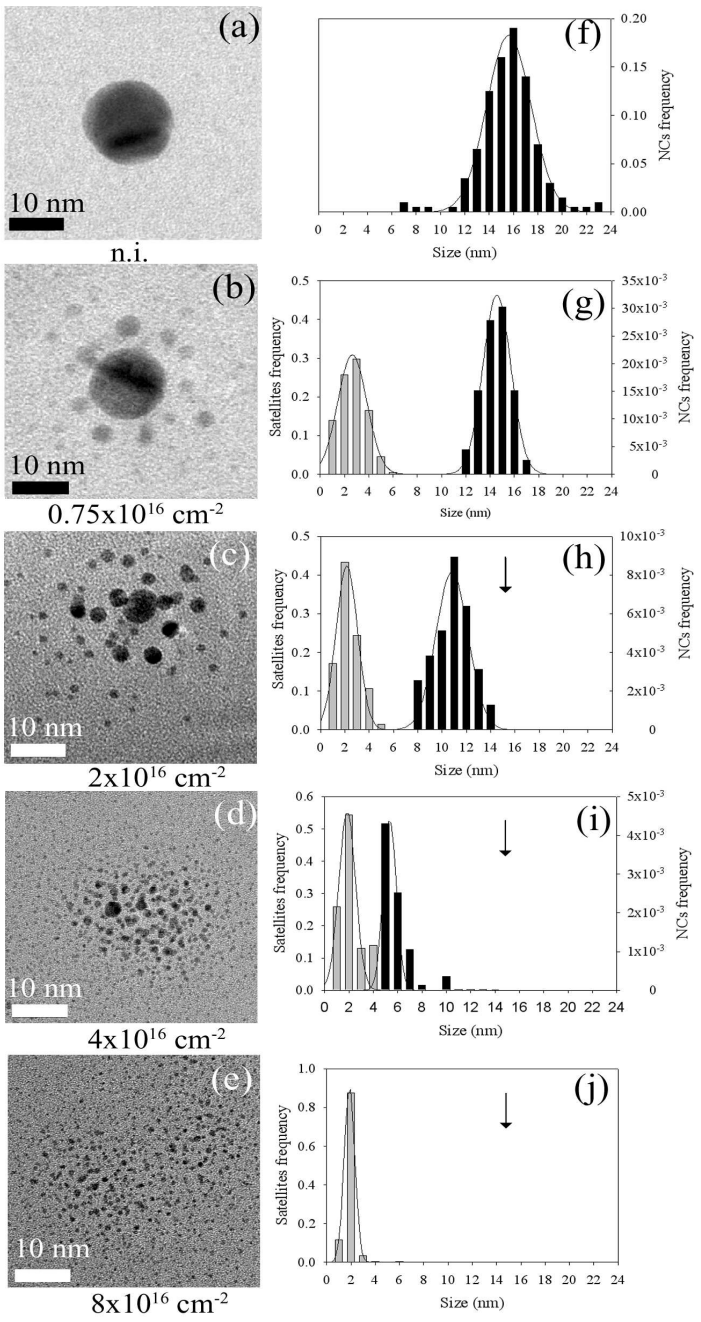

Figure 3.1: (a-e) Bright field TEM micrographs of the time sequence of NPs evolution under 4 MeV Au irradiation at 300 K. The samples were irradiated at increasing fluences up 8x10^{16}cm^{-2}. (f-j) The corresponding size distributions of NPs and satellites.

the original NP, as shown in figure 3.1(b). This corresponds to the emergence

of a new peak in the size distribution graph. To facilitate the observation, the peaks were respectively drawn in black, for the NPs, and in gray, for the satellites.

For irradiation fluences up to 0.5x10^{16} cm^{-2}, the two peaks are well separated, figure 3.1(g). The centroid of the NPs is found at 14.5±2.4 nm, whereas that of the satellites at 2.1±1.2 nm. Increasing the irradiation fluence, the continuous dissolution of the original NPs corresponds to a shift of the mean diameter towards the lower values of the cluster dimension, figure 3.1(g-j). The arrow indicates the average size of the unirradiated particles. It is worth noting that this shift does not correspond to the broadening of the size distribution, which remains limited to 2-3 nm. This means that all the original NPs were dissolved by the irradiation. On the other hand, the nucleation and growth of a first generation of satellites close to the NP surface is followed by the precipitation of new satellites at increasing distances. For irradiation fluences higher than about 4x10^{16} cm^{-2} the two size distributions merge (figure3.1(i)). In other words, the NPs size becomes equivalent to that of the satellites. This corresponds to the complete dissolution of the original NPs. Thus, from this fluence, the precipitates distribution is calculated considering the NP and the satellites as a whole. For irradiation fluences ranging from 4 to 8x10^{16} cm^{-2}, we observe the partial dissolution of the larger satellites, i.e. those closer to the NP surface. This is associated to an increase of the precipitate density (figure 3.1(d-e)). Finally, for the maximum fluence used in the present experiment, 8x10^{16} cm^{-2}, a very narrow distribution is found (figure 3.1(e)). This corresponds to a mean size of 2.0 nm and to a standard deviation of 0.4 nm. It worth stressing that this value is much lower than that of the original NPs (2.1 nm).

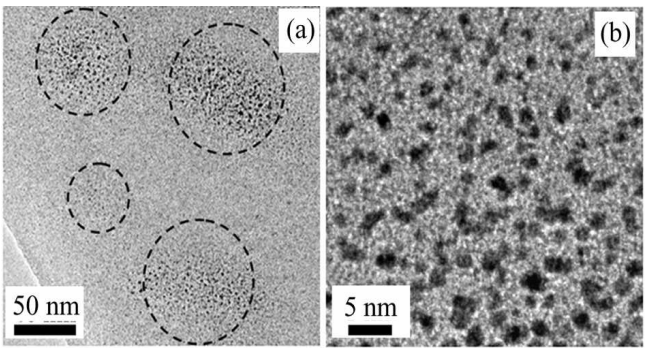

Figure 3.2: (a) Bright field TEM micrograph of four completely dissolved NPs at a fluence of 8x$10^{16}$$cm^{-2}$. (b) A detail of one of these regions, where nearly monodisperse NPs with a mean size of 2.0 nm are observed.

Figure 3.2(a) shows four completely dissolved NPs in a sample irradiated at a fluence of 8x10^{16} cm^{-2}. At the place of original NPs, a multitude of smaller precipitates was found. A higher magnification of one of these regions

(figure 3.2(b)) shows the very narrow NP size dispersion. Moreover, a simply electron diffraction analysis indicates that the fcc crystallographic structure of the NPs is not modified by the irradiation. It is worth noting that very recently, Kluth et al. [12], using a more sophisticated EXAFS spectroscopy analysis showed that irradiation induce disorder in the crystalline nanophase.

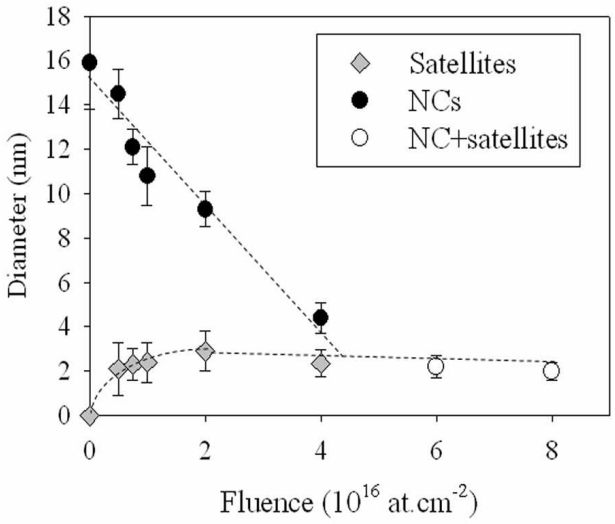

Figure 3.3: Original NPs and satellites size evolution in the fluence range of 0-8x10^{16}cm^{-2}. NPs are represented by full black circles, satellites by full gray diamond. Starting from the fluence of about 5x10^{16}cm^{-2}, the two curves intercept each other and the mean diameter is calculated considering NPs and satellites as a whole (hollow circles).

The possibility to use the irradiation to tailor an ensemble of precipitates by reducing the NPs size is even more clear if we look at figure 3.3. Here, the average diameter of both NPs and satellites is reported as a function of the irradiation fluence. On one hand, a linear correlation between the NPs dissolution and the radiation fluence is observed (black circle). On the other hand, the size of the satellites (gray diamonds) continuously grows up to a saturation value of about 2 nm which is reached at a fluence of about 2x10^{16} cm^{-2}. The dotted lines are only to help the eye to follow the particle size evolutions. The two curves intercept each other at a fluence of about 5x10^{16} cm^{-2}. Hence, the system (NPs+satellites) evolves as a whole towards a steady state condition (hollow circles).

In figure 3.3, the average diameter of the satellites is evaluated by considering all the precipitates. However, TEM micrographs indicate that the satellites size decreases with the distance from the NP surface, figure 3.4(a). In particular, the satellites close to the NP surface, which in the following will be also called the satellite of first generation, can grow up to sizes which

are systematically larger than the steady state equilibrium size. This behavior is well illustrated in figure 3.4(b). The first generation of satellites grows up to a maximum size of about 3 nm, corresponding an irradiation fluence of 2x10^{16} cm^{-2}, for then partially dissolves down to a steady state size of 2 nm for irradiation higher than 4-5x10^{16} cm^{-2}. On the other hand, the satellites far from the NP surface continuously grow towards the equilibrium size, which is reached at about 2-3x10^{12} cm^{-2}. The commencement of the satellites dissolution can be related to the dimension of the dissolving NP, where it cannot support any more the growth of the surrounding precipitates.

The modification of the growth regime corresponds to an increase of the precipitates density that passes from about ∼2x10^{12} cm^{-2} for fluences up to 2x10^{16} cm^{-2}, to about 6x10^{12} particles.cm^{-2} or fluences higher than 4x10^{16} cm^{-2} (figure 3.5).

Therefore, we can conclude that the evolution of the satellites can be seen as a two step process where the transition between the two regimes is controlled by the original NP size.

Finally, in figure 3.6 we report the maximum distance at which satellites were observed from the NP surface as a function of the irradiation fluence. This evolution can be described by a square function of the radiation dose: $D_{max} \propto \sqrt{\Phi}$.

3.4 Discussion

3.4.1 Theory

Before discussing the experimental results, we recall the basic principles of the nucleation theory. In the classical nucleation theory from a supersaturated solution, the precipitation of clusters with radii exceeding the critical radius is followed by the particles growth by draining the supersaturated solution, [16, 17]. In this regime, because of the large supersaturation, all the clusters can grow without competing effects. However, when the supersaturation degree is reduced to a very low level, the cluster evolution is then governed by its chemical potential. Here, the solute concentration around a spherical precipitate of radius R is given by the Gibbs-Thomson relation : $C(R)=C_\infty \exp(2\sigma V_a/RkT) \simeq C_\infty(1+R_C/R)$, where C_∞ is the equilibrium solute concentration at flat interface and R_C is the capillarity length. As the equilibrium concentration at the cluster surface scales as the inverse of the cluster size, the clusters evolve towards the growth of the larger ones at depends of the smaller ones. This regime is also called the Ostwald ripening (OR) regime if the total mass is conserved.

During the irradiation, a NP can be seen as a source of solute. In fact, the atoms recoil and the collision cascades cause the ballistic ejection of Au atoms from the original NP and their deposition in the surrounding matrix (SiO_2). When the solute concentration overcomes the solubility threshold,

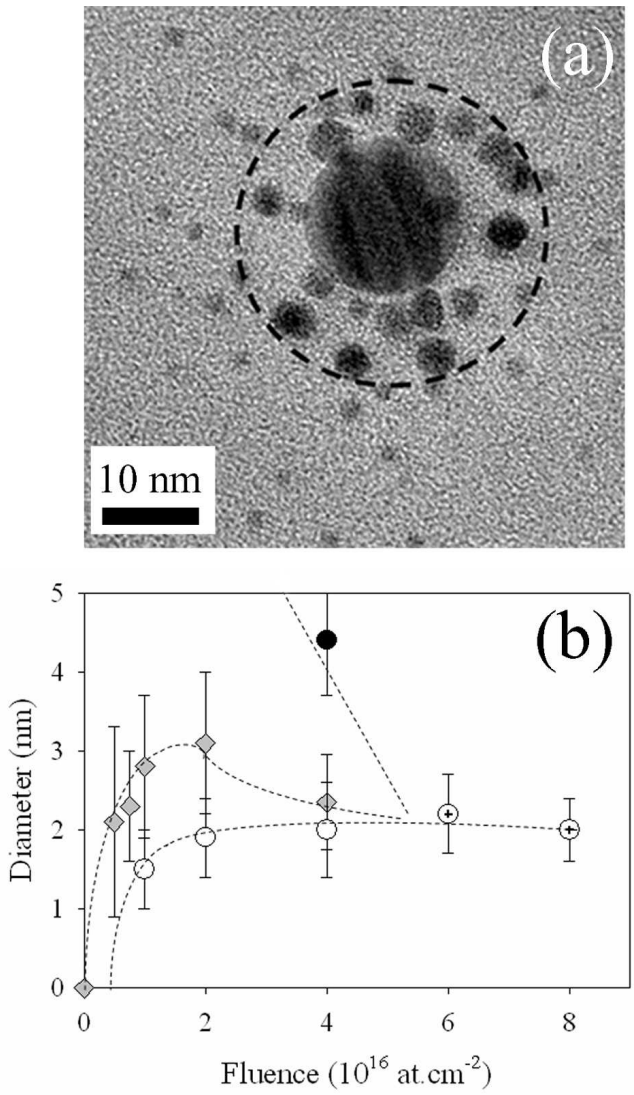

Figure 3.4: (a) Bright field TEM micrographs of a single NPs surrounded by satellites. Micrographs show the satellites size dependence on the distance from the NP surface. The dotted circle separates the larger satellites, close to the NP surface, from the smaller ones, observed far from the NP surface. (b) mean size evolution of different satellites population as well as the NPs as a function of the irradiation fluence. Original NPs are represented by full black circles, first generation of satellites by full gray diamonds and further generation of satellites by hollow circles.

the nucleation of a new phase can occur. However the irradiation also affect the NP stability. Recently an analytical treatment of the steady-state of a NP under irradiation has been proposed, [18, 19]. It has been shown that the asymptotic expression for the steady-state concentration of a NP un-

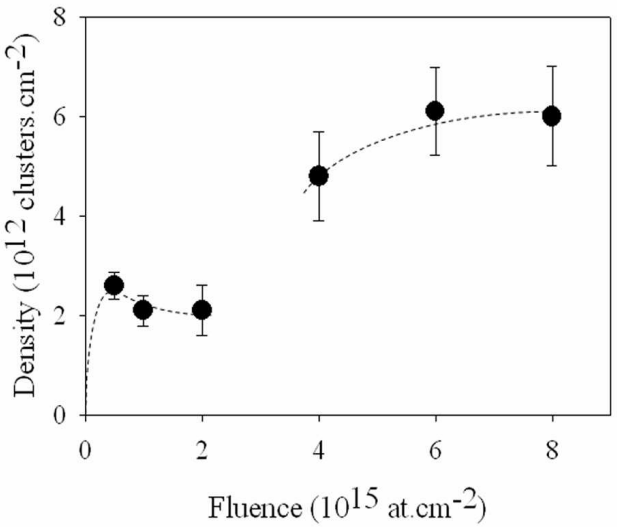

Figure 3.5: Evolution of the precipitates density as a function of the irradiation fluence.

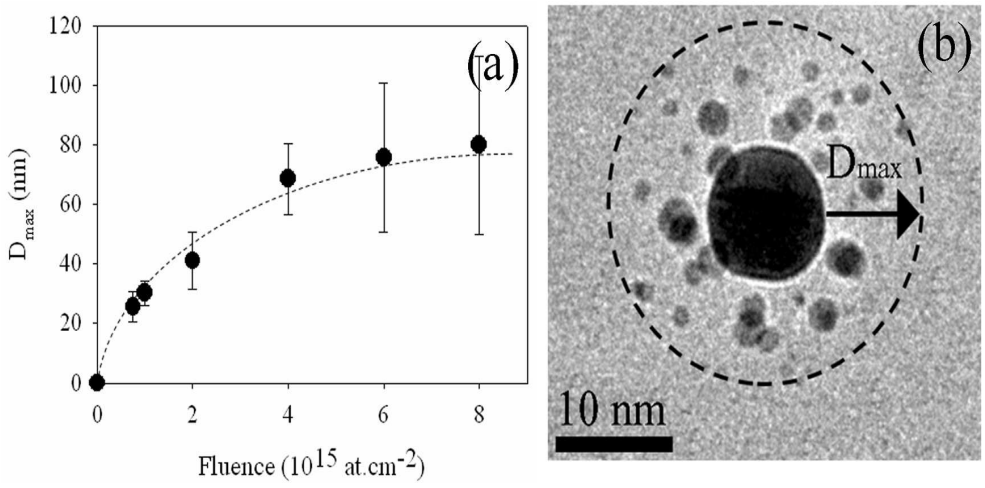

Figure 3.6: (a) Increase of maximum satellite clusters distance from the original cluster surface with dose of irradiating-ion. (b) Bright field a sample irradiated with a fluence of $1x10^{16}cm^{-2}$. Maximum satellite clusters distance is indicated by the dotted circle.

der irradiation takes an expression equivalent to that of the Gibbs-Thomson : $C^I(R)=)\simeq C^I{}_\infty(R)(1+R^I{}_C/R)$, where $C^I{}_\infty$ and $R^I{}_C$ are respectively the equilibrium solute concentration at planar surface and the capillarity length under irradiation. The model predicts that below a critical temperature the capillarity length can be negative. In other words, the surface tension of

small clusters becomes negative. This reverses the chemical potential gradient, favoring the small clusters at the expanse of the large ones. This regime was named inverse Ostwald ripening. MC simulations indicate that nucleation of new clusters, not predicted by the model, and inverse Ostwald ripening regime can be both active for low T, where the steady-state solute concentration under irradiation becomes so high that new precipitates can nucleate, [20]. Unfortunately, in literature only few and inconclusive experiments exists on the study of the inverse Ostwald ripening mechanism, [7, 21, 22].

3.4.2 A two steps mechanism

To describe the irradiation-induced NPs tailoring, the particle size can be taken as the key parameter. At the beginning of the irradiation the original NP is the only source of impurity (in the limit of non-interacting NPs).

As the concentration of gold impurities increases with the ion fluence, nucleation of embryos occurs by local fluctuations of the solute concentration, when it overcomes the solubility threshold. In addition, because the low gold diffusivity at room temperature, the precipitation is favored close to the original NP. Finally, as the displacement cascades are in first approximation isotropically distributed at the NP surface, [23], the nucleation occurs all around the original particle.

The irradiation induced NPs evolution towards a steady-state condition can be described by a two steps process. The first one is characterized by i) the beginning of NP dissolution, ii) the nucleation and growth of a first generation of satellites close to the NP surface and iii) the continuous nucleation of further generations of satellites at increasing distances from the NP surface. On the contrary, the second step is characterized by i) the complete dissolution of the original NP, ii) the partial dissolution of the first generation of satellites, iii) the evolution of the system toward a nearly monodisperse size distribution and iv) the increase of the cluster density.

In the first regime, the original NP acts as an infinite source of solute allowing to keep a high supersaturation level in its surrounding. Therefore, the growth of the first generation of satellites is sustained by the dissolution of the original NP. Moreover, the nucleation of further generation of satellites is favored either by the Radiation Enhanced Diffusion (RED) of the solute monomers ejected from the original NP and/or by the continuous dissolution of the existing satellites, which act as secondary solute sources. It worth noting that under irradiation the Au diffusivity is not zero as indicated by the fact that nucleation was observed in ion-implantation experiment performed at room temperature, [24, 25, 26, 7]. In this first regime, both the growth of all the particles and the nucleation of new clusters is observed. This implies that the supersaturation level is high. Thus, we can exclude that we are in presence of a classical Ostwald ripening mechanism. On the other hand,

in the fluence range of 0.5-2x10^{16} cm^{-2}, the density of satellites is almost constant. This, associated with the observed clusters nucleation, indicates that some kind of ripening is active. It has been shown that when mass conservation is violated, i.e. when the external flux of matter impinging on the matrix is sufficiently large, coalescence is the dominant growth mechanisms, [27]. As, in first approximation, ion irradiation can be seen as a local ion implantation, where mass is displaced at increasing distances from the original NP. Locally, mass is not conserved. In this regards, it is plausible that coalescence occurs among touching satellites. Hence, in the first regime the growth of the satellites is governed by the supersaturation level. This means that growth mechanisms is not controlled by an inverse OR mechanism. This has a consequence: it is impossible to observe an inverse OR mechanism if the precipitates are formed from an infinity solute source, as for example a semi-infinity flat surface. However, the growth process will be limited by the ion mixing effects.

Once the size of the original NP becomes comparable to that of the surrounding satellites, the partial dissolution of part of the satellites, accompanied with an increasing of the nucleation frequency, is observed. As the size of the original NP is reduced below a critical value, the NP looses its capability to sustain the growth of the surrounding particles. This fact determines the beginning of the second regime. Of course, the transition from one regime to another one is a statistical process and does not occur at a precise irradiation fluence, but it is more a continuous process. From previous experimental analysis, and for our experimental conditions, we can estimate that this transition starts at about at 3-4x10^{16} cm^{-2}.

The second regime corresponds to the evolution of the whole system towards a steady state condition. The partial dissolution of part of the satellites implies that the supersaturation level has fallen to a very low level. Thus, the precipitates evolution is now governed by the interface effects. In the classical Ostwald ripening, the system evolves towards the growth of the large particles and the dissolution of the small ones. Again, we can exclude that the dominant mechanisms for particles evolution under irradiation is the classical OR mechanisms. Here, the system evolves towards a steady state configuration where each precipitate becomes an equivalent solute source and where the equilibrium size is given by the steady-state balance between the interface mixing, which favors the particle dissolution, and the draining of the solute atoms, which favors the particle growth. This second regime can be interpreted in the light of the inverse OR mechanisms.

3.4.3 Radiation Enhanced Diffusion

In figure 3.6 we show that the maximum distance at which satellites are found varies as the square of the irradiation fluence ($\sqrt{\Phi}$). It is known that irradiation can favors the diffusion of the dissolved atoms by increasing the

amount of structural defects in silica matrix, [28]. The Radiation Enhanced Diffusion (RED) can be correlated to the fraction of kinetic energy of energetic ions dissipated through electronic excitation processes. In particular Frenkel defects formation of oxygen vacancies and interstitial ions induced by the electronic excitation, [29]. It has been speculated that interstitial metal atoms tend to form complexes with vacancies because of their large size and that the complexes are more mobile than the simple defects. Thus, the RED is likely due to the formation of vacancy-impurity complexes which are mobile at low T in the silica network, [30].

This process can be qualitatively understood by taking into account the expression for the diffusion coefficient D=x^2/4t, and replacing the diffusion distance x with the maximum distance at which satellites were found (D_{max}) and the time t with the ion fluence ϕ=φt, where and φ is the constant ion flux. This gives:

$$D_{max} \propto \sqrt{4D_{RED}\phi/\varphi} \tag{3.1}$$

This expression correlates the maximum distance at which satellites were found, D_{max}, to the diffusion coefficient under irradiation, D_{RED}.

3.5 Conclusion

In summary, using Au colloids embedded in a silica matrix as a model system, we demonstrate the possibility to tailor an ensemble of precipitates by reducing the NP size and to obtain a nearly monodisperse NPs distribution. This approach will be useful when the reduction of the mean size of embedded NPs is desired. We show that the size reduction is accompanied by the narrowing of the size distribution. Indeed, by this method, we obtain a standard deviation of 0.4 nm on an average diameter of 2.0 nm, compared a standard deviation of 2.1 nm for the initial NPs. It is worth noting that combining the chemical synthesis of the NPs and the ion irradiation to tune the particle size, we overcome the problems related to the control of size and spatial distribution associated with the synthesis of NPs using ion implantation.

Moreover, we reveal the existence of two regimes for satellites evolution. The first one is governed by the supersturation level maintained by the NPs dissolution, whereas the second, which is characterized by the evolution of the whole system towards a steady state condition, is dominated by the steady-state balance between the interface mixing, which favors the particle dissolution, and the draining of the solute atoms, which favors the particle growth, where each particle can be considered an equiprobable solute source.

Finally, further experiments are scheduled to elucidate the role of the irradiation parameters (ion energy, current density), as well the temperature and the NPs size on the dissolution process.

Bibliography

[1] In: F. Gonella and P. Mazzoldi, Editors, Handbook of Nanostructured Materials and Nanotechnology Vol. 4, Academic Press, San Diego (2000).

[2] A. Meldrum, L.A. Boatner and C.W. White, Nucl. Instr. and Meth. B **178**, 7 (2001)

[3] E. Valentin, H. Bernas, C. Ricolleau, F. Creuzet, Phys. Rev. Lett. **86**, 99 (2001).

[4] V. Ramaswamy, T.E. Hayens, C.W. White, W.J. Moberly Chan, S. Roorda, M. Aziz, Nanoletters **5**, 373 (2005)

[5] G. Rizza, F. Garrido, J.C. Pivin, J.C. Dran, L. Thome, M. Gusso, L. Tapfer, A. Quaranta, P. Colombo, Nucl. Instr. Methods B **127**, 574 (1997)

[6] L. Thome, G. Rizza, F. Garrido, M. Gusso, L. Tapfer, A. Quaranta, Applied Physics A **67**, 241 (1998)

[7] G.C. Rizza, M. Strobel, K.H.Heinig, H.Bernas, Nucl. Instr. Meth. B **178**, 78 (2001)

[8] G. Mattei, G. De Marchi, C. Maurizio, P. Mazzoldi, C. Sada, V. Bello, G. Battaglin, Phys. Rev. Lett. **90**, 855502 (2003)

[9] G. Mattei, G. Battaglin, V. Bello, G. De Marchi, C. Maurizio, P. Mazzoldi, M. Parolin, C. Sada, J. Non-Cryst. Solids **322**, 17 (2003)

[10] V. Bello, G. De Marchi, C. Maurizio, G. Mattei, P. Mazzoldi, M. Parolin, C. Sada, J. Non-Cryst. Solids **345-346**, 685 (2004)

[11] G. Mattei, V. Bello, P. Mazzoldi, G. Pellegrini, C. Sada, C. Maurizio, G. Battaglin, Nucl. Instr. Meth. B **240**, 128 (2005)

[12] P. Kluth, B. Johannessen, G.J. Foran, D.J. Cookson, S.M. Kluth, M.C. Ridgway, Phys. Rev. B **74**, 14202 (2006)

[13] P. Mazzoldi, G. Mattei, Rivista de Nuovo Cimento **28**, 1 (2005)

[14] J.F. Ziegler, J.P. Biersack, and U. Littmark, The Stopping Ranges and Ranges of Ions in Solids Pergamon Press, New York, 1985

[15] http://www.srim.org

[16] C.H. Herring, In: Structural and properties of thin Surfaces, R. Gomer and C.S. Smith Eds. Chicago Press (1953)

[17] I.M. Lifshitz, V.V. Slyozov: J. Phys. Chem. Solids **19**, 35 (1961)

[18] M. Strobel, K.H. Heinig, W. Möller, Phys. Rev. B **64**, 245422 (2001)

[19] K.H. Heinig, T. Müller, M. Strobel, B. Schmidt, W. Möller, Appl. Phys. A **77**, 17 (2003)

[20] M. Strobel, K.H. Heinig, W. Möller, Mater. Res. Soc. Symp. Proc. **647**, 23 (2001)

[21] B. Schmidt, K.H. Heinig, A. Muecklich: Mater. Res. Soc. Symp. Proc. **647**, O11.20 (2001)

[22] P. Kluth, M.C. Ridgway, Nucl. Instr. Meth. B **242**, 458 (2006)

[23] P. Sigmund: In: Sputtering by Particle Bombardment I, ed. by R. Behrisch (Springer, Berlin 1981)

[24] M. Strobel, K.H. Heining, W.Möller, A. Meldrum, D.S. Zhou, C.W. White, R.A. Zuhr, Nucl. Instr. Meth. B **147**, 343 (1999)

[25] D. Ila, E.K. Williams, S. Sarkisov, C.C. Smith, D.B. Poker, D.K. Hensley, Nucl. Instr. Meth. B **141**, 289 (1998)

[26] D. Ila, E.K. Williams, R.L. Zimmerman, D.B. Poker, D.K. Hensley, Nucl. Instr. Meth. B **166-167**, 845 (2000)

[27] G.R. Carlow, Physica A **239**, 65 (1997)

[28] M. Nastasi, J.W. Mayer, J.K. Hirvonen (Eds.), Ion-solids interactions fundamentals and applications, Cambridge University Press, Cambridge, UK, 1996.

[29] H. Hosono, N. Matsunami, Nucl. Instr. Meth. B **141**, 566 (1998)

[30] J.C. Pivin, G. Rizza, F. Garrido, L. Thomé, Europhys. Lett. **39**, 623 (1997) .

Chapter 4

Controlling the size distribution of embedded Au nanoparticles using ion irradiation

Abstract

Few works exist on the ion-engineering processes, where the energy released by the energetic ions is used to modify already formed NPs. This allows, for example, the morphology of the NPs to be shaped, e.g. [1, 2, 3, 4], or the nucleation and growth of elements already present within the matrix to be promoted, e.g. [5, 6, 7, 8]. The latter results in the formation of a halo of satellites around the pristine NP. Following this approach, in the previous chapter, we succeeded in displacing the initial size distribution of the NPs toward a smaller steady-state size, narrowing, at the same time, its size dispersion, [6]. The aim of this chapter is to extend our investigation on the ion-engineering of confined NPs by studying their evolution when the temperature and the deposited energy are changed.

4.1 Introduction

Samples composted of chemically synthesized Au nanoparticles(NPs) (16.0±2.0nm) embedded within a planar silica film are used as model system to investigate the evolution of a second phase under irradiation when the temperature and the ion stopping power are changed. Samples are irradiated with 4MeV Au^{2+} ions and 4MeV Br^{2+} ions for temperature ranging from 30°C up to 800°C and for fluences up to 8x10^{16} cm^{-2}. We show that at room temperature the complete dissolution of the NPs leads to the formation of smaller precipitates with a narrower size distribution, i.e. 2.0±0.3nm. However, when the temperature is increased and/or the nuclear stopping power is decreased, a reduction of the dissolution rate was observed. This leads to the formation of a bimodal size distribution. Finally, the evolution of the density of the precipitates with the temperature is discussed in term of the thermal stability of the irradiation-induced defects within the silica matrix.

4.2 Experimental

Samples were irradiated with Au^{2+} and Br^{2+} ions in the fluence range of 0-8x10^{16} cm^{-2} under a constant ion flux of 1 μA.cm^{-2}. The nuclear and the electronic stopping power for both Au and Br ions in both Au NPs and SiO_2 matrix were calculated with the code SRIM 2008, [9]. The values are reported in Table 4.1.

Table 4.1: Characteristics of the irradiation conditions. S_n is the nuclear stopping power and S_e the electronic stopping power as estimated from the code SRIM 2008, [9], for both Au NPs and SiO_2 matrix.

Ion	Energy (MeV)	S_n^{Au} (keV/nm)	S_e^{Au} (keV/nm)	$S_n^{SiO_2}$ (keV/nm)	$S_e^{SiO_2}$ (keV/nm)
Au^{2+}	4	7.5	3.6	2.0	2.2
Br^{2+}	4	1.2	3.3	3.2	1.9

The irradiation temperature was varied between 30°C and 800°C. The latter value was chosen to be lower than the melting temperature of the NPs. This is generally lower than that of the bulk material (T_{melt}(Au)=1064°C) and depends on the NP size. For 16 nm gold NPs evaporated at low pressure on an amorphous carbon film, Buffat and al. estimate that the melting temperature is about 960°C, [10]. The same value was measured by Dick and al. for 16 nm gold NPs encapsuled in silica, [11]. This indicates that the matrix plays only a minor role on the melting temperature of the nanoparticles.

4.3 Results

In this section, we first analyze how the size distribution is modified when the irradiation temperature is changed. We then investigate how the size of the NPs evolves with fluence when different irradiation temperatures are considered. Finally, we investigate how the NPs evolve when the stopping power is varied.

4.3.1 Size evolution with temperature at a given fluence

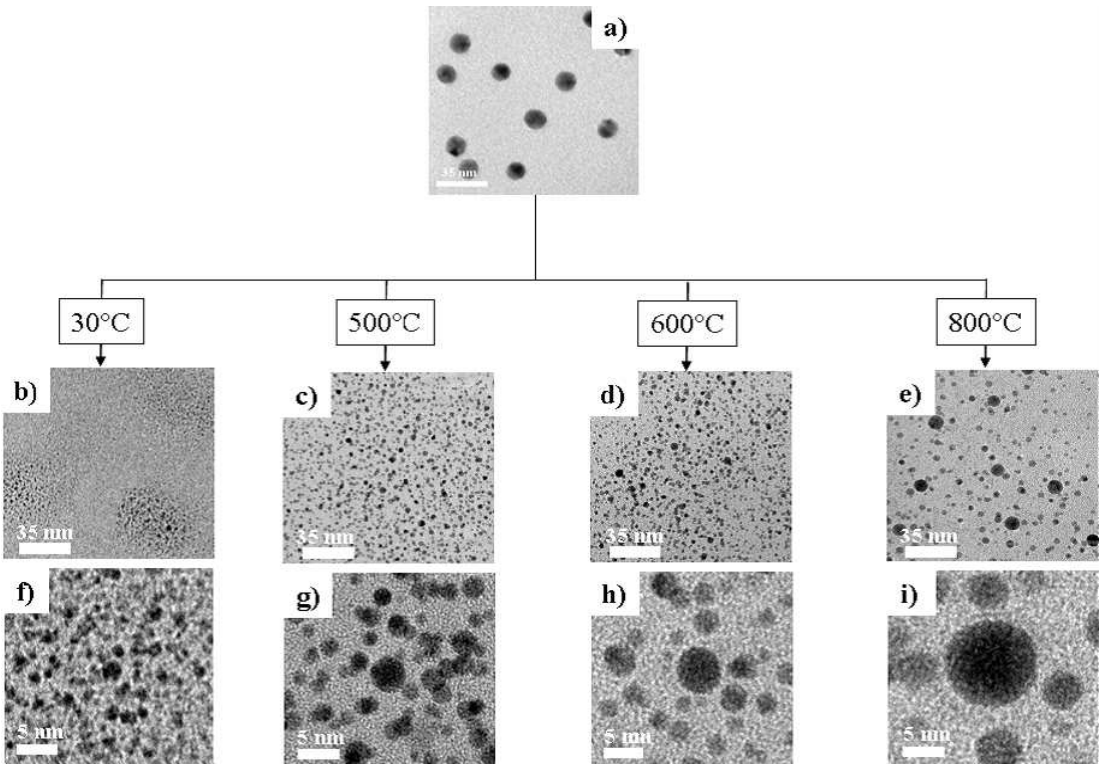

Figure 4.1: a) Bright field TEM micrograph of an as-prepared sample. Bright field TEM micrographs of samples irradiated with 4MeV Au ions at a fluence of $8x10^{16}$ cm^{-2} for increasing temperatures: b) and f) 30°C, c) and g) 500°C, d) and h) 600°C, e) and i) 800°C. Magnification of the previous micrographs are also shown: f) 30°C, g) 500°C, h) 600°C, i) 800°C The ion irradiation is normal to the plane.

Figures 4.1(b-i) show the Au NPs (D_0=16 nm) irradiated with 4MeV Au^{2+} ions at the fluence of $8x10^{16}$ cm^{-2} for increasing temperatures, i.e. from 30°C to 800°C. The corresponding normalized size distribution functions are shown in figure 4.2(b-e).

Irradiation at room temperature (30°C) favors the complete dissolution of the pristine NPs and the nucleation and growth of smaller, nearly mono-

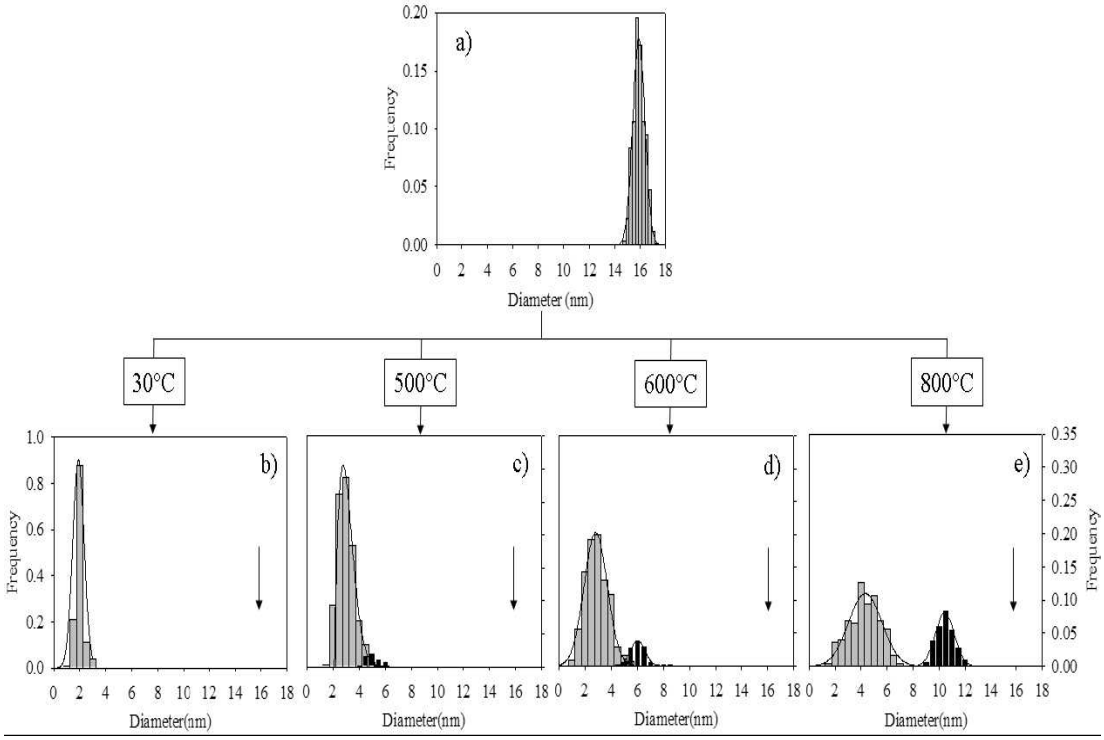

Figure 4.2: a) Size distribution corresponding to the pristine Au NPs. b-e) Size distributions for the samples irradiated with 4MeV Au ions at a fluence of $8x10^{16}$ cm^{-2}: b) 30°C, c) 500°C, d) 600°C, e) 800°C. The distributions corresponding to NPs are in black, those relative to precipitates in gray. The arrows indicate the initial size of the NPs.

disperse, precipitates, figure 4.1(b). These remain spatially localized in the vicinity of the original NP, i.e. the diffusivity of the metallic species is low. Figure 4.1(f) represents a magnification of the central part of figure 4.1(b). The mean size and size dispersion of the precipitates (2.0±0.3 nm) are obtained considering the corresponding symmetric (gaussian) size distribution function, figure 4.2(b). Here, the arrow indicates the size of the pristine Au NPs. These results can be compared to those obtained for Au NPs confined within a silica film prepared by sol-gel technique, (2.0±0.4 nm), [6]. As the steady-state size is nearly the same for the two configurations, we conclude that the matrix has only a minor influence on the evolution of the precipitate phase.

Irradiation at 500°C results in a random distribution of the precipitates within the matrix, figure 4.1(c). Thus, when the irradiation temperature is increased, the spatial localization of the precipitates is lost. That is, above a threshold temperature the diffusivity of the metallic species within the silica matrix becomes important. Here, the satellites present a broader size

dispersion, between 2 and 5-6 nm, compared to those obtained at room temperature (1-3nm), figure 4.1(g). This effect is better appreciated on figure 4.2(c), where the size distribution function is slightly shifted toward the larger sizes and presents a tail in the same direction. The mean size of the precipitates and the corresponding size dispersion (2.9±0.7 nm) are larger than those measured at room temperature (2.0±0.3 nm).

At at 600°C we observe the emergence of two populations of NPs, figure 4.1(d) and figure 4.1(h). Although, the majority of them have a size smaller than about 3-4 nm, some larger NPs are also observed. This effect is even more clear looking at the corresponding size distribution function, figure 4.2(d). The tail observed at 500°C is now separated from the main peak, i.e. the distribution function is now bimodal. Thus, we decide to study separately the two populations. The first peak, associated to the smaller satellites, is roughly symmetric and have a centroid at 2.7 nm and a size dispersion of 0.8 nm. The second peak corresponds to the pristine NPs which has not been completely dissolved yet. The mean size and size dispersion for this second peak are 5.8 and 0.6 nm, respectively.

At 800°C the size difference between the two population of NPs is now clearly visible, figure 4.1(e) and figure 4.1(i) and the two distribution functions are well apart from each other, figure 4.2(e). The distribution function associated with the precipitates has a mean size of 4.0 nm and the size dispersion of 1.2 nm, respectively. On the other hand, the distribution function associated with the NPs has a centroid and a size dispersion of 10.5 nm and 1.4 nm, respectively.

4.3.2 Size evolution with fluence for different temperatures

Sofar, we focussed on a single fluence and we analyze how the size distribution function changes when the temperature is increased. Here, we investigate the evolution of the NPs with fluence for different irradiation temperatures (30°C, 600°C and 800°C). Each point on the curves of figures 4.3(a-c) corresponds to the centroid of the size distribution function as obtained from TEM micrographs. For example, the points corresponding to the largest fluence ($8x10^{16}$ cm^{-2}) are obtained from the size distribution function of figures 4.2(a-e). Here, triangles represent the pristine NPs and circles the precipitates.

Figure 4.3(a) shows the evolution of both these populations for the irradiation at 30°C. Here, the system evolves toward a unique steady-state size of about 2nm. This value is reached for fluences larger than about $6x10^{16}$ cm^{-2}. During the irradiation two processes take place: i) the dissolution of the pristine NP and ii) the growth of the precipitates, [8]. *However, the steady-state size for the whole system is determined by the equilibrium size of the precipitates.* This can be easily checked observing that the average size of the precipitates reaches a plateau value for fluences larger than $2x10^{16}$ cm^{-2}.

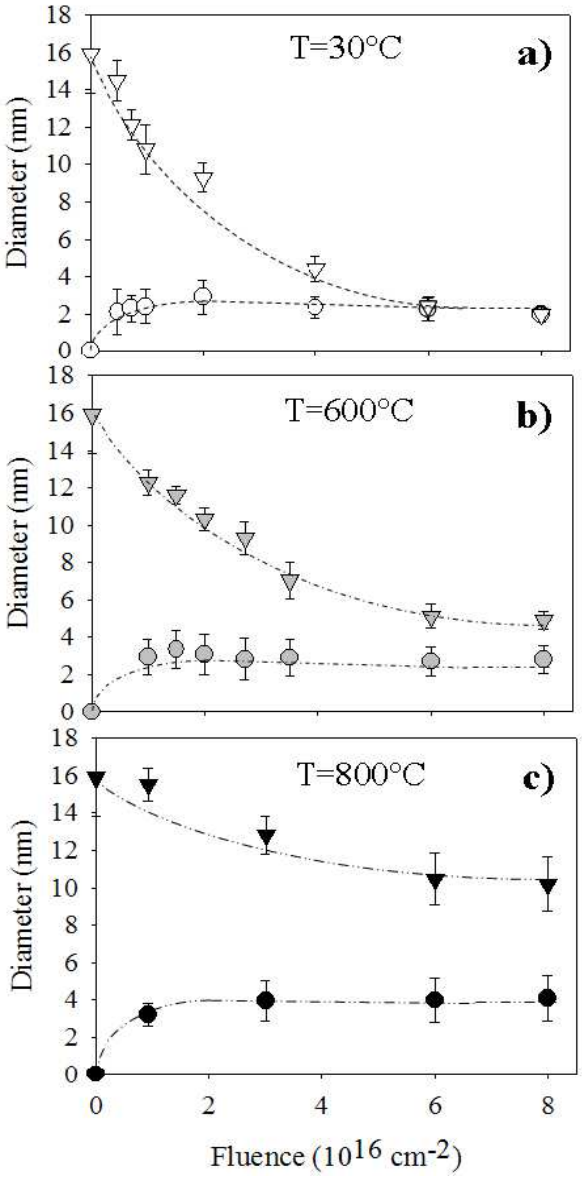

Figure 4.3: Evolution of the size of the NPs (triangles) and precipitates (circles) with fluence for different irradiation temperatures: a) 30°C, b) 600°C, c) 800°C. The samples are irradiated with 4MeV Au ions.

It worth mentioning that this fluence is lower than the fluence corresponding to the steady-state size for the whole system, e.g. 6x10^{16} cm^{-2}.

When the irradiation temperature is increased up to 600°C, the dissolution rate of the NPs is reduced, figure 4.3(b). This means that the system takes longer time to reach a steady-state condition. The consequence is that

at the maximum fluence investigated in this work (8x10^{16} cm^{-2}) the two curves are still slightly separated to each other. This explains the bimodal size distribution observed in figure 4.2(d).

At 800°C the reduction of the dissolution rate is even more evident. Here, the two populations, NPs and precipitates, remain clearly separated up to 8x10^{16} cm^{-2}.

Finally, the average size for the precipitates increases with the irradiation temperature.

4.3.3 Size evolution with energy deposition at two different temperatures

In this section we investigate how the size distribution of the embedded NPs is modified when the energy deposition is changed. The samples are irradiated with 4MeV Au^{2+} and 4MeV Br^{2+} ions up to a fluence of 8x10^{16} cm^{-2} and at two different temperatures, 600°C and 800°C. The ion mass and the ion energy are chosen such that the nuclear stopping power into the Au NP will be rather different for the two ions ($S_n{}^{Au}/S_n{}^{Br}\sim6.3$), whereas the electronic stopping power into the SiO_2 matrix will remain almost the same ($S_e{}^{Au}/S_e{}^{Br}\sim1.2$). Thus, in this sub-section we investigate how the nuclear stopping power modifies the evolution of the NPs when the irradiation temperature is changed.

Figures 4.4(a-d) show the TEM micrographs and the corresponding size distributions for the samples irradiated at 600°C at 8x10^{16} cm^{-2}. As already seen, the size distribution corresponding to the irradiation with 4MeV Au ions is monodisperse with a tail toward larger sizes, figure 4.4(c). On the other hand, the formation of a well separated bimodal size distribution is clearly observed for the irradiation with 4MeV Br ions (figure 4.4(d)). This corresponds on figure 4.4(e) to a strong decrease of the dissolution rate. Here, full triangles and circles correspond to the irradiation with 4MeV Br ions, whereas open triangles and circles correspond to the irradiation with 4MeV Au ions. As the temperature is identical for the two systems, this effect is related to the reduced nuclear stopping power for the irradiation with 4MeV Br ions.

Figures 4.5(a-d) show the TEM micrographs and the corresponding size distributions for the samples irradiated at 800°C at 8x10^{16} cm^{-2}. The first observation is that both distributions are bimodal, figures 4.5(c-d). Moreover, in comparison to the irradiation at 600°C, in both cases there is a reduction of the dissolution rate of the NPs, figure 4.5(e). However, this effect is much more pronounced for the irradiation with 4MeV Au ions, where the size of the NPs passes from about 5nm to 10nm. On the other hand, the dissolution rate is almost negligible for the irradiation with 4MeV Br ions, e.g. the NP size passes from 13nm to 15nm. Finally, the evolution of the precipitates is slower for the irradiation with 4MeV Br ions than for

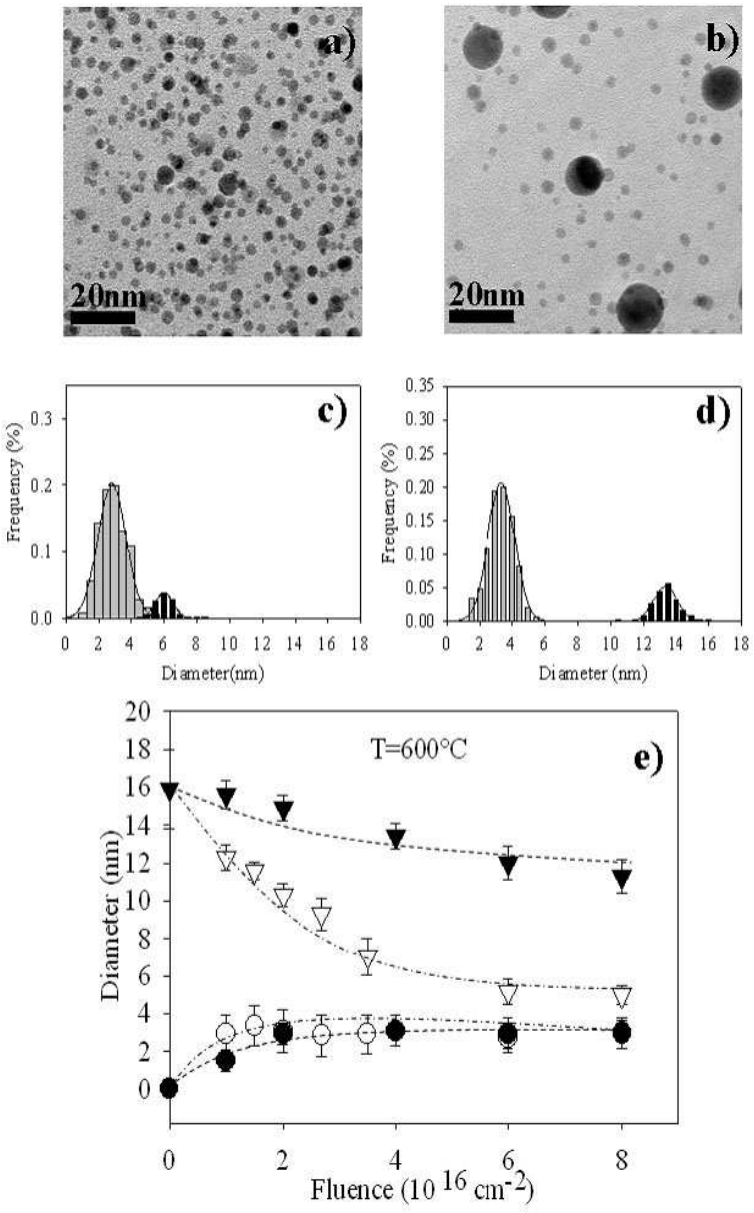

Figure 4.4: (a-b) Bright field TEM micrographs of samples irradiated at 600°C at a fluence of 8x10^{16} cm^{-2} with 4MeV Au ions (a) and 4MeV Br ions (b), respectively. c-d) The corresponding size distributions for the NPs (black) and the precipitates (gray). (e) Evolution of the size of the NPs (triangles) and precipitates (circles) with fluence. Full symbols represent the irradiation with 4MeV Br ions, whereas open symbols the irradiation with 4MeV Au ions.

the irradiation with 4MeV Au ions. In particular, in the former case the steady-state size is not still reached at the fluence of 8x10^{16} cm^{-2}.

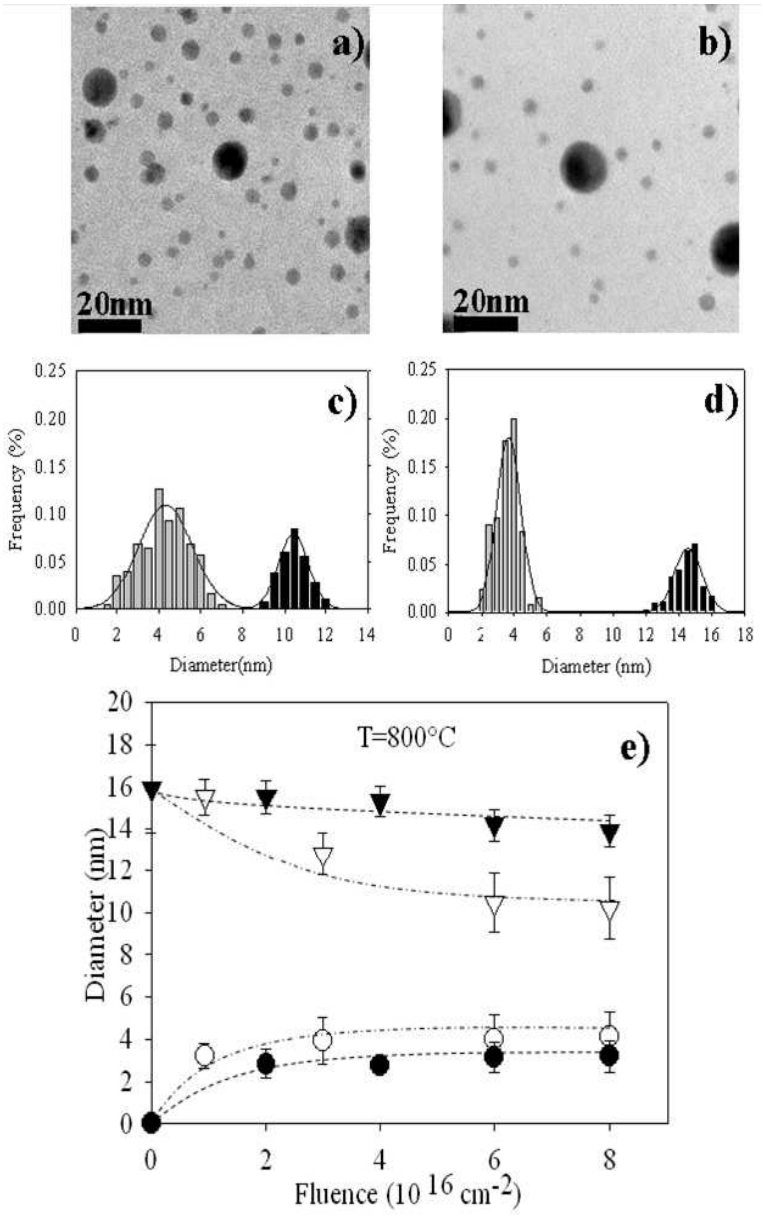

Figure 4.5: (a-b) Bright field TEM micrographs of samples irradiated at 800°C at a fluence of 8x10^{16} cm^{-2} with 4MeV Au ions (a) and 4MeV Br ions (b), respectively. c-d) The corresponding size distributions for the NPs (black) and the precipitates (gray). (e) Evolution of the size of the NPs (triangles) and precipitates (circles) with fluence. Full symbols represent the irradiation with 4MeV Br ions, whereas open symbols the irradiation with 4MeV Au ions.

4.4 Discussion

Figures 4.6(a-d) summarize the evolution of both the NPs and the precipitates when the irradiation conditions are changed. The aim of such schemes

is to rationalize the choice of the irradiation conditions to enhance the control of the final distribution of the NPs.

Figure 4.6(a) shows how the diameter of the pristine NPs is changed when the irradiation temperature is changed. For the irradiation with 4MeV Au ions (full circles) the final diameter increases from 2 nm at room temperature to about 10 nm for the irradiation at 800°C. This corresponds to a difference in size of a factor of 5. The increasing of the *final* NP diameter is due to the reduction of the dissolution rate, which in turn is directly related to the irradiation temperature. However, the increasing of the NP size with the temperature is not linear and it becomes more pronounced for temperatures larger than 500°C. For the irradiation with 4MeV Br ions (open circles), the same behavior is observed. However, here the *final* size for the NPs is systematically larger than that obtained for the irradiation with 4MeV Au ions, i.e. the dissolution rate is reduced. This is due to the difference in the nuclear stopping power between the two systems, e.g. ${S_n}^{Au}/{S_n}^{Br}\sim 6.3$.

Figure 4.6(b) shows how the size of the precipitates is changed when the irradiation temperature is changed. The steady-state size of the precipitates formed during the irradiation with 4MeV Au ions grows up from 2 nm at 30°C up to about 4 nm at 800°C. On the other hand, for the irradiation with 4MeV Br ions, the size of the precipitates remains roughly constant for temperatures ranging between 500-800°C.

Figure 4.6(c) shows how the size dispersion, σ, of both the NPs and the precipitates is changed when the temperature and the stopping power are changed. These values are normalized to the initial size dispersion, i.e. σ_0=2.1 nm. For irradiation with 4MeV Au ions the ratio σ/σ_0 increases with temperature in the same way for both NPs (full circles) and precipitates (open circles). Furthermore, this value remains well below 1. This means that in this case the irradiation favors the reduction of the size dispersion of the embedded second phase. The situation is different for the irradiation with 4MeV Br ions. On one hand, the size dispersion of the NPs strongly increases when the temperature is increased (full squares). In particular, at 800°C this value approaches 1, e.g. the initial size dispersion. On the other hand, for the precipitates the size dispersion is slightly reduced when the temperature is increased (open squares).

When the temperature is raised, the system evolves toward a bimodal size distribution. We define the difference between the size of the NPs and that of the precipitates the *size gap*. Figure 4.6(d) shows how the size gap is changed when the irradiation temperature is changed. For the irradiation with 4MeV Au ions at room temperature the system evolves toward a unique steady-state size, e.g. the gap is zero. Increasing the temperature the size gap increases up to 6 nm for the irradiation at 800°C. For the irradiation with 4MeV Br ions, the size gap is systematically larger than for the irradiation with 4MeV Au ions and ranges between 8-10nm for temperatures ranging between 500-800°C.

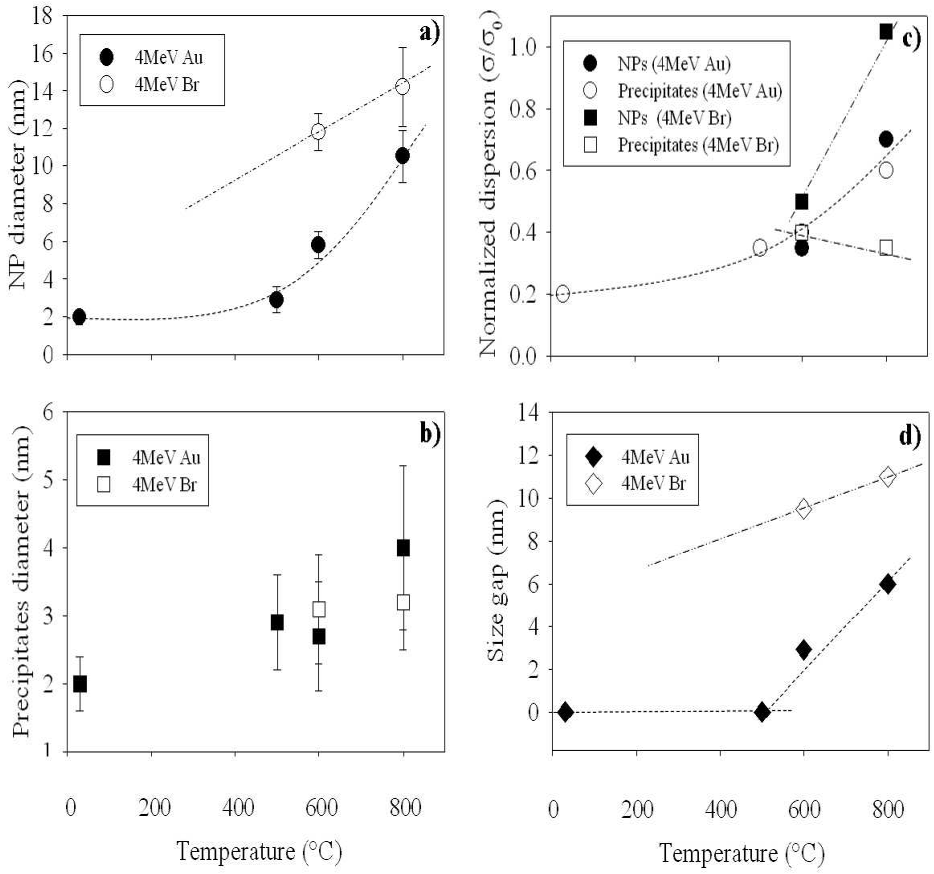

Figure 4.6: a) Evolution of the NP diameter with temperature for the irradiation with 4MeV Au ions (full circles) and 4MeV Br ions (open circles). b) Evolution of the precipitates diameter with temperature for the irradiation with 4MeV Au ions (full squares) and 4MeV Br ions (open squares). c) Evolution the normalize size dispersion for both NPs and precipitates irradiated with 4MeV Au ions (full and open circles) and 4MeV Br ions (full and open squares). d) Evolution of the size gap with temperature for the irradiation with 4MeV Au ions (full diamonds) and 4MeV Br ions (open diamonds).

4.4.1 Contribution of thermal effect on the evolution of the NPs

For a reliable interpretation of our experimental data, the effective contribution of the temperature on the evolution of the NPs under irradiation is checked. This is done by annealing the samples under the same experimental conditions as used for the irradiation experiments. Here, the three key parameters are i) the maximum annealing temperature, ii) the annealing time and iii) the annealing atmosphere.

i) to account for possible irradiation-induced heating of the sample, the

annealing temperature was chosen to be larger than the irradiation temperature, i.e. 800°C, but lower than the melting temperature for NPs, i.e. 960°C. Thus, the annealing temperature was chosen to be 900°C.

ii) the irradiation time corresponding to the largest irradiation fluence is about 12h. Thus, this time was chosen for the annealing experiments.

iii) to simulate the irradiation atmosphere, the samples were annealed under vacuum atmosphere.

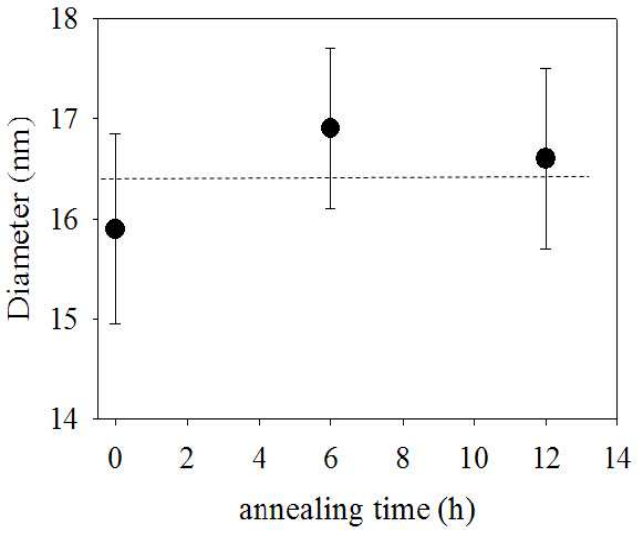

Figure 4.7: Evolution of the NP size during the annealing treatment at 900°C up to 12h under vacuum atmosphere.

To summarize, 16 nm Au NPs have been annealed at 900°C up to 12h under vacuum atmosphere. The results are shown in figure 4.7 and clearly indicate that the system is stable under annealing treatment. This results can be easily understood by considering the gold diffusivity, D_{th}, within silica at 900°C. However, it worth noticing that D_{th} is strongly affected by the annealing conditions, and that it is lower in vacuum than in air or inert atmosphere, [12, 13, 14]. For example, in "air" this value has been estimated by De Marchi and al to be of the order of $D_{th} \sim 5x10^{-17} cm^2.s^{-1}$, [13]. As $D_{th}^{vacuum} < D_{th}^{air}$, the diffusion length of the metallic solute, corresponding to an annealing time of 12h, will be at maximum of about 10 nm. This length is smaller than the mean inter-particle distance, i.e. about 35 nm.

Thus, in these experiments, the gold diffusivity is sufficient low and the density of the NPs is sufficiently small to avoid any coarsening (Ostwald ripening) process during the annealing treatment [15, 16]. Hence, our results cannot be explained by simply considering the effect of the temperature.

4.4.2 Contribution of the stopping power on the evolution on the NPs under irradiation

Under 4 MeV ion irradiation, the ion energy is deposited into the Au NP and the silica subsystems through both nuclear and electronic stopping power.

The nuclear stopping power (S_n) is roughly temperature-independent and allows primarily the gold atoms to be displaced from the NPs into the silica matrix. Without thermal effects, NPs act as purely ballistic source of solute and the precipitates are formed close to the pristine NP. The basic idea of our approach is that the physics underlying the precipitation and growth of a second phase during ion implantation is equivalent to those that intervene during the satellites nucleation and growth. Here high solute concentration is deposited in small volumes around the NP, via the irradiation-induced displacement cascades. We call this process *nano-implantation*, [8]. Thus, we try to draw a qualitative correlation between our results and those obtained during ion implantation at high temperature.

For implantations at room temperature, the evolution of the size of the precipitates depends either on annealing temperature and time, [17, 13], and on annealing atmosphere, [12]. However, few works deal with the ion beam synthesis at high temperature. For example, Strobel and al, [18], studied silica glass implanted with 2.75 MeV gold ions, with a fluence of $1.5\text{x}10^{17}$ cm^{-2} for temperatures in the range of 30-600°C. They show that the size of the NPs increases with the implantation temperature. Moreover, they obtain a qualitative agreement between the experimental results and kinetic Monte Carlo simulations. Similar results were obtained by Anderson et al, [19], for implanted indium, In, into soda lime glasses for temperatures ranging between 100 and 673 K.

The electronic stopping power (S_e) mainly favors the creation of defects within the silica matrix. During the irradiation these defects allows the gold atoms to diffuse and to precipitate upon fluctuations of the solute concentration above the supersaturation threshold. The type of defects created during the irradiation as well as their stability will depend on both the electronic stopping power and the irradiation temperature.

Oliver et al, [20], studied, by optical absorption and electron paramagnetic resonance measurements, the formation and the evolution with temperature of point defects in amorphous silica when irradiated with 4MeV Si^+ ions and 3MeV Au^{2+}, respectively. Two different kind of defects are observed: i) the neutral oxygen vacancy B2 defect ($\equiv$SiO$\bullet\bullet$Si$\equiv$) and ii) the oxygen vacancy E' defect ($\equiv$SiO$\bullet$). The authors show that the B2 defects preexist in virgin samples and that their density increases with irradiation fluence. On the other hand, E' defects are absent in the pristine samples. Their creation was ascribed to the irradiation with both Si and Au ions. In particular, the authors show that the energy deposited through the electronic

excitation mainly generates E′ defects.

A correlation between the density of E′ defects and the density of precipitates was found by Valentin et al, [21]. In these experiments glasses doped with copper atoms were irradiated at room temperature with 7MeV Si ions. A similar result was obtained by Oliver et al for silica irradiated with 3MeV and 10MeV Au ions, [20].

However, these defects becomes instable when the temperature is increased above a threshold value, [22, 23, 24, 25]. Griscom shows that in amorphous silica E′ defects start to recover from about 500°C, whereas B2 defects are stable up to about 900°C [26]. Thus, one should aspect that the density of the precipitates will be reduced when the temperature is increased above 500°C and 900°C, i.e. the recovering temperature for E′ and B2 defects, respectively.

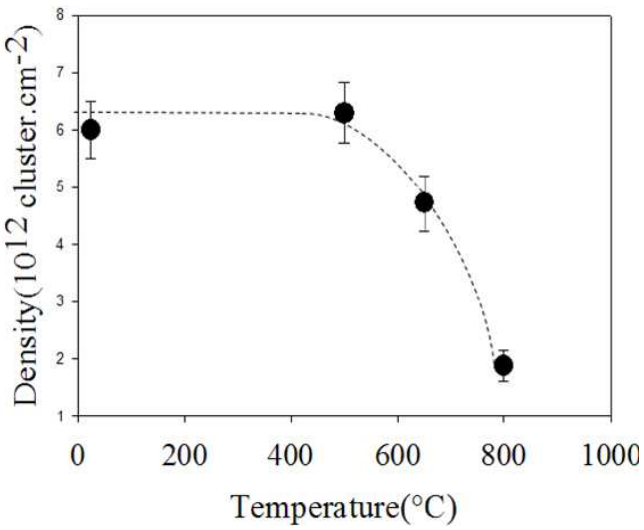

Figure 4.8: Evolution of the density of the precipitates, at a fluence of 8x10^{16} cm^{-2}, for temperature in the range 30-800°C.

Figure 4.8 shows the evolution of the density of precipitates (measured for the largest irradiation fluence) when the temperature is varied between 30°C and 800°C. This value remains constant at about 6x10^{12} cm^{-2} up to 500°C, then starts to decrease for higher temperatures, i.e. at 800°C the density is only 2x10^{12} cm^{-2}. Thus, a *qualitative* correlation can be tracked between the evolution of the irradiation-induced defects, especially E′, and the evolution of the precipitates under irradiation, i.e. their density. In particular, *the reduction of the nucleation sites, i.e. E′ defects, as well as the increasing of the irradiation-induced gold diffusivity with temperature favors the formation of larger precipitates.*

4.5 Conclusion

In conclusion, the irradiation of embedded NPs with MeV ions leads to both i) the dissolution of the pristine NPs and the growth of a precipitate second phase. At room temperature the system evolves toward a unique steady-state size, which is determined by the equilibrium size of the precipitates. However when either the irradiation temperature is increased or the nuclear stopping power decreased, a reduction of the dissolution rate of the embedded NPs is observed. This leads to the formation of a bimodal size distribution, the extend of which can be controlled by varying the temperature, the nuclear stopping power and the irradiation fluence. Besides, the steady-state size of the precipitates is observed to increases with the irradiation temperature. Furthermore, we find a qualitative correlation between the thermal stability of the E' defects and the reduction of the density of the precipitates when the irradiation temperature is above 500°C.

Finally, the introduction of several graphs, or schemes, describing the evolution of the size of both NPs and precipitates, their size dispersion and the size gap has been done with the aim to rationalize the choice of the irradiation condition to enhance the control of the final size distribution of the confined second phase.

Bibliography

[1] C. D'Orléans, J. P. Stoquert, C. Estournès, C. Cerruti, J. J. Grob, J. L. Guille, F. Haas, D. Muller, M. Richard-Plouet, Phys. Rev. B 67, (2003) 220101R

[2] R. Giulian, P. Kluth, L.L. Araujo, D.J. Sprouster, A.P. Byrne, D.J. Cookson, M.C. Ridgway, Phys. Rev. B 78 (2008) 125413

[3] E.A. Dawi, G. Rizza, M.P. Mink, A.M. Vredenberg, F.H.P.M. Habraken, J. Appl. Phys. 105 (2009) 074305

[4] G. Rizza, E.A. Dawi, A.M. Vredenberg, I. Monnet, Appl. Phys. Lett. 95 (2009) 043105

[5] G.C. Rizza, M. Strobel, K.H. Heinig, H. Bernas, Nucl. Instrum. Methods Phys. Res. B 178 (2001) 78

[6] Chapter 3, G.Rizza, H.Cheverry, T.Gacoin, A.Lamasson, S.Henry, J.Appl.Phys. 101,014321 (2007)

[7] Chapter 5 G.Rizza, Y. Ramjauny T. Gacoin, S. Henry, Nucl. Instr. Meth. B 257 (2007) 15

[8] Chapter 6 G.Rizza, Y.Ramjauny, T.Gacoin, L.Vieille, S.Henry , Phys.Rev.B 76, 245414 (2007)

[9] J.F. Ziegler, J.P. Biersack, and U. Littmark, The Stopping Ranges and Ranges of Ions in Solids Pergamon Press, New York, 1985; www.srim.org.

[10] Ph.Buffat, J-P Borel, Phys.Rev A 13 (1976) 2287

[11] K.Dick, T.Dhanasekaran, Z. Zhang, D.Meisel, J.Am.Chem.Soc.124 (2002) 10

[12] A.Miotello, G. De marchi, G.Mattei, P.Mazzoldi, C.Sada, Phys.Rev.B 63 (2001) 075409

[13] G.De Marchi, G.Mattei, P.Mazzoldi, C.Sada, A.Miotello, J.Appl.Phys. 92 (2002) 4249

[14] F. Ruffino, M.G. Grimaldia, C. Bongiorno, F. Giannazzo, F. Roccaforte, V. Raineri, Superlattices and Microstructures 44 (2008) 588

[15] I.M. Lifshitz, V.V. Slyozov , J.Phys.Chem.Sol. 19 (1961) 35

[16] V.C. Wagner, Z.Elektrochem. 65 (1961) 581

[17] D.Ila, E.Sarkisov, C.C Smith, D.B Poker, D.K Hensley, Nucl. Instr. Meth. Phys. Res. B 141 (1998) 289

[18] M.Strobel, K.-H.Heinig, W.Moller, A.Meldrum, D.S. Zhou, C.W. White, R.A. Zuhr, Nucl. Instr. Meth. Phys. Res. B 147 (1999) 343

[19] T.S.Anderson, R.H.Magruder III, R.A.Weeks, R.A.Zuhr, J. Non-Cryst. Sol. 203 (1993) 114

[20] A.Oliver, J.C.Cheang-Wong, A.Crespo, L.Rodriguez-Fernandez, J.M Hernandez, E.Munoz, R.Espejel-Morales, Mater.Sci.Eng. B 78 (2000) 32

[21] E.Valentin, Thesis Ecole Centrale, Paris (1999-42)

[22] R.A.B.Devine, Phys.Rev.B 35 (1987) 18

[23] R.A.B.Devine, J.Appl.Phys. 56 (1984) 2

[24] R.A.B.Devine, J.Appl.Phys. 58 (1984) 3368

[25] J.Robertson, J.Phys.C 17 (1984) L221

[26] D.L.Griscom, Nucl. Instr. Meth. Phys. Res. B 1 (1984) 481

Chapter 5

Dependence of the irradiation-induced growth kinetics of satellites on the nanoclusters dimension

Abstract

The aim of this chapter is to describe how the growth kinetics of the satellites is influenced by the initial size of the embedded NPs. In particular, with respect to the ion implantation, where the solute concentration is defined by the implantation dose, the irradiation, through the ion mixing, allows the solute to be continuously added to the system. In other words, the embedded NP can be considered as a solute reservoir. As the complete description of the growth kinetic process needs the knowledge of both the size and density of the satellites as a function of the irradiation fluence, insight into the kinetic mechanisms requires, besides the control of the irradiation parameter, also the careful control of the properties of the embedded NPs.

5.1 Introduction

Irradiation with MeV gold ions of embedded Au nanoparticles (NPs) in silica matrix results in the formation of a ring of satellites in its surrounding [1]. We show that both the size and the density of the satellites depend on the initial NP size. The same is true when the kinetic growth of the satellites is studied. Finally, we discuss the limitation of the ion implantation technique to study in detail the kinetic growth of a precipitate phase.

5.2 Experimental

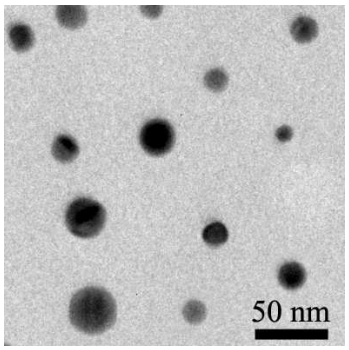

Figure 5.1: TEM micrograph of the unirradiated sample

All the irradiations described in the present work were performed with the ARAMIS accelerator, [2], at the CSNSM laboratory (Orsay, France). NPs with an initial size ranging from 8 up to 30 nm were irradiated with 4 MeV Au^{2+} ions at a fluence of 1.5x10^{16} cm^{-2} at room temperature (T=300K), figure5.1.

5.3 Results and discussion

Figure 5.2(a-d) show the formation of a satellite ring around Au NPs of different sizes irradiated with 4 MeV Au ions at a fluence of 1.5x10^{16} cm^{-2}. As all the NPs are embedded within the same matrix, the irradiation conditions are the same for all the NPs and the only varying parameter is the NP diameter, or its volume. Observing figure 5.2 we note that i) the size of the satellites, ii) their distance from the NP surface and iii) their number, depend on the size of the NP. TEM micrographs show that the satellites close to the NP surface are systematically larger than that formed at larger distances. Their nucleation and growth is directly sustained by the NP dissolution, where the latter is considered a solute reservoir. We call

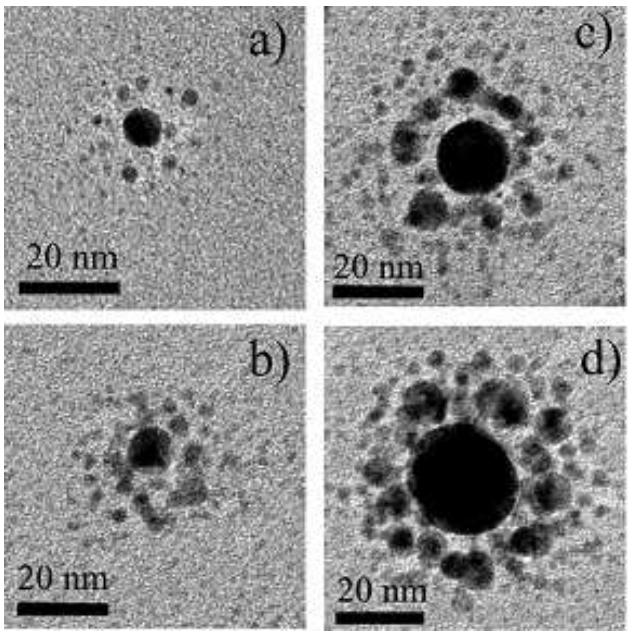

Figure 5.2: TEM micrograph of NPs with different sizes irradiated at a fluence of $1.5x10^{16}$ cm^{-2} with 4 MeV Au ions at room temperature. a) 5.8 nm, b) 8.7 nm, c) 16.7 nm and d) 25.1 nm.

these satellites of first generation. A second generation of satellites nucleates when the first one is large enough to create, through the irradiation mixing, a solute supersaturation at increasing distances from the NP surface, d_{NP}.

However, for increasing value of d_{NP}, the strength of the solute reservoir is reduced, because the solute is spread over a larger volume, $\sim d_{NP}^3$. As the solute concentration decreases with the distance from the NP, the nucleation and growth of new satellites do the same. As the study of this system is complicated, we limit our investigation to the evolution of the first generation of satellites, i.e. those close to the original NP. Experimentally, they are found in an annular region around the NP with a thickness ranging between 1-1.5 R_{NP}, where R_{NP} is the NP radius.

The corresponding satellite size distributions (SSD) are shown in figure 5.3(a-e). For the smallest NP size, 5.8 nm, the SSD is asymmetric with a tail toward the smaller size, figure 5.3a. Increasing the NP size to 8.7 nm results in quite symmetric SSD, figure 5.3b). For larger NPs, up to 16.7 nm, the SSD is asymmetric but with a tail toward the larger sizes, figure 5.3c. Finally, for the largest NP considered in the present work, 25.1 nm, the SSD becomes bimodal, figure 5.3d. This bimodal shape can be understood thinking that when the growing satellites reach a *critical* size their contribution to the solute concentration becomes large enough to enhance the nucleation of new precipitates in their vicinity. On the other extreme, the contribution of

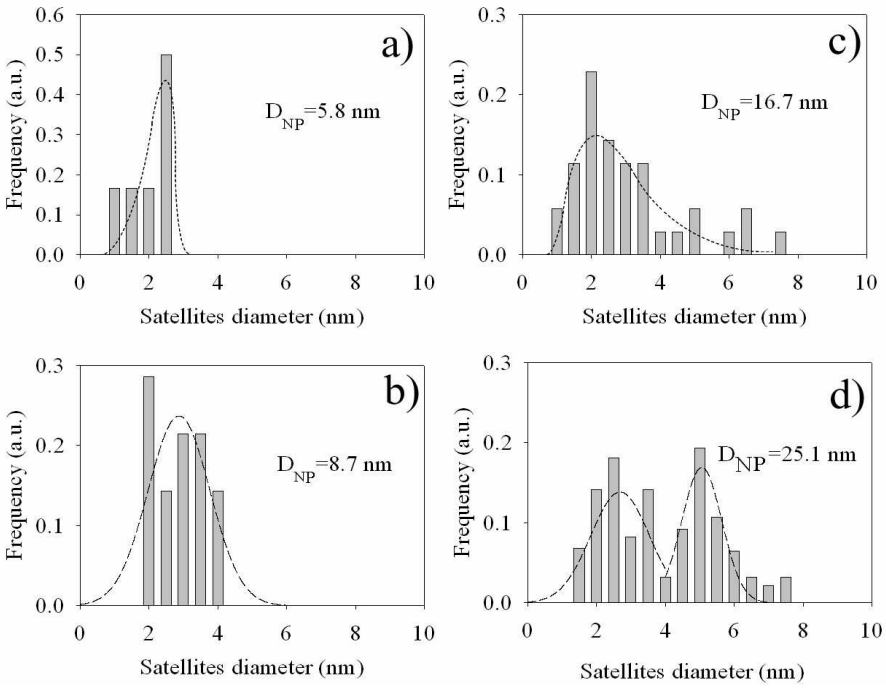

Figure 5.3: Satellites size distribution as a function of the NP size, as in figure 5.1

sub-critical satellites to the solute concentration is insufficient to sustain the nucleation and the growth of new precipitates, and the SSD remains unimodal. This is what we observe for the NPs of 5.8 nm and 8.7 nm. An intermediary situation is found for the 16.7 nm NP. Here, the contribution of the larger satellites to the supersaturation is sufficient to allow the nucleation of new precipitates in their surrounding. This leads to a SSD with a tail toward the larger sizes.

Figure 5.4 reports the evolution of the average satellite diameter as a function of the initial NP dimension. We found that the satellites mean diameter increases from 1.9 nm up to 3-3.5 nm for NP sizes ranging from 5 nm up to 10-12 nm. Further increasing of the NP size results in the saturation of the average satellites diameter to the value of about 4 nm.

The relation between the number of the satellites and the initial NP size is shown in figure 5.5a). A Linear correlation is observed up to about 20 nm, then a saturation appears. The satellites density can be calculated considering the number of satellites contained within the annular surface defines as:

$$S = \pi(R_{NP} + d_{NP})^2 - \pi R_{NP}^2 \tag{5.1}$$

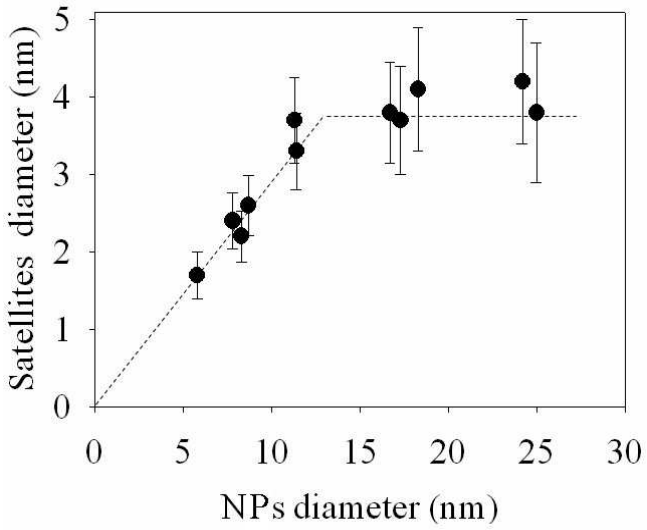

Figure 5.4: Relation between the NP size and the mean satellite size for a sample irradiated at a fluence of 1.5x10^{16} cm^{-2} with 4 MeV Au ions at room temperature.

where d_{NP} is the distance from the NP surface and R_{NP} the NP radius. The result is reported in figure 5.5b). The density scales approximatively with the inverse of the NP radius, $\rho_{satellites} \sim 1/R_{NP}$. This is due to the fact that the annular surface increases as $\sim R_{NP}^2$ whereas the number of satellites as $\sim R_{NP}$.

5.4 Conclusion

In conclusion, we have shown that the irradiation of NPs with different sizes leads to different values of both satellites size and density. In particular, the satellite size linearly scales with the NPs size before to saturate, whereas the density ranges approximatively as the inverse of the NPs radius. For example changing the NP size from 5 nm to 30 nm we obtain a satellite size of 1.9 nm and 4 nm and a density of 0.083 at.nm^{-2} and 0.014 at.nm^{-2}, respectively. This represents a variation of about 47 % in the size and 17 % in the density estimation. It is worth noting that also the shape of the size distribution function depends on the NPs size. SSD is asymmetric with a tail toward smaller sizes if the NPs are small (5.8 nm), is symmetric in shape for NPs of about 10 nm, and shows a tail toward the larger sizes for NPs of about 16 nm. Finally, it becomes bimodal NPs of 25 nm.

It is clear that starting with a large size distribution of NPs introduces errors in the measure of the kinetic processes under irradiation. In order to study the kinetics growth is therefore important to start with the narrowest

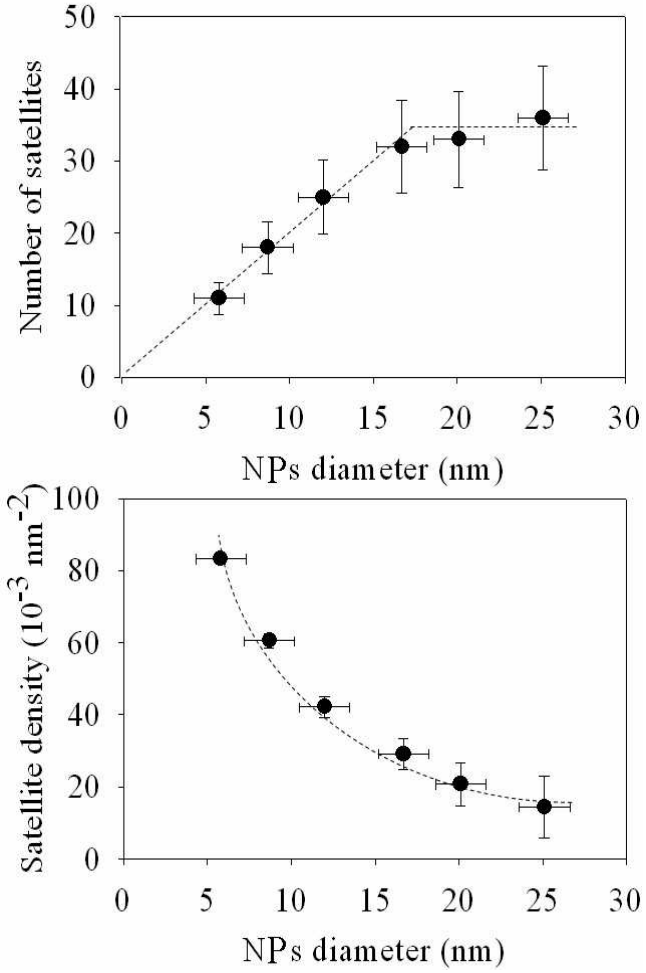

Figure 5.5: a) Number of satellites and b) the corresponding density as a function of the NPs size.

possible size distribution profile. In this regards both ion implantation and ion mixing, inducing balling-up of a continuous thin film are not adapted techniques, because the control of the size and the spatial dispersion of the embedded NPs is one of their main limitation.

On the other hand, the chemical synthesis of metallic NPs and the following sandwiching between two amorphous layers allows to overcome this constraint. The use of a *model* system where the size, the spatial distribution as well as the NPs concentration are perfectly controlled allows to precisely study the kinetic evolution of a precipitate phase under irradiation. This is the topic of the next chapter.

Bibliography

[1] Chapter 3, G. Rizza, H. Cheverry, T. Gacoin, S. Henry, J.Appl.Phys. 101,014321 (2007)

[2] E. Cotterau, J. Camplan, J. Chaumont, R. Munier, H. Bernas, Nucl. Instr. Meth. B 45 (1990) 293

Chapter 6

a Model System to Give Insights into the Nucleation and Growth under Irradiation

Abstract

In this chapter, the problem to rationalize and to improve the ion beam synthesis of NPs has been studied in detail. In particular, this work represents a tentative to go beyond in the description of the nucleation and growth of a precipitate phase under ion irradiation. The final objective is to provide a guideline method to overcome the limitations in controlling the NPs size and spatial distributions that are associated with the ion implantation technique. These limitations are mainly related to the difficulty in performing experiments with an appropriate control of the initial NPs conditions, which depend on the complex relation between particle growth through solute depletion, and particle dissolution, induced by displacement cascades triggered by the impinging ions.

6.1 Introduction

The control over the size and the dispersion of the ion beam-synthesized nanoparticles (NPs) is generally poor. This is partially due to the scarce knowledge of the behavior of the precipitate phase in the first steps of the nucleation and growth processes. To overcome this difficulty, the MeV irradiation-induced nucleation and growth of the satellites clusters around embedded NPs is studied in detail. Here the evolution of the satellite clusters by the MeV-ion irradiation-induced dissolution of gold NPs in a silica matrix has been investigated with a twofold purpose: i) to study the kinetics of the growth of the satellites. We show that it can be described by a diffusion-limited Ostwald ripening mechanism in an open system. ii) to determine the complete evolution of the Au solute concentration as a function of the fluence. It allows, in principle, to modify the temporal extension of the nucleation regime, and thus the final particles size distribution, by varying in a controlled way both the temperature and the irradiation parameters. Finally, we estimate: i) the concentration threshold for precipitation, ii) the surface tension of the gold particles and iii) the diffusion coefficient of the metal atoms within silica under irradiation.

6.2 Experimental

For the present study 15±2 nm Au NPs are embedded within a 500 nm silica layer. All the Au NPs are in a plane at 200 nm below the surface of the silica film. The samples were irradiated at room temperature and under a constant ion flux 1 μA.cm^{-2} with 4 MeV Au ions with using the ARAMIS accelerator, [1], of the CSNSM laboratory (Orsay, France).

Some comments are necessary to define the fluence range. In the previous chapters, [2], we observed that the evolution of the satellites can be described by a two-step process: : i) for low irradiation fluences (up to about 2-3x10^{16} cm^{-2}) satellites are observed to grow, directly sustained by the NP dissolution. ii) for fluences higher than about 4x10^{16} cm^{-2}, when the pristine NP is below a critical size, the satellites are partially dissolved by the irradiation. Thus, to describe the satellite kinetics we limit our investigation to the first regime, i.e. for fluences up to 2.2x10^{16} cm^{-2}.

The characterization of the samples was performed by transmission electron microscopy (TEM) with a 300 keV Philips CM30. The average size, the size distribution and the spatial distribution of the Au NCs were obtained in planar transmission electron microscopy (P-TEM), figure 6.1.

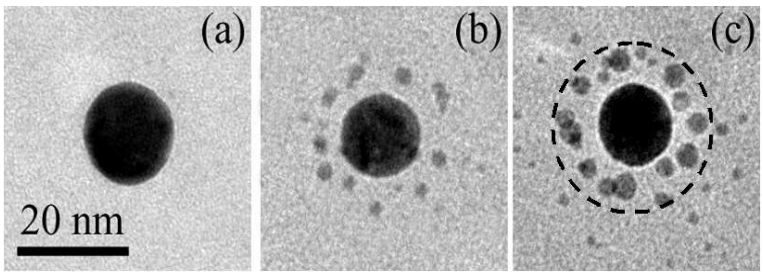

Figure 6.1: (a-c) TEM micrographs of Au NPs irradiated at increasing fluences with 4 MeV Au ions at room temperature. (c) the circle represents an eye-ball separation of the areas of growth of the two generations of satellites.

6.3 Results

Figure 6.1(a) shows a planar-view TEM micrograph of an as-prepared Au NP. Irradiation favors the formation of a halo of satellite clusters around each pristine NP, figures 1(b-c). For our TEM conditions, the minimum resolvable particle size is estimated to be about 0.5 nm. In a previous work, [2], we have shown that i) at low irradiation fluences, a *first generation* of satellites nucleate close to the NP surface, where the latter is considered a solute reservoir figure 6.1(b). ii) for higher irradiation fluences, a *second generation* of satellites nucleates at increasing distances from the NP surface, when supersaturation created by both the NP and the first generation of satellites overcomes a threshold value, figure 6.1(c). As the satellites close to the NP surface are systematically larger than those far from it, we limited our investigation to the evolution of the first ones, those close to the NP. Experimentally they are found within an annular region around the NP with a thickness ranging between 1 and 1.5 times the NP radius.

A simply electron diffraction analysis indicates that the fcc crystallographic structure of the NPs is not modified by the irradiation. Nonetheless, it is worth noting that very recently, Kluth et al. [3], using a more sophisticated EXAFS spectroscopy analysis showed that irradiation induces disorder in the crystalline nanophase.

Figures 6.2(a-f) show the evolution of the satellite size distribution (SSD) as a function of the irradiation fluence. The distributions are normalized to the number of satellites, i.e. the ordinate corresponds to their frequency of appearance, and fitted with a lognormal function using the average particle size and the standard deviation as parameters. Two different behaviors can be distinguished: i) the broadening of the SSD and, for larger fluences, the corresponding peak shift toward larger sizes. ii) the decrease of the nucleation frequency, i.e. the reduction of the number of satellites smaller than 1 nm. For example, at $0.5\text{x}10^{16}$ cm^{-2} about 60 % of the particles have a size less or equal to 1 nm. This value is reduced to about 20 % at $1.2\text{x}10^{16}$ cm^{-2},

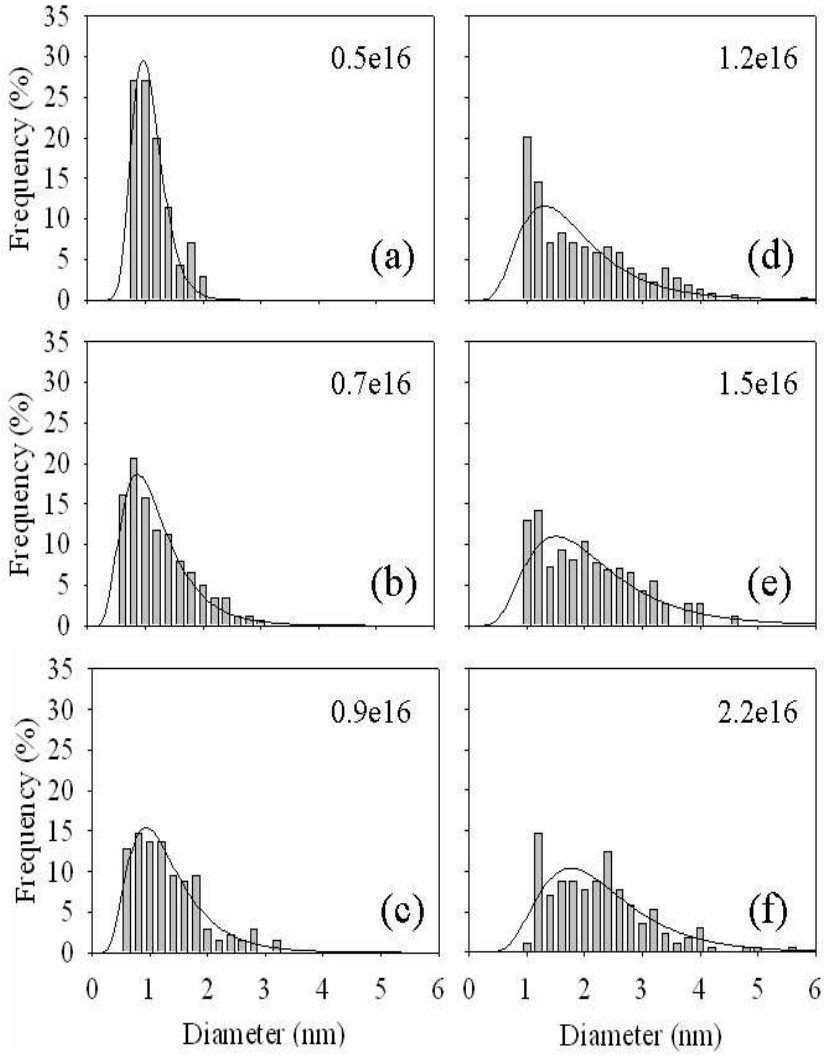

Figure 6.2: Size distributions of satellites as a function of the irradiation fluence.

and less than 5 % for a fluence of 2.2x10^{16} cm^{-2}.

Figure 6.3 shows the evolution of the satellites density. After a short transient regime a steady state value of about 15x10^{-3} particles.nm^{-2} is reached for fluences larger than 0.5x10^{16} cm^{-2}. Finally, above 1.5x10^{16} cm^{-2} a further increase is observed.

In figure 6.4 we report the evolution of the average satellite size with fluence, R(Φ). The experimental data have been interpolated using the power function R(Φ)=$a\Phi^b$. The best fit for this function gives a proportionality coefficient of a=0.74±0.04 and a time exponent of b=0.37±0.03, respectively. The corresponding correlation coefficient is $\Re$=0.99.

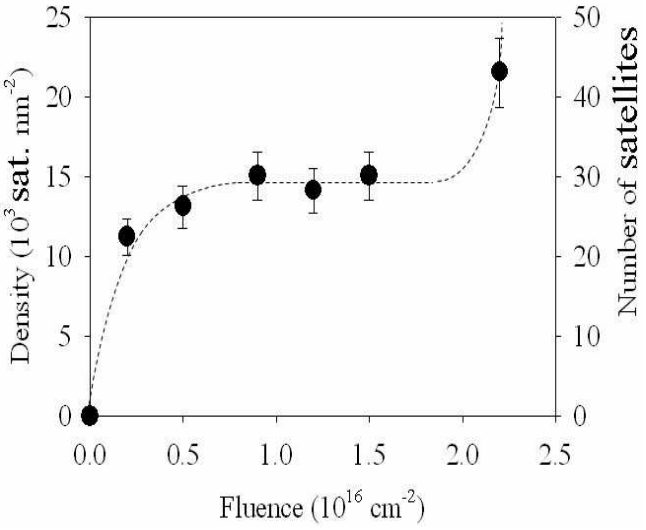

Figure 6.3: Evolution of the satellite density with irradiation fluence.

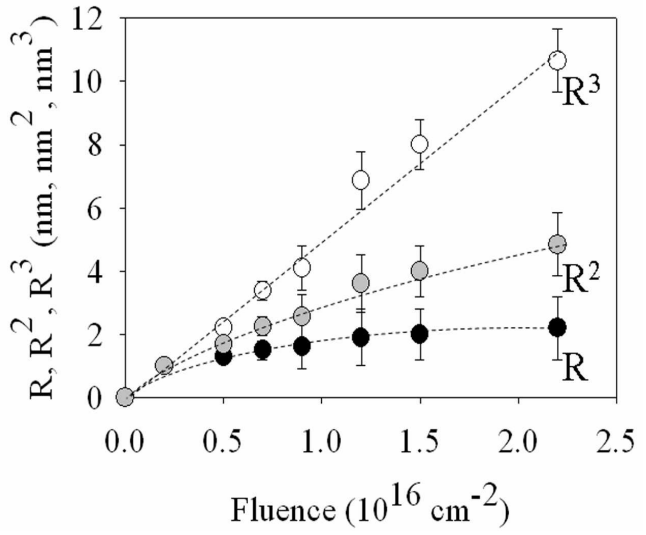

Figure 6.4: Evolution of the satellites mean size (R), square (R^2) and cube (R^3) as a function of the irradiation fluence.

Hence, to summarize we have shown that the evolution of the satellites under MeV irradiation is characterized by i) a constant reduction of the nucleation rate, ii) a steady-state value of the satellite density at least up to a fluence of 1.5x10^{16} cm^{-2} and iii) growth kinetics of the type $R(\Phi) \sim \Phi^{0.37 \pm 0.03}$.

6.4 Discussion

The study of the precipitates growth kinetics is virtually impossible with the ion implantation technique, due to the high fluence necessary to induce the precipitation, e.g. for gold in silica an implantation fluence larger than 10^{17} cm^{-2} is needed, [4]. However, MeV irradiation of pre-implanted samples allows to reduce the threshold implantation dose for nucleation by at least two orders of magnitude [5]. In our experimental set up ion irradiation is used with a double purpose: i) to promote the gold solute deposition into the silica matrix through the irradiation-induced NPs dissolution and ii) to enhance the satellites nucleation by reducing the nucleation threshold. This allows the precipitation to be observed already at a fluence of 10^{15} cm^{-2} and the evolution of the precipitate phase to be easily investigated. The basic idea of our approach is that the physics underlying the precipitation and growth of a second phase during ion implantation is equivalent to those that intervenes during the satellites nucleation and growth (Figure 6.5a-f). Here high solute concentration is deposited in small volumes around the NP, via the irradiation-induced displacement cascades. We call this process *nano-implantation*. Thus, studying the evolution of the satellite clusters under nano-implantation is a way to gain insight into the mechanisms of nucleation and growth under ion implantation.

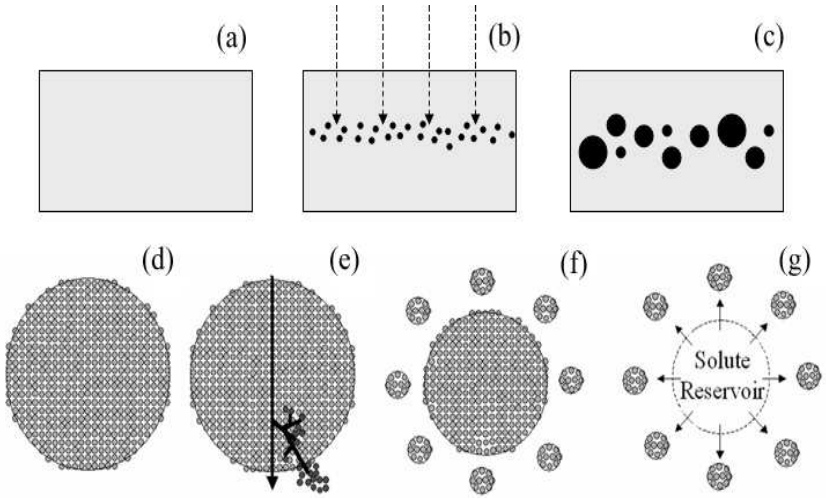

Figure 6.5: schematic representation of: (a-c) Implantation and (d-g) nano-implantation. (g) in an open system the NP can be replaced by a fictive solute reservoir

6.4.1 Theory

To describe the precipitation and growth under irradiation the classical nucleation and growth theory can be used, [6, 7]. The key parameter is

the supersaturation S(t) defined as $S(t)$=[C(t)-C_∞]/C_∞, where C(t) is the solute concentration at a given time and C_∞ is the bulk solubility. However, although the satellite nucleation and growth is directly sustained by the dissolution of the original NP, its evolution can be described in two ways: i) the ensemble composed of the original NP and the surrounding satellites can be considered as a 'closed system', i.e. the external flux of matter is zero. In such a 'conservative system', the irradiation allows the total mass of the pristine Au particle to be spatially redistributed over a larger *fixed* volume containing also the satellites. ii) the evolution of the satellites can be described as produced by an external monomer supply. In this case, the original NP, acting as a solute source, can be replaced by a fictive solute reservoir as shown in figure 6.5g. Here, the satellite precipitation occurs in a finite region with open mass exchange with neighboring regions of different concentration. As, in principle, the two choices are equally appropriate, we extend the formulation of the particle growth by considering both closed and the open systems.

Depending on S(t), the phase separation in a supersaturated solid solution can - both for closed and open systems - be divided into distinct stages:

Supersaturation regime

As soon as the solute is introduced into the host matrix, e.g. during ion implantation or nano-implantation, S(t) increases linearly as a function of the amount of monomers deposited. This goes on up to a critical value, S_c, at a time t_1, after which spontaneous nucleation sets in. It is worth noting that due to the fact that ion-implantation or nano-implantation are non-equilibrium processes it is possible to introduce concentrations of dopants into a solid matrix that are much higher than the equilibrium dopant solubility. Thus S_c is generally higher than the bulk solubility, i.e. S=1.

Nucleation regime

When the solute concentration, S(t), exceeds S_c, stable embryos start to form. Owing to the occurrence of nucleation and subsequent growth of the nuclei (e.g. the precipitates act as a sink for the diffusing solute), S(t) starts to decrease despite the ongoing monomer deposition, and the supersaturation eventually drops below the nucleation threshold at a time t_2. The region between t_1 and t_2 is usually referred to as the *nucleation* region.

Growth regime

Below S_c, the nucleation of new particles is inhibited and all the existing precipitates grow by incorporating the incoming monomers. Hence, the number of the particles reaches a steady state value, [8]: N(t)$\sim$Const.

Conversely, the diffusion of monomers to the particle interface and their absorption *via* the interface reaction drives the precipitates growth. The kinetic laws are i) limited by the diffusion, if the monomer absorption is the faster process or ii) limited by the interface kinetics, if the monomer diffusion is the faster process. A general expression for the particle growth rate, valid for both closed and open systems, writes [9, 10]:

$$\frac{dR}{dt} = \frac{KC_\infty \Lambda_C}{R_C}\left(\frac{1 - R_C/R}{1 + \epsilon R}\right) \tag{6.1}$$

where R is the particle radius, K is the rate of monomer absorption at the particle surface, σ the surface tension, $\mathrm{R}_C{=}\Lambda_C/S(t)$ the critical particle radius, Λ_C the capillarity length, $\epsilon^{-1}{=}\mathrm{D_0V}a/\mathrm{K}$ the screening length, D_0 the diffusion coefficient and V_a the molar volume.

In Eq. 6.1 the factor $\epsilon\mathrm{R}{=}\mathrm{KR}/\mathrm{D_0V}a$ determines the dominating mechanism. When $\mathrm{KR}{\ll}\mathrm{D_0V}a$, the growth is limited by the reaction-interface and for $\mathrm{R}{\gg}\mathrm{R}_C$, [11], the number of particles and the particle radius scale as:

$$N \propto constant, \tag{6.2a}$$

$$R \propto t. \tag{6.2b}$$

When $\mathrm{KR}{\gg}\mathrm{DV}_A$ the growth is limited by the diffusion of the monomers. Considering the asymptotic solution ($\mathrm{R}{\gg}\mathrm{R}_C$) the number of particles and the particle radius evolve as:

$$N \propto constant, \tag{6.3a}$$

$$R \propto t^{0.5}. \tag{6.3b}$$

Ostwald ripening regime

When the supersaturation reaches a sufficiently low value, the smaller particles becomes instable and eventually dissolve, since the critical radius of the particles scales as the inverse of the supersaturation level, i.e. $\mathrm{R}_C{\propto}1/S(t)$. This regime is called *Ostwald ripening* (OR). The evolution of a precipitate phase in the OR regime is different for closed and open systems.

a) In *closed systems* the mass is conserved. The supersaturation cannot remain constant indefinitely and thus decreases with the time. The system evolves towards a redistribution of the mass that minimizes the total free energy. Interface effects becomes important and the smaller precipitates dissolve in favor of the larger ones. The description of the evolution of the particles in an Ostwald-Ripening (OR) regime was originally developed by Lifshitz, Slyozov, [12], and Wagner, [13], and is nowadays knows as the LSW theory.

If the monomer assimilation is limited by the *interface reaction* the precipitates size and number evolve as:

$$R \propto t^{0.5}, \tag{6.4a}$$
$$N \propto t^{-1.5}. \tag{6.4b}$$

On the other hand, for surface absorption limited by the *diffusion of the monomers* one has:

$$R \propto t^{0.33}, \tag{6.5a}$$
$$N \propto t^{-1}. \tag{6.5b}$$

b) In an *open system*, the continuous monomer supply allows the particle dissolution to be reduced, or eventually stopped. This mechanism is called *Ostwald ripening in an open system* or *Second Independent Growth* (SIG) [14]. In an open system the kinetic laws are the same as for the particles evolving under mass conservation. However, the scaling law for the number of particles is different and depends on the absorption mechanism, [14, 15].

If the monomer absorption is limited by the *surface reaction* the particle size and number evolve as:

$$R \propto t^{0.5}, \tag{6.6a}$$
$$N \propto t^{-0.5}. \tag{6.6b}$$

On the other hand, in the *diffusion-limited* regime they evolve as:

$$R \propto t^{0.33}, \tag{6.7a}$$
$$N \propto constant. \tag{6.7b}$$

6.4.2 Kinetic evolution of satellites

The mechanism controlling the evolution of an ensemble of particles in a supersaturated solid solution can be characterized knowing i) the size distribution function, $f(\mathrm{R}(\Phi))$, ii) the change of the particle radii with time, $\mathrm{R}(\Phi)$ and iii) the evolution of the number of particles, $\mathrm{N}(\Phi)$.

De Lamaestre et al., [16], have recently shown that when ion implantation is involved, the nucleation and growth history of the clusters is no longer revealed by the distribution function, which often evolves towards a lognormal shape. As the kinetic evolution of the second phase does not lead to the predicted distribution shape, experimental distributions cannot be used to discriminate among different regimes. Conversely, the other two

quantities, R(Φ) and N(Φ), are experimentally accessible. First, we analyze the evolution of the average particle radius with fluence, R(Φ). The time, t, is linearly related to the fluence *via* the constant ion flux, φ, i.e. $\Phi=\varphi \cdot t$. In the results section we showed that the fluence exponent for satellite growth is 0.37±0.03, as can be seen in figure 6.4. According to the theoretical predictions summarized in Tab 6.1, any possible link with the growth regime can be ruled out since the particle size scales as R∼t, for the reaction-limited, and as $R \sim t^{0.5}$, for the diffusion limited kinetics.

Moreover, the OR regime governed by interface reactions can also be excluded as the satellite sizes scale as $R \sim t^{0.5}$. Hence, both for closed or open systems the time exponent can only correspond to OR within a diffusion-limited regime. To discriminate between the two options, we look at the evolution of the number of satellites, N(Φ) (Figure 6.3). After a rapid increase at the beginning of the irradiation, N(Φ) reaches a steady state value up to a fluence of 1.5×10^{16} cm^{-2}, then it starts to increase. This depends on the fact that for higher irradiation fluences the original NP can no longer be considered as an infinite solute reservoir [2].

Table 6.1: Evolution of the radius and the number of the precipitate phase within the regimes of growth and coarsening within closed and open systems.

	Growth regime		**Ostwald Ripening regime**	
	Close system	Open system	Close system	Open system
Interface kinetics limited regime ($Kr \ll DV_A$)	$R \propto t$ $N \sim$Constant	$R \propto t$ $N \sim$Constant	$R \propto t^{0.5}$ $N \sim t^{-1.5}$	$R \propto t^{0.5}$ $N \sim t^{-0.5}$
Diffusion limited regime ($Kr \gg DV_A$)	$R \propto t^{0.5}$ $N \sim$Constant	$R \propto t^{0.5}$ $N \sim$Constant	$R \propto t^{0.33}$ $N \sim t^{-1}$	$R \propto t^{0.33}$ $N \sim$Constant

As inspection of the Tab. 6.1 reveals, the only mechanism accounting for our experimental results, $R(\Phi) \sim \Phi^{0.37}$ and N(Φ)∼Const., is the *OR regime in an open system, i.e. under a monomer supply that is diffusion limited.*

To conclude this section we can say that when the embedded NP can be considered as an infinite solute source, i.e for low irradiation fluences, the second phase precipitation can be studied by subdividing the problem into two parts: i) the irradiation-induced NP dissolution, i.e. the evolution of the solute reservoir and ii) the particle growth under external monomer supply. In the latter case the classical nucleation and growth theory can be applied.

6.4.3 Nucleation fraction

In this section we analyze the evolution of the nucleation fraction with irradiation, n(Φ).

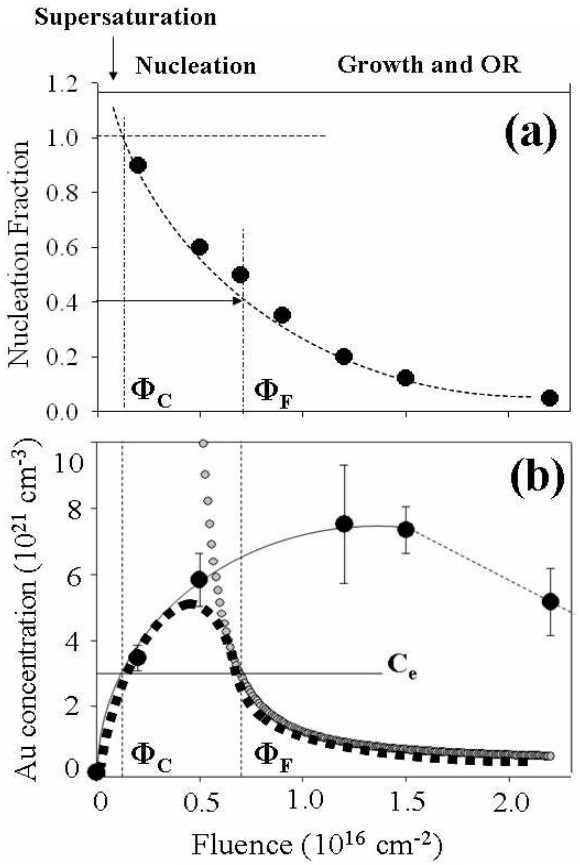

Figure 6.6: (a) evolution of the nucleation fraction of the satellites with fluence, i.e. the fraction of satellites smaller than 1 nm. (b) the evolution of Au solute concentration with fluence can be estimated by considering two opposite terms: i) the full black circles represent the continuous monomers addition into the matrix due to the irradiation-induced NC dissolution. ii) the full gray circles represent the evolution of solute concentration into the matrix above the nucleation threshold. The difference between the two curves is related to the amount of solute which is absorbed by the growing NPs. Finally, the dashed line describes the complete evolution of the Au solute concentration with fluence.

It is obtained from satellite size distributions, figure 6.2, by normalizing the number of satellites with radius smaller than 1 nm to the their total number, N(Φ). The result is shown in figure 6.6(a).

The experimental data can be fitted with an exponential decay function, indicating that the nucleation of new satellites decreases with the irradiation:

$$n(\Phi) = a * exp(-b\Phi) \tag{6.8}$$

The best fit is obtained for a=1.22 and b=0.145x10^{-15} at^{-1}.cm^2. The corresponding correlation coefficient is $\Re$=0.998. Several parameters can be determined from the inspection of the figure 6.6(a): i) the fluence threshold for nucleation, Φ_C, ii) the fluence corresponding to the end of the nucleation regime, Φ_F, and iii) the time-dependent nucleation rate. Φ_C corresponds to the condition n=1, i.e. all the particles have a size smaller than 1 nm, and is given by Φ_C∼0.16x10^{16} cm^{-2}. Of course it represents an upper limit of the threshold fluence for nucleation. Φ_F can be estimated as the characteristic length of the Eq. 6.8, i.e. Φ_F=1/b∼0.68x10^{16} cm^{-2}. The nucleation-rate, *dn(Φ)/d*Φ, can be used to determine the change of the supersaturation with irradiation and will be calculated in the following sections.

6.4.4 Estimation of the concentration threshold for satellites nucleation

Nucleation is expected to set in when the solute concentration exceeds a nucleation threshold, c$_e$. In the previous section we estimated the critical fluence for nucleation to be Φ_c=0.16x10^{16} cm^{-2}. During irradiation an original NP is progressively dissolved. The number of atoms displaced into the silica matrix at Φ_c is simply given by ΔN(Φ_c)=c$_p\Delta$V$^{NP}_{\Phi_c}$=1.6x10^4 at. Here c$_p$=5.9x10^{22} at.cm^{-3} is the gold bulk density and ΔV$^{NP}_{\Phi_c}$=4/3π[R^3(0)-R^3(Φ_c)] is the NP dissolved volume at Φ_c as measured from TEM micrographs. Once in solution, the Au atoms can diffuse over a volume ΔV^{SAT} before precipitation occurs. The latter is experimentally estimated from TEM micrographs as the volume containing the satellites at Φ_c, ΔV$^{SAT}_{\Phi_C}$∼5.6x10^{-18} cm^3. Thus, an upper limit of c$_e$ can be evaluated to be:

$$c_e = c_p \frac{\Delta V^{NP}_{\Phi_C}}{\Delta V^{SAT}_{\Phi_C}} \sim 2.8x10^{21} at.cm^{-3} \tag{6.9}$$

In Eq. 6.9 all the parameters are experimentally determined with the exception of the NP atomic density, C$_p$, defined as the bulk density for gold. Although C$_p$ could be modified by the intermixing of the matrix recoils (Si and/or O), several elements can be given to justify the validity of our approximation: i) SRIM simulations show that the implantation depth of Si and O into Au is nearly limited to the very first NP surface. ii) irradiation-induced vacancies aggregation and voids formation already observed in other systems, e.g. [4], were not evidenced by our TEM analysis. ii) EXAFS measurements indicate that pre-implanted impurities, Si and O atoms (10 % at.), into an Au film do not affect its atomic structure when irradiated with 2.3 MeV Sn ions, [3].

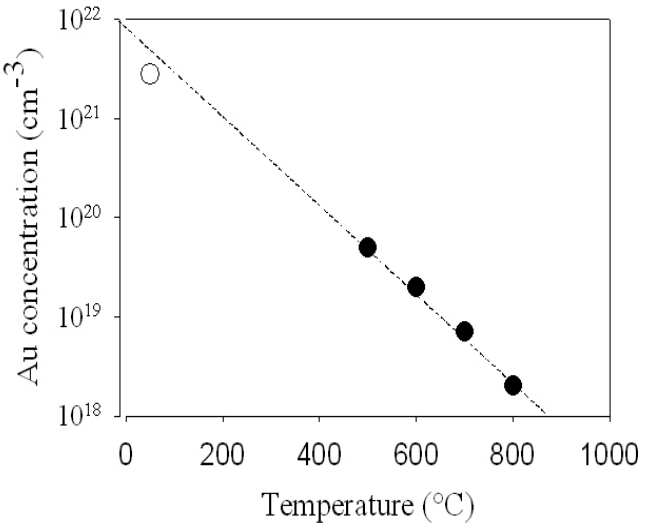

Figure 6.7: The full circles represent the experimental threshold values for gold nucleation in silica within the temperature range 500-800 °C, as taken from Ref. [17]. The extrapolation of these to lower temperatures is given by the dotted line. The open circles represent our estimates at room temperature.

In the literature only few estimations of the nucleation threshold exist. Ila et al., [4], found that an upper limit of c_e for gold in silica at 1200°C is below c_e<9x10^{21} at.cm^{-3}. Recently, Ramaswamy et al.,[17], calculated the variation of c_e for temperatures ranging between 500°C and 800°C. These are reported in figure 6.7 (full circles) together with our estimation at room temperature (open circles). The dotted line is simply the extrapolation of c_e towards the low temperature regime. Clearly our estimation agrees reasonably well with the data of reference [17].

6.4.5 Evolution of the solute concentration with fluence

The evolution of the solute concentration with irradiation depends on two opposite terms: i) the continuous addition of monomers, which is due to the NP dissolution and which enhances the metal concentration within the host matrix and ii) the absorption of monomers into the forming and the growing particles, which favors the decrease of the total amount of available solute.

The first term can be calculated as in the previous section, where now the dissolved volume of the NP and the annular region containing the satellites are determined for all the irradiation fluences:

$$c(\Phi) = c_p \frac{\Delta V^{NP}(\Phi)}{\Delta V^{SAT}(\Phi)} \tag{6.10}$$

The evolution of the solute concentration with fluence is shown in figure 6.6(b), the full black circles. Here, the concentration of dissolved monomers increases with fluence up to 1.5x10^{16} cm^{-2} and then decreases. In a previous work, we showed that when the size of the original NP becomes comparable to that of the surrounding satellites each particle turns into an equivalent solute source and a regime change occurs in the satellites evolution, [2]. Hence, the reduction of the solute concentration, associated with the observation of the increasing of the satellite density for fluences larger than 1.5x10^{16} cm^{-2}, clearly indicates that a new regime is active and that the original NP cannot be no more considered as an infinite solute source.

The second term, corresponding to the solute concentration above the fluence threshold for nucleation, Φ>Φ_c, can be calculated using the classical nucleation theory, [18, 7]:

$$I(t) = I_0 exp\left[\frac{-B}{(LnS(t))^2}\right] \tag{6.11}$$

where I(t) is the nucleation rate, I$_0$ is the maximum nucleation rate, S(t) the supersaturation, B=16$\pi\sigma^3$V$_a^2$/3(kT)^3, σ is the surface tension, V$_A$ the molar volume, k Boltzmann's constant and T the temperature. Rearranging Eq. 6.11, the supersaturation, S(t), writes:

$$S(t) = exp\left[\frac{-B}{2Ln(I/I_0)}\right] \tag{6.12}$$

The evolution of the gold supersaturation in silica matrix is found by equating the relative nucleation rate, I/I_0, to the experimental one, I^{exp}/I_0^{exp}. I^{exp} is obtained by differentiating the Eq. 6.8, I^{exp}=$\dot{n}(\Phi(t))$, and the maximum experimental nucleation rate is given by I$_0^{exp}$=$\dot{n}(\Phi_C)\cdot\varphi$=4.4x10$^{-4}\cdot$ s^{-1}, where $\dot{n}(\Phi_C)\simeq$1.4x10^{-16} cm^2 and φ=3.12x10^{12} at.cm^{-2}.s^{-1}. We obtain:

$$S(\Phi) = exp\left[\frac{B}{2b\,(\Phi - \Phi_C)}\right] \tag{6.13}$$

where b=0.145x10^{-15} at^{-1}.cm^2 and Φ_C=0.16x10^{16} cm^{-2}. Finally, an expression for the solute concentration is obtained by multiplying Eq. 6.13 by the equilibrium concentration, C$_\infty$:

$$C(\Phi) = S(\Phi)C_\infty = exp\left[\frac{8\pi\sigma^3 V_a^2}{3b(kT)^3\,(\Phi - \Phi_C)}\right] C_\infty \tag{6.14}$$

where kT=5x10^{-21} J and V$_a$=1.6x10^{-23} cm^3. The only two unknown parameters of Eq. 6.14 are the equilibrium concentration, C$_\infty$, and the surface tension, σ. However, a condition for the fit is imposed by the fact

that the nucleation regime ends at Φ=Φ_F, where the supersaturation must be C(Φ_F)=C_e. The best fit for Eq. 6.14 is given in figure 6.6(b), the full gray circles. The surface tension has been estimated to be in the range of σ∼1-2.2x10^{-5} J.cm^{-2}. It is worth noting that this slight variation is obtained by changing the equilibrium concentration over orders of magnitude, e.g. 10^{10}-10^{21} cm^{-3}.

The combination of Eq. 6.10 and Eq. 6.14 represents the complete evolution of the solute concentration with irradiation, i.e. the dashed line in figure 6.6(b). The supersaturation regime crosses over into the nucleation regime at a fluence of about Φ_C∼0.16x10^{16} cm^{-2}, and it turns into the growth regime for fluences higher than Φ_F∼0.68x10 ^{16} cm^{-2}.

The possibility to estimate the evolution of the supersaturation with fluence allow us to study how the irradiation parameters modify the nucleation and growth regimes. It is clear that when the nucleation window is temporally large the final size distribution will be broad, because the particles can nucleate (and grow) at different times. On the other hand, the shorter the nucleation regime, the narrower the final particles dispersion. As all the particles nucleate (and grow) at almost the same time. Thus, a way to tailor the final size distribution of the precipitates is to modify the nucleation window by varying in a controlled way both the temperature and the irradiation parameters.

6.4.6 Surface tension of the gold NPs under irradiation

The surface tension of ion-beam-synthesized gold NPs embedded in a silica matrix has been estimated by several authors. A value of 4x10^{-4} J.cm^{-2} was extrapolated by De Marchi et al., [19], from TEM measurements. Values of 3.6x10^{-4} J.cm^{-2}, [20], and 3.4x10^{-4} J.cm^{-2}, [21], were deduced by Kluth et al. form EXAFS experiments using a simple liquid-drop model, [22]. All these results are in good agreement with those obtained for free-standing NPs, suggesting a negligible influence of the silica matrix, e.g. Buffat et al., [23], give 1.38x10^{-4} J.cm^{-2}, whereas Balarena et al., [22], obtain 3.46x10^{-4} J.cm^{-2}. However, our value is one order of magnitude lower than the previous ones, 1-2.2x10^{-5} J.cm^{-2}. Thus, in the following we try to account for this discrepancy.

There is a crucial difference between our experiment and the former ones in as far as the experimental set-up is concerned:

i) in all the previous works, gold NPs precipitate during the post-implantation annealing treatment, i.e. the NPs grow under purely thermal conditions,

ii) in our case, gold NPs form by the irradiation-induced dissolution of the gold particles and by solute re-precipitation in their surroundings, i.e. the NPs grow under irradiation conditions.

It is evident that irradiation drives the irradiated system away from its equilibrium state. This is due to the forced atomic relocation induced by

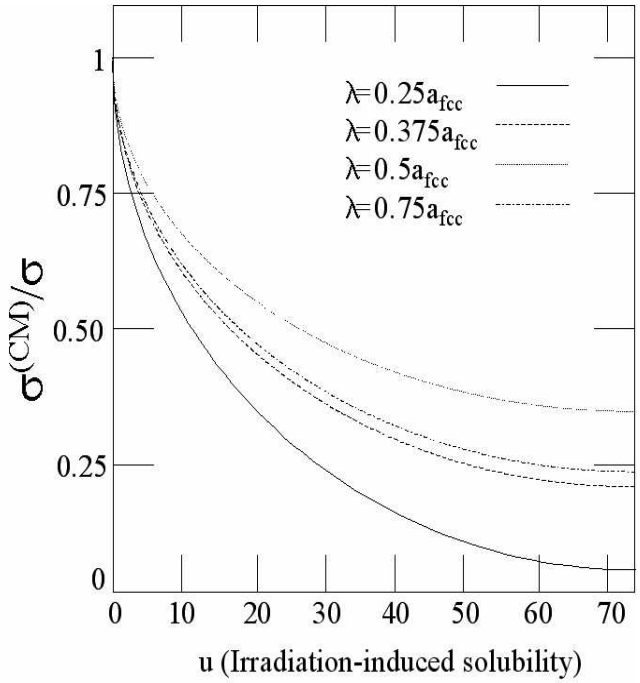

Figure 6.8: Monte-Carlo simulation showing the decrease of the surface tension under irradiation σ^{MC} with respect the equilibrium value, σ, as a function of the ballistic force, u, for different values of the mixing length, λ, from [24].

nuclear collision. In other words, the displacement cascades perturb the equilibrium conditions at the particle surface modifying the value of the surface tension. This effect has been nicely described by Strobel et al., [24], using the K3DLMC code. In figure 6.8 the ratios of values of the surface tension under irradiation, $\sigma^{(CM)}$, to their values within the purely thermal case, σ, are represented as a function of the mixing length, i.e. the average distance at which monomers are displaced from the NP surface, and the ballistic force, u, i.e. the strength of the solute source. The ratio $\sigma^{(CM)}/\sigma$ decreases as the source strength, i.e. the u parameter, is increased.

Heinig et al., [25], have recently shown that the asymptotic expression for the steady-state concentration of a NP under irradiation takes an expression equivalent to that of the Gibbs-Thomson: $C^I(R)=C^I_\infty(R)(1+R^I_C/R)$, where C^I and R^I_C are, respectively, the equilibrium solute concentration at planar surface and the capillarity length under irradiation. The model predicts that irradiation reduces the surface tension, i.e. the value of the capillarity length R^I_C, and that for appropriate irradiation conditions an effective negative value of the surface tension can be achieved. Similar conclusions have been drawn by other recent theoretical studies, [26, 27].

Although, additional work is needed to clarify the influence of the ion-matter interaction on the decrease of the surface tension, our estimation represents, to our knowledge, the first experimental determination of the effective surface tension of gold NPs under irradiation.

6.4.7 Diffusion coefficient under irradiation, D_{RED}

Rizza et al., [2], have shown that the diffusion coefficient under irradiation, D_{RED}, can be qualitatively related to the maximum distance at which satellites were found, L_{MAX}, [28, 29, 30]:

$$D_{RED} = \frac{L^2_{MAX} \cdot \varphi}{\Phi} \tag{6.15}$$

where Φ is the irradiation fluence and φ the constant ion flux. Using this expression, here we provide a quantitative estimation for D_{RED}.

In Figure 6.9 the evolution of $L_{MAX}(\Phi)$ with the fluence is shown. The experimental data are fitted with the function:

$$L_{MAX} = a \cdot \Phi^{0.5} \tag{6.16}$$

where $a=(D_{RED}/\varphi)^{0.5}=0.6$ nm is the free parameter and $\varphi=3.12\text{x}10^{-2}$ ions.s^{-1}.nm^{-2}. Thus the diffusion coefficient under irradiation is simply given by:

$$D_{RED} = a^2 \cdot \varphi \simeq 3.8x10^{-16} cm^2.s^{-1} \tag{6.17}$$

De Marchi et al., [19], estimated the diffusion coefficient during post-implantation annealing experiments at 900° C to be $D\sim5\text{x}10^{-17}$ cm^2.s^{-1}. On

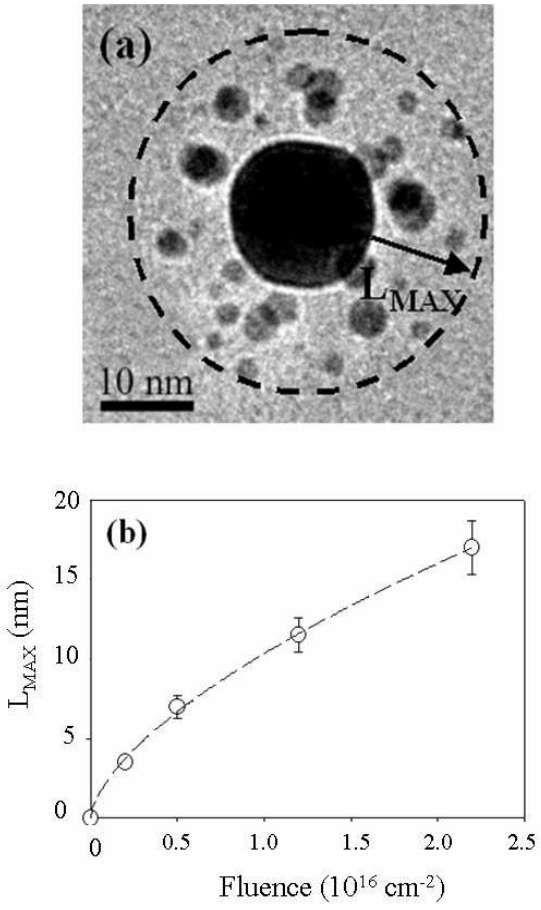

Figure 6.9: (a) Bright-field image of a sample irradiated with a fluence of 1x10^{16} cm^{-2}. The maximum satellite-clusters distance is indicated by the dotted circle (b) Increase of the maximum satellite-clusters distance (as calculated from the original cluster surface) as a function of the fluence of the irradiating ions.

the other hand, Rizza et al. [31] give a crude estimation of D_{RED} based on the ratio of thermal to irradiation-enhanced diffusion and the ion beam-induced displacement rate deduced from the SRIM code, D$\sim$1.5x10^{-16} cm^2.s^{-1} . Our estimation is comparable to the latter. This may be related to the amount of defects created by the irradiation, enhancing the atomic mobility more efficiently than in the purely thermal case. This is consistent with Martin's model, [32], which states that a solid solution under irradiation at temperature T (and flux φ) is equivalent to the one evolving at an higher effective temperature, i.e. T^{irr}=T[1+Δ(T,φ)]. Thus we can conclude that the diffusivity of the gold solute under MeV Au ions irradiation at room temperature corresponds to a fictive temperature above 900° C.

6.5 Conclusion

The way one must follow to improve the final particle monodispersity is to separate the nucleation and growth processes. The new ion-based methodologies operate within this direction. However, their main limitations are related to our poor knowledge of the behavior of the precipitate phase in the first stages of the nucleation, which prevents the possibility to precisely control the final particle properties. This work was motivated by the ambition to fill this gap and represents a first step in the quantitative description of the precipitation process as obtained through ion implantation.

In summary, using Au colloids embedded in a silica matrix as a model system and considering the original NP as a fictive solute source, we show that the evolution of the precipitate phase under irradiation is successfully described by an Ostwald ripening mechanism in an open system limited by the diffusion. Moreover, we estimate the concentration threshold for nucleation as well as the surface tension and the gold diffusivity in silica under irradiation. To conclude, our approach makes it possible to assess the evolution of the *(nano-)implanted* solute with the irradiation, in particular the extent of the nucleation regime. In this respect, further experiments are scheduled to modify this regime in a controlled way by playing both with the irradiation parameters and with the temperature. The final key issue is the optimum control of the nanostructures, when these are synthesized with ion-beam-related techniques.

Bibliography

[1] E.Cottereau, J.Camplan, J.Chaumont, R.Munier, H.Bernas, Nucl. Instr. Meth. B 45 (1990) 293

[2] Chapter 3, G.Rizza, H.Cheverry, T.Gacoin, A.Lamasson, S.Henry, J. Appl. Phys. 101 (2007) 14321

[3] P. Kluth, B. Johannessen, G.J. Foran, D.J. Cookson, S.M. Kluth, M.C. Ridgway, Phys. Rev. B 74 (2006) 14202

[4] D.Ila, E.K.Williams, S.Sarkisov, C.C.Smith, D.B.Poker, D.K.Hensley, Nucl. Instr. Meth. B 141 (1998) 289

[5] D. Ila, , E. K. Williams, R. L. Zimmerman, D. B. Poker and D. K. Hensley, Nucl. Instr. Meth. B 166 (2000) 845

[6] In: D.A. Porter and K.E. Easterling, Phase Transformations in Metals and Alloys 2nd edition, Nelson Thornes, (2001)

[7] In: L. Ratke, P.W. Voorhees, Growth and Coarsening, Springer (2002)

[8] M. Strobel, K.H. Heinig, W. Möller, A. Meldrum, D.S. Zhou, C.W. White, R.A. Zuhr, Nucl. Instr. Meth. B 147 (1999) 343

[9] I.H. Leubner, J. Phys. Chem. 91 (1987) 6069

[10] K. Nozawa, M.-H. Delville, H. Ushiki, P. Panizza, J.-P. Delville, Phys. Rev. E 72 (2005) 011404

[11] In the growth regime the supersaturation is still relatively high, thus, Rc can be very small and a stable embryo can be composed by only few atoms. In this regard, EXAFS measurements indicate that Au atoms, displaced from the Au NP into the silica matrix by 2.3 MeV Sn ions, can form very small clusters composed by only dimers, trimers..., [3]. As in our experiment R>0.5 nm, e.g. larger than the smallest resolvable NP, the condition R$\gg$Rc is satisfied.

[12] I.M. Lifshitz, V.V. Slyozov, J. Phys. Chem. Solids 19 (1961) 35

[13] V.C. Wagner, Z. Electrochem. 65 (1961) 581

[14] E.Brosh, A.Kiv, J. Nucl. Mater. 306 (2002) 173

[15] F.-P. Ludwig, J. Schmelzer, Z. Phys. Chem. 192 (1995) 155

[16] R. Espiau de Lamaëstre, H. Bernas, Phys. Rev. B 73 (2006) 125317

[17] V. Ramaswamy, T.E. Haynes, C.W. White, W.J. Roorda, M.J. Aziz, Nano Letters, 5 (2005) 373

[18] In: R.W. Balluffi, S.M. Allen, W.C. Carter, Kinetics of materials, Ed. J. Wiley (2005)

[19] G. De Marchi, G. Mattei, P. Mazzoldi, C. Sada, A. Miotello, J. Appl. Phys. 92 (2002) 4249

[20] P. Kluth, B. Johannessen, V. Giraud, A. Cheng, C.J. Glover, G. de M. Azevedo, M.C. Ridgway, Appl. Phys. Lett. 85 (2004) 3561

[21] P. Kluth, B. Johannessen, D.J. Cookson, G.J. Foran, M.C. Ridgway, Nucl. Inst. Meth. B. 246 (2006) 30

[22] A. Balarena, E. Bernieri, P. Picozzi, A. Reale, S. Santucci, E. Burattini, S. Mobilio, Surf. Sci. 156 (1985) 156

[23] Ph. Buffat, J-P. Borel, Phys. Rev. A 13 (1976) 2287

[24] M. Strobel, Ph.D Thesis, FZR, Dresden (1999)

[25] K.H. Heinig, T.Müller, B.Schmidt, M.Strobel, W.Möller, Appl. Phys. A 77 (2003) 17

[26] R.A. Enrique, P. Bellon Phys. Rev. B 63 (2001) 134111

[27] J.-W. Liu, P. Bellon, Phys. Rev. B 66 (2002) 20303(R)

[28] M. Nastasi, J.W. Mayer, J.K. Hirvonen (Eds.), Ion-solids interactions fundamentals and applications, Cambridge University Press, Cambridge, UK, 1996.

[29] H. Hosono, N. Matsunami, Nucl. Instr. Meth. B **141**, 566 (1998)

[30] J.C. Pivin, G. Rizza, F. Garrido, L. Thomé, Europhys. Lett. 39 (1997) 623

[31] G.C.Rizza, M.Strobel, K.H.Heinig, H.Bernas, Nucl. Instr. Meth. B 178 (2001) 78

[32] G. Martin, Phys. Rev. B 30 (1984) 1424

Chapter 7

Direct and Inverse Ostwald ripening under irradiation

Abstract

A model system composed of chemically synthesized 4nm gold nanoparticles confined between two silica layers is used to investigate the behavior of a second phase under irradiation. Samples have been irradiated with 4MeV Au ions for temperatures ranging from 30° up to 800 °C for fluences up to $8x10^{16}$ cm^{-2}. First, we determine the evolution with fluence and temperature of the NP size, density and size distribution. These results have been compared to the predictions of the Heinig-Strobel model. Qualitatively, this model correctly describes the behavior of the NPs under irradiation. Furthermore, we experimentally estimate the evolution with the temperature of the capillarity length, the ion-driven diffusivity and the steady-state concentration for both planar and curved interfaces. Injecting all these parameters into the Heinig-Strobel model, we obtain the size-dependent steady-state concentration for the irradiated NPs. Finally, we redefine the concept of inverse Ostwald ripening showing that, depending on the steady state size, NPs can either to grow or to be dissolved.

7.1 Introduction

Ion beam synthesis (IBS) and ion beam processing (IBP) have proved to be suitable methods for obtaining materials based on NPs and to tune their physico-chemical properties. The irradiation of embedded NPs by energetic ions leads to both the continuous displacement of atoms from the NP toward and the creation of defects within the confining matrix. These elementary processes allow the system exploring novel experimental configurations that are far off-equilibrium. However, whenever the temperature is sufficiently high, the ballistic effects start to compete with thermally activated ones, which tends to restore the system into the equilibrium configuration. The outcome of this competition depends on both the irradiation and the thermodynamic parameters. However, a general understanding of the behavior of nanostructures under irradiation is still lacking. In this regard, one longstanding and intriguing problem concerns the possibility of using ion-irradiation to inverse the thermodynamic stability of an ensemble of NPs. In other words, if under thermodynamic conditions, larger particles grow at the expense of the smaller ones (Ostwald ripening-OR), under irradiation, smaller NPs may become more stable than the larger ones. This process is called inverse Ostwald ripening (IOR).

The first experimental observation of the IOR process dates from early seventeens and is due to Nelson, Hudson and Mazey, [1], who reported the dissolution and stabilization of Ni_3Al precipitates in Ni-Al alloy irradiated at 550°C with 100keV Ni ions. Besides, Jones et al., [2], reported that large ThO_2 precipitates in Ni became decorated by a halo of small thoria precipitates after Ni irradiation. More recently, Rizza et al., [3, 4], reported similar precipitates refinement at the surrounding of Au and Ag NPs within a silica matrix. Mazzoldi et al. , [5], obtained equivalent results for metallic alloy, e.g. CuAu and AuAg. All these results show that under irradiation the equilibrium conditions can be reversed.

Several models have been developed to describe the effect of ballistic mixing on the stability of a precipitate phase. They can be classified according to two main categories:

• The first category is associated with the so called *unidirectional ballistic mixing*. Here, the mixing is restricted to the displacement of solute atoms from the precipitates to the matrix. The first *unidirectional ballistic mixing* model was introduced by Nelson et al., [1], to interpret the behavior of the Ni_3Al precipitates irradiated in Ni-Al alloys . This model is also called precipitate dissolution or NHM model. The model describes the scattering of atoms out of a precipitate particle by irradiation. The solute removed from the precipitate is then assumed to be uniformly distributed to give a supersaturated matrix and uses the theory of precipitate growth from supersaturated solution. The model predicts the existence of a steady state size for irradiated precipitates. This depends on either the competition be-

tween the dissolution rate, due to the ballistic mixing and ion flux, and the growth rate, due to the thermally activated diffusion. However, the model does not include neither nucleation nor coarsening effects. A major improvement of the NHM is due to Frost and Russell, [6, 7, 8]. They introduced a diffusion equation with a ballistic source term, where the coarsening effects are included into the boundaries conditions. Moreover, they formulate the concept of critical flux, to describe the transition from classical-to-inverse Ostwald ripening. It worth mentioning the the term "*inverse coarsening*" or "*inverse Ostwald ripening*" was first used by Russell,[9]. Recently, Heinig and Strobel further improved these earlier works using a better description of the source term by choosing an exponential distribution of relocation distance, [10]. These authors propose to use the capillarity length as physical parameter to rationalize the inverse coarsening.

• More general models include full account of forced mixing. Here, ballistic intermixing is taken into account. In other words, the transport of solute atoms is explicitly calculated not only from the precipitate to the matrix, but also from the matrix toward the precipitate. Following this approach, Martin first described the competition between the ballistic mixing and the thermally activated diffusion introducing the concept of effective temperature, [11]. The latter, related to the irradiation flux, can be understood considering that under irradiation at a temperature T a system reaches a steady state equivalent to that it would have reached at a higher effective temperature. Similar to the model of Frost et al., the Martin's model predicts the existence of a critical flux. In particular, above this threshold flux the dissolution of the precipitates must occur. Further development is due to Enrique and Bellon, [12, 13], and is based on a phase field-type description belonging to the class of diffuse interface models. The authors obtain a dynamical equilibrium phase diagram for a binary alloy. This is separated in three domains: i) a macroscopic phase separation that describes a classical coarsening, ii) a patterning phase to illustrate an inverse coarsening and iii) a solid solution phase to take account of the dissolution effects. In addition, they found a critical flux, consistent with the previous predictions of Frost and Martin.

In principle models including full account of forced mixing do better describe the evolution of a system under irradiation. However, in Chapter 6 we have estimated the gold supersaturation within the silica matrix ($5\text{x}10^{20}$ cm^{-3}) being much lower than the concentration of gold into the NP, ($5.9\text{x}10^{22}$ cm^{-3}). Thus, in first approximation, the contribution of solute diffusing from the matrix toward the NP can be neglected. This allows us to focus on the unidirectional mixing models and in particular on the Heinig-Strobel model. The reason for our choice relies on the fact that this model gives an analytical expression for the solubility of a NP under irradiation allowing, at the same time, the experimental determination of all its parameters.

The aim of this chapter is to use our model system to give an experimen-

tal insight into the mechanisms of direct and inverse Ostwald ripening under irradiation. This chapter is structured as follows: first we experimentally investigate the evolution under irradiation and temperature of 4nm Au NPs. Afterwards, we introduce the Heinig's model and we compare our experimental results with the predictions of the model. The steady-state solubility with NP size, as given by the Heinig's model, is then experimentally determined. Finally, these results are used to interpret our experimental observation for both 4nm and 15 nm Au NPs.

7.2 Experimental

For this study 4nm Au NPs, are considered. The protocol for NPs synthesis and confinement within the silica matrix has been given in Chapter 2. The total thickness of the silica layer is 600nm and the NPs are confined within a unique plane 300nm below the sample surface.

Samples containing 4nm NPs size were irradiated with 4 MeV Au ions for temperature ranging from 30 to 800°C. The ion flux was kept constant at $1\mu A.cm^{-2}$.

7.3 Results

7.3.1 Evolution under irradiation of 4nm Au NPs

First, we analyze how the size of the NPs evolves with fluence for increasing irradiation temperatures. Afterward, for the maximum irradiation fluence, we investigate the evolution with the temperature of both the size distribution profile (SDP) and the density of the NPs.

NP size distribution with fluence at increasing temperatures

Figure 7.1a shows the as-prepared sample. It is composed of spherical and well dispersed Au NPs. The corresponding SDP (figure 7.1e) is asymmetric with a small tail toward the larger sizes. The NP mean size is estimated to be 3.6nm and the standard deviation 1.2nm. Here, the dotted vertical line defines the mean NP size of the unirradiated NP.

Figures 7.1(b-d) show the planar TEM micrographs as well as the SPD corresponding to the maximum irradiation fluence of figure 7.2, i.e. $8 \times 10^{16} cm^{-2}$, at different irradiation temperatures, i.e. 30, 650 and 800°C.

Irradiation at room temperature, figure 7.1b, results in a reduction of the dimension of the NPs. At the same time, 7.1f, the SDP becomes i) symmetric and nearly Gaussian, ii) narrower and iii) shifted toward the smaller sizes. The mean NP size and size dispersion are 2nm and 0.4 nm, respectively.

Figure 7.1c shows sample irradiated at 650°C. The size of the NPs is only slightly modified by the irradiation, i.e. 3.4±1.0nm. Considering the SDP

(figure 7.1g), the SDP is not shifted with respect to the unirradiated one, but its profile becomes more symmetric (gaussian).

Finally, figure 7.1d shows sample irradiated at 800°C. The corresponding SDP is shifted toward larger sizes, whereas a tail is visible toward the smaller sizes. This corresponds to the disappearing of 1-2nm NPs and the growth of larger NPs (5-7nm). Thus, the average NP size is increased to 4.6nm and the size dispersion is 0.8nm.

NP size with fluence at increasing temperatures

Figure 7.2 shows the evolution with fluence of 4nm NPs for temperature ranging from of 30 up to 800°C. Here the curves are only to guide the eye. At room temperature (open diamonds) the NP size rapidly decreases toward a steady state value of 2nm, which is reached at a fluence of about $3.8 \times 10^{16} cm^{-2}$. At the same time, the size dispersion is significantly reduced as compared to the unirradiaed sample. At 650°C (grey squares), both the size and the dispersion of the NPs do not change appreciably with fluence. Finally, at 800°C (full circles) the evolution of the system is reversed. Here, we observe the growth of the NPs toward a steady-state size of about 4.6nm which is reached for fluences larger than $5 \times 10^{16} cm^{-2}$.

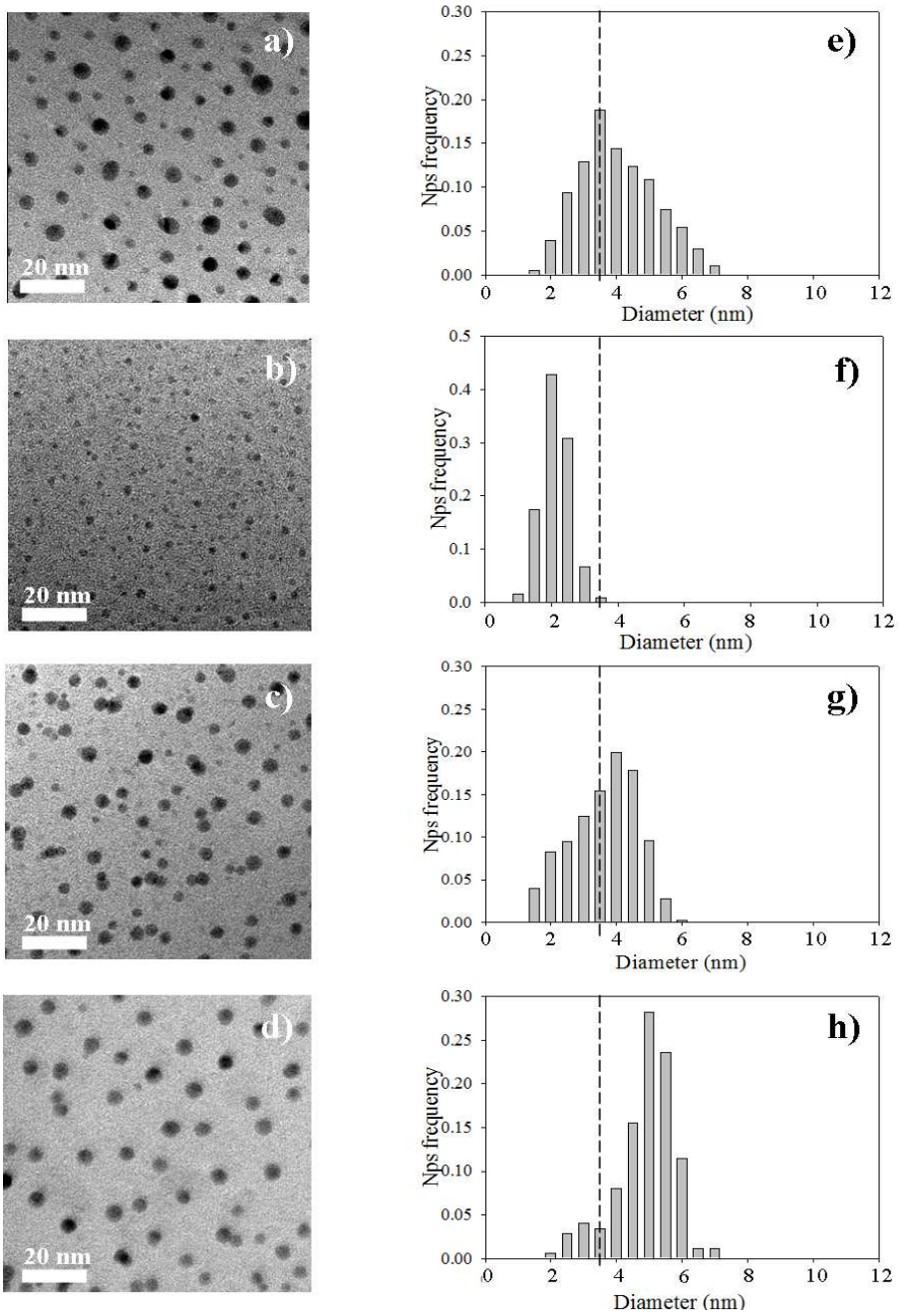

Figure 7.1: a)-d) Planar TEM micrographs of 3.6nm Au NPs: a) unirradiated, b-d) irradiated at $8\times10^{16}cm^{-2}$ at b) T= 30°C, c) T=650°C,and d) T=800°C. The corresponding size distribution functions are given in e-h)

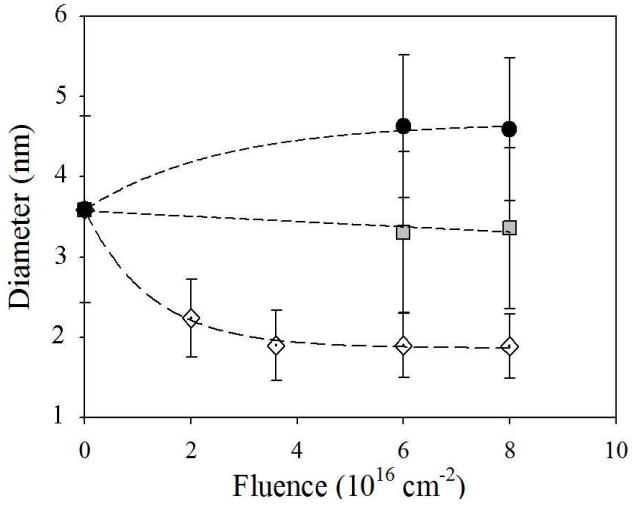

Figure 7.2: Kinetic evolution of 3.6 nm Au NPs irradiated with 4MeV Au ions up to a fluence of $8 \times 10^{16} cm^{-2}$. Irradiation temperatures are T= 30°C (open diamonds) , T=650°C (gray squares), and T=800°C (full circles), respectively.

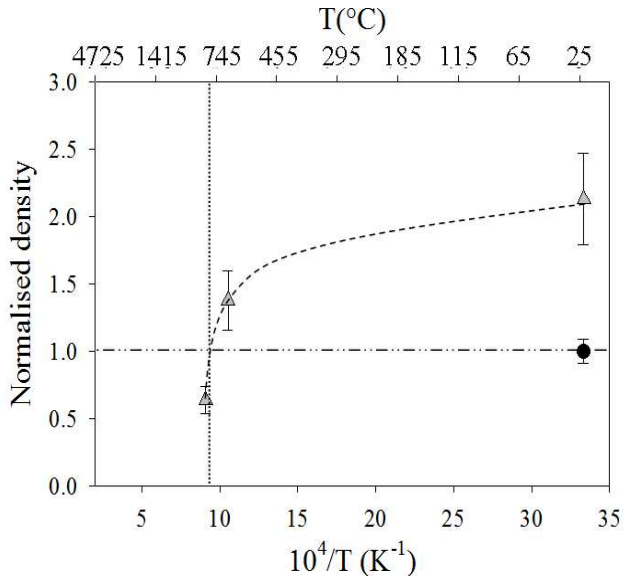

Figure 7.3: Evolution of the normalized NPs density with temperature. Unirradiated sample (black circle and horizontal dotted line). Irradiated NPs at fluence of $8 \times 10^{16} cm^{-2}$ *(Gray triangle)*

NP density with irradiation temperature

Figure 7.3 shows the evolution of the density of the NPs with temperature at a fluence of $8 \times 10^{16} cm^{-2}$. This quantity has been normalized to density corresponding to the unirradiated sample, i.e $7.5 \times 10^{3} \mu m^{-2}$, i.e. the full circle and the dash dotted line. For the sample irradiated at room temperature the density is about two times larger that than measured for the unirradiated sample. Thus, the system evolves under a nucleation and growth regime. When the temperature is raised to 650°C, the normalized density is reduced to 1.4. Finally, at 800°C, the density is further reduced and is now less than one, e.g. 0.7. This corresponds to the fact that the system is driven by a coarsening mechanism. The transition from the precipitation to the coarsening regime is found at about 760°C.

7.4 Discussion

7.4.1 Theory

In this section, we briefly introduce the theoretical elements describing the evolution of an ensemble of NPs under both thermodynamic and ion-driven conditions.

Equilibrium concentration for a planar interface, C_∞ and for spherical NPs, $C^{GT}(R_s)$

From a thermodynamical point of view, the equilibrium concentration at a planar interface A/B is given by the equilibrium between the chemical potentials of the two elements, μ(A)=μ(B), and writes:

$$C_\infty(T) = Exp\left(\frac{\Delta S}{R}\right) Exp\left(-\frac{\Delta H}{RT}\right) \tag{7.1}$$

where ΔS is the entropy, ΔH the enthalpy and R the gaz constant. However, a curved interface, e.g. a spherical NP, generates a stress, σ. The latter modifies the equilibrium conditions between the two phases and is accounted by the Gibbs-Thomson (GT) equation. In its linearized form it writes:

$$C^{GT}(R_s) = C_\infty\left(1 + \frac{R_c}{R_s}\right) \tag{7.2}$$

where C_∞ is the the equilibrium concentration at a planar interface, R_s the NP radius and R_c=$2\sigma V_a / k_B T$ the capillarity length.

The evolution of an ensemble of NPs in a low supersaturation regime is schematically illustrated in figure 7.4. The equilibrium concentration for NPs of different sizes, i.e. the GT equation, is represented by black bars. The GT equation points up that larger NPs have a lower concentration that

smaller ones. Thus, in the figure, the larger the NP, the smaller the height of the bar and the larger its width. Whenever the diffusion is allowed, i.e. at high temperature, a net flux of matter occurs from the smaller toward the larger NPs. This results in the dissolution of the former and a growth of the latter. This phenomenon is known as Ostwald ripening process.

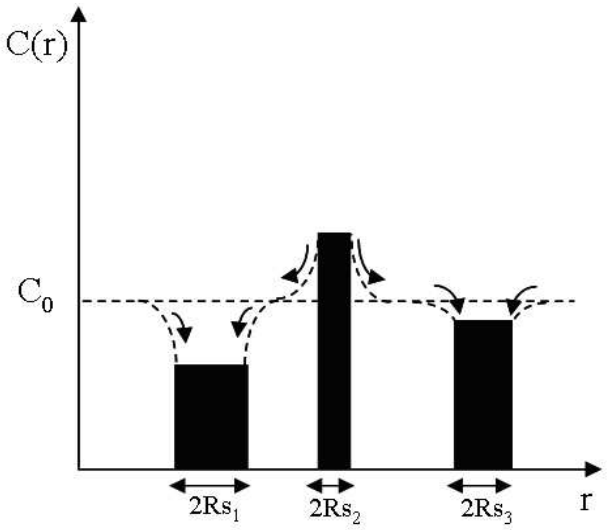

Figure 7.4: Classical Ostwald ripening under thermodynamic conditions. Smaller NPs have a higher equilibrium concentration than the larger ones. The system evolves toward the growth of the larger NPs at the expense of the smaller ones.

Steady-state concentration under irradiation: the Heinig's model

Under thermodynamic conditions, the equilibrium concentration at the interface of a NP is given by the equilibrium between the thermal attachments and detachments. However, whenever irradiation is considered ballistic effects, i.e. the displacement cascades, broke this equilibrium by introducing a new term. As the atoms of the NP are preferentially displaced toward the host matrix, the ballistic term is directionally biased. In other words, if thermal contributions drive the system to toward a thermodynamic equilibrium state, the ballistic term allows the system to explore novels, far off equilibrium configurations.

In the following we will describe the behavior of a NP under irradiation using the Heinig-Strobel model. The model considers that the spatial probability distribution of atomic displacements caused by a collision cascade, $f(\rho)$, is isotropic and exponentially decreasing:

$$f(\rho) = Exp\left(-\frac{\rho}{\lambda}\right) \tag{7.3}$$

ρ is the distance of a displaced atom from its initial position and λ is the characteristic displacement length.

The spatial probability distribution of the atoms displaced into the host matrix, $W_{R_s}(\delta)$, is obtained by integrating $f(\rho)$ for all the atomic positions within the NP:

$$W_{R_s}(\delta) = \frac{q \cdot \lambda \cdot Exp\left(-(\delta + R_s)/\lambda\right)}{2(\delta + R_s)} \times \begin{pmatrix} ((\delta + R_s) \cdot R_s/\lambda^2 + 3 \cdot R_s/\lambda) \cdot cosh(R_s/\lambda) \\ -(R_s^2/\lambda^2 + R_s/\lambda + 3) \cdot sinh(R_s/\lambda) \end{pmatrix} \tag{7.4}$$

$\delta = r - R_s$ is the radial distance from the NP surface. q is the mixing rate and has the dimension of recoil per incident ion per nm.

The importance of $W_{R_s}(\delta)$ relies on that it can be used as a source term to resolve a diffusion equation:

$$D \cdot \frac{1}{r^2}\frac{\partial}{\partial r}\left(r^2 \frac{\partial}{\partial r} C(r)\right) = -\varphi \cdot W_{R_s}(r - R_s) \tag{7.5}$$

where the following boundary conditions are used:

•mass conservation

$$\lim_{r \to \infty} 4\pi r^2 \nabla C(r) = 0 \tag{7.6}$$

•Gibbs-Thomson relation at the interface

$$C(r = R_s) = C^{GT}(R_s) \tag{7.7}$$

The solution of equation (7.5) allows to obtain the steady-state concentration for a NP of size R_s. In its linearized approximation it writes:

$$C^I(R_s) = C^I_\infty \left(1 + \frac{R^I_C}{R_S}\right) \tag{7.8}$$

With

$$\Delta = q\varphi\lambda^2/D^I C_\infty \tag{7.9}$$

$$C^I_\infty = C_\infty.(1 + \Delta) \tag{7.10}$$

$$R^I_C = (R_c - 5\lambda\Delta/4)/(1 + \Delta) \tag{7.11}$$

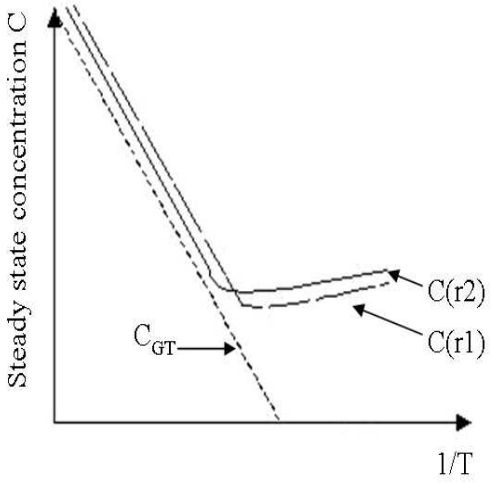

Figure 7.5: Full and long dashes curves represent the solubility under irradiation for precipitates of radius r_1 and r_2 ($r_1 < r_2$). At low temperature, the ballistic contribution modifies the solubility conditions. The short dashed line gives the thermodynamic solubility for a flat interface, e.g. the Arrhenius plot. From [10]

In equation (7.5) the ballistic terms are included into the parameter Δ, i.e. equation (7.9) : the mixing rate q, the characteristic length of displacement atoms λ, the flux of irradiation ions φ, the diffusion coefficient under irradiation, D^I(T), and the equilibrium concentration at a flat interface, C_∞. Δ depends on the temperature through both $D^I(T)$ and $C_\infty(T)$. Thus, $D^I \cdot C_\infty$ can be used to discriminate between two extreme regimes:

i) at high temperature, $D^I \cdot C_\infty \gg 1$ and $\Delta \ll 1$. The consequence is that $C^I(R_s)$ approaches the thermodynamic value, i.e. the Gibbs-Thomson relationship, $C^I(R_s) \rightarrow C^{GT}(R_s)$

ii) at low temperature, $D^I \cdot C_\infty \ll 1$ and $\Delta \gg 1$. Thus, the steady-state concentration close to a flat interface is much larger that the corresponding equilibrium value, $C^I_\infty \gg C_\infty$ (eq. 7.10). On the other hand, for large values of Δ, the capillarity length may become negative, i.e. $R^I_C < 0$ (eq. 7.11).

The main results of the model is that the steady-state concentration given in equation (7.5) has the same form that the Gibbs-Thomson relation given in equation (7.2). On figure 7.6 black bars represents the equilibrium concentration under irradiation for different NP sizes, $C^I(R_s)$. Contrary to the thermodynamic case, larger NPs have higher equilibrium concentration than the smaller ones. Thus, when diffusion is allowed a net flux of matter occurs from the larger toward the smaller NPs. This results in the partial dissolution of the former ones and the growth of the latter ones. This phenomenon

is known as *inverse Ostwald ripening process.*

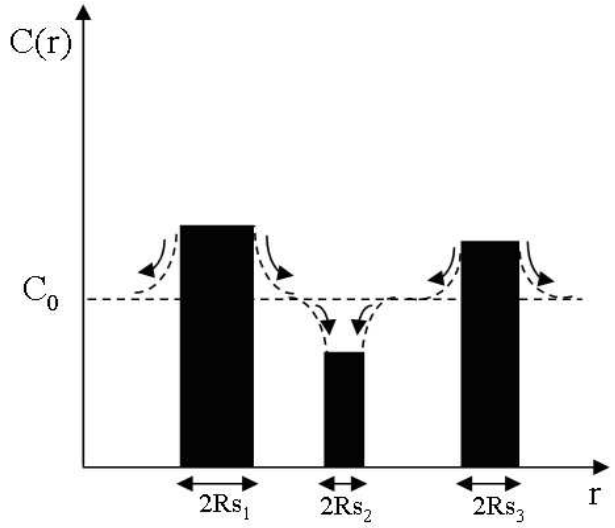

Figure 7.6: Inverse Ostwald ripening under irradiation. Smaller NPs have a steady-state concentration lower than the larger ones. The system evolves toward the dissolution of larger NPs and the growth of the smaller ones.

The Heinig's model defines the critical temperature, T_c, for the classical-to-inverse Oswald ripening transition to be:

$$T_c = \frac{E_a + E^*}{k_B \cdot Ln\left(\frac{C_0 D_0 E^*}{q\varphi\lambda^2 E_a}\right)} \tag{7.12}$$

T_c is defined as the minimum of the steady-state concentration for a flat interface, i.e. T_c=$T\left[MIN(C^I_\infty)\right]$. T_c depends on the diffusion coefficient $D(T) = D_0.exp(-E_a/k_B.T)$ through the pre-exponential factor D_0 and the activation energy E_a. It depends also on the pre-exponential factor, C_0, and the activation energy, E^*, of the steady state concentration at the flat interface, $C_\infty = C_0.exp(-E^*/k_B.T)$. k_B is the Boltzmann constant, and q, φ, λ have the same meaning as previously introduced.

Figure 7.7 shows the evolution of precipitates radius distribution under irradiation as predicted by the Heinig-Strobel model and kinetic Monte-Carlo simulations, [14].

• Far below T_c, precipitation and inverse Ostwald ripening were found and the density of NPs is expected to increase. At the same time the size distribution function must shift toward smaller sizes becoming narrower.

• Below T_c, inverse Ostwald ripening with a conserved number of NPs is predicted. The size distribution is not shifted but becomes narrower.

• Above T_c, conventional Ostwald ripening is predicted. The NP density decreases, whereas the size distribution function shifts toward larger size

becoming broader and approaching the classical LSW distribution, [15, 16]

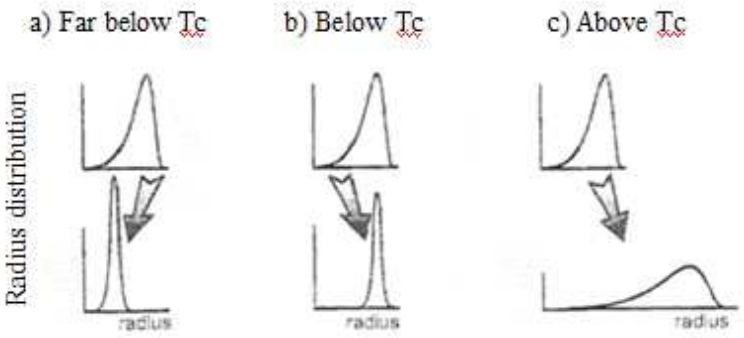

Figure 7.7: Evolution of the size distribution under irradiation. Above the initial size distribution. Below the prediction of the model for different irradiation temperatures: a) far below Tc b) below Tc , c) above Tc. From [10].

7.4.2 Qualitative comparison between our experimental results and the prediction of the Heinig-Strobel model

In this section the prediction of the Heinig-Strobel model are compared to our experimental results. All the results have been summarized in table 7.1.

i) irradiations at T=30°C. The SDP is shifted toward smaller sizes becoming narrower (figure 7.1) and the nucleation of new precipitates is observed (figure 7.3). This behavior corresponds to the predictions of the Heinig-Strobel model for the IOR regime far below T_c.

ii) irradiations at T=650°C. Although the nucleation of new precipitates is observed. However, the normalized density is reduced to 1.4 and the SDP is not shifted by the irradiation. This behavior is close to the inverse Ostwald ripening regime with a conserved number of NPs predicted by the Hening-Strobel model.

iii) irradiations at T=800°C. the SDP is shifted toward larger sizes becoming broader. At the same time, a reduction of NP density is observed. This behavior corresponds to the evolution the NPs in a classical OR regime, as predicted by the Heinig-Strobel model above T_c.

7.4.3 Experimental estimation of the steady-state concentration of a NP under irradiation

In previous section we have introduced the Heinig-Strobel model and we have shown that it qualitatively agrees with our experimental results. Here, we use the analytical expression for the steady-state concentration, $C^I(R_s)$,

Table 7.1: Experimental estimation for NPs density, size and size distribution. These results have been compared to the predictions of the Heinig's model.

	NP density		NPs size (displacement toward)		NPs size distribution	
	Theory	Exp.	Theory	Exp.	Theory	Exp.
$T \ll T_c$	increase	increase	smaller sizes	smaller sizes	narrower	narrower
$T \sim T_c$	constant	constant	no	no	narrower	stable
$T \gg T_c$	decrease	decrease	larger sizes	larger sizes	broader	broader

to quantitatively describe the stability of a second phase under irradiation. First, each parameter contained in equations (7.9), (7.10), (7.11) is experimentally estimated then reinjected into equation (7.8).

Δ parameter

The parameter Δ, eq.(7.9), contains all the irradiation on terms and writes:

$$\Delta = q\varphi\lambda^2/D^I C_\infty \tag{7.13}$$

Ion flux φ

All our experiments have been performed with a constant ion flux of φ=1μA.cm^{-2} or 3.12x10^{12} ions.cm^{-2}.s^{-1}.

Mixing rate, q, and characteristic displacement length, λ

These two parameters, q and λ, can be determined by having recurse to the SRIM simulation. As we cannot simulate spherical structures, we consider a multilayer system composed of a thin Au layer sandwiched between two silica layers. The thickness of the Au layer is taken to be 3.6nm corresponding to the average size of NPs, whereas the thickness of both silica layers is 200nm.

For each simulation 4MeV Au ions are used and 10^5 iterations are considered. The result is shown in figure 7.8. Full circles correspond to the implantation profile of Au into SiO_2 , i.e. the number of gold recoils per ion and nm into silica. The parameters q and λ can be estimated by fitting the implantation profile with:

$$W_\infty(\delta) = \frac{q}{2}.(1 + \frac{\delta}{2\lambda}).exp(-\delta/\lambda) \tag{7.14}$$

where δ is the distance from the Au surface. This expression has been derived from equation 7.4 in the limit of infinity sphere, i.e. $R_S \longrightarrow \infty$. The obtained values are reported in table 7.2. We observe that q and λ for

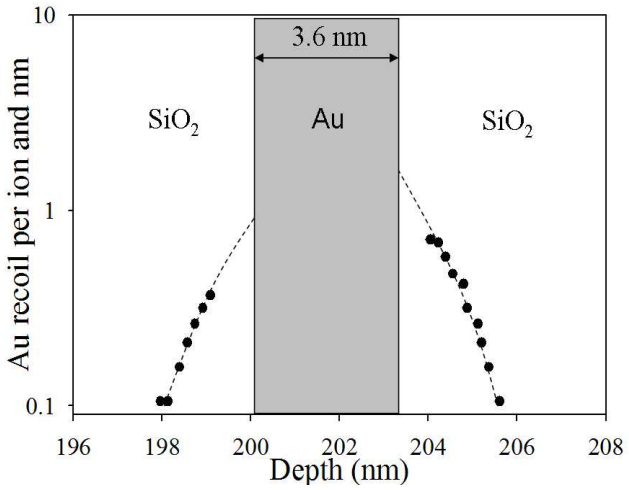

Figure 7.8: SRIM calculation for 4MeV Au irradiation of a 3.6nm Au layer sandwiched between two silica layers (200nm each). Full circles represent the depth profile of Au atoms displaced from the Au layer into the silica matrix. These points have been fitted with equation 7.14 to obtain the q and λ parameters.

the forward displacements are slightly larger than those for backward displacements. This effect is probably due to the anisotropic distribution of cascades during the ion-mixing process, [17]. In the following an average value for both these quantities has been considered, i.e. q=27.5±2.1nm^{-1} and λ=0.7±0.1nm.

Table 7.2: Value of q and λ parameters given by SRIM

Ballistic ejection	q (recoil/ion/nm)	λ (nm)	Depth interface (nm)
Forward (right)	29.6	0.8	203.6
Backward (left)	25.4	0.6	200

Equilibrium concentration for a planar interface, C_∞
The equilibrium concentration for a planar interface, C_∞, writes, [18]:

$$C_\infty = C_0 Exp(-H_{fv}/k_B T) \tag{7.15}$$

H_{fV} is the enthalpy for vacancy formation and its value for gold NPs

embedded within a silica matrix has been estimated by Ruffino and al to be about 1eV.at^{-1}, [19]. The pre-factor C_0 can be considered equal to the bulk density, i.e. C_p=5.9×10^{22}cm^{-3}. The evolution of C_∞ with temperature is given in figure 7.9, full circles.

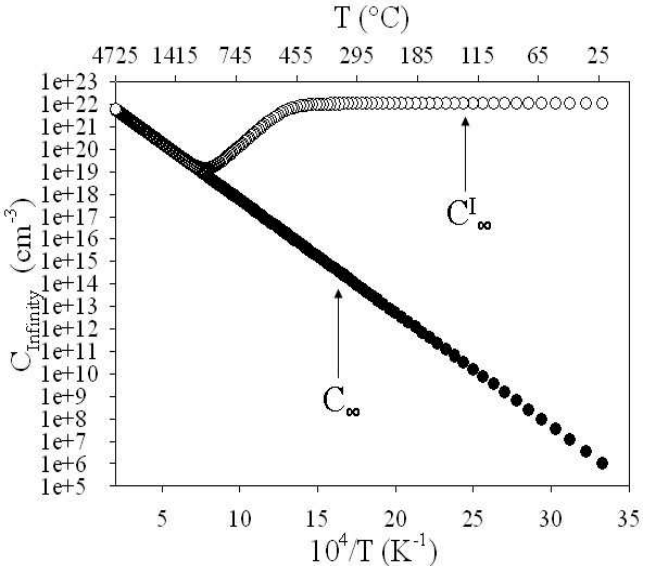

Figure 7.9: Concentration at a flat interface: under thermodynamic conditions, C_∞, (full circles) and under irradiation, C^I_∞, (open circles).

Diffusion coefficient under irradiation, $\mathbf{D^I(T)}$

We have shown in Chapters 3 and 6 that the diffusion coefficient under irradiation can be qualitatively estimated by considering the definition for the diffusivity, D=L^2/4t. The diffusion distance L corresponds to the maximum distance at which satellites were found, L_{max}, and the time t is related to the flunce, t=Φ/φ. The value of L_{max} is measured considering the distance between the plane containing the NP and the farthest visible precipitate toward the Si substrate, figures 7.10(a-b). It worth mentioning that in order to have a solute source at both large irradiation fluences and high temperature 15nm Au NPs are used.

Experimental values are given on figure 7.11, full circles. The thermodynamic diffusivity is also represented, open circles. Thermodynamic diffusivity of gold into silica has been evaluated by several authors. Collins et al, [20], measured the diffusivity of a gold layer on a Si/SiO_2 substrate, annealed between 800 and 1100°C under Ar atmosphere. They found a diffusion coefficient of $D = 1.52 \times 10^{-7} Exp(-2.14/k_B.T) cm^2.s^{-1}$. Similar values have been obtained by Ruffino and al., [21], and by Menke and al., [22].

Experimental data can be fitted using the Radiation Enhanced Diffusion (RED) theory developed by Dienes and Damask, [23]. The Dienes and

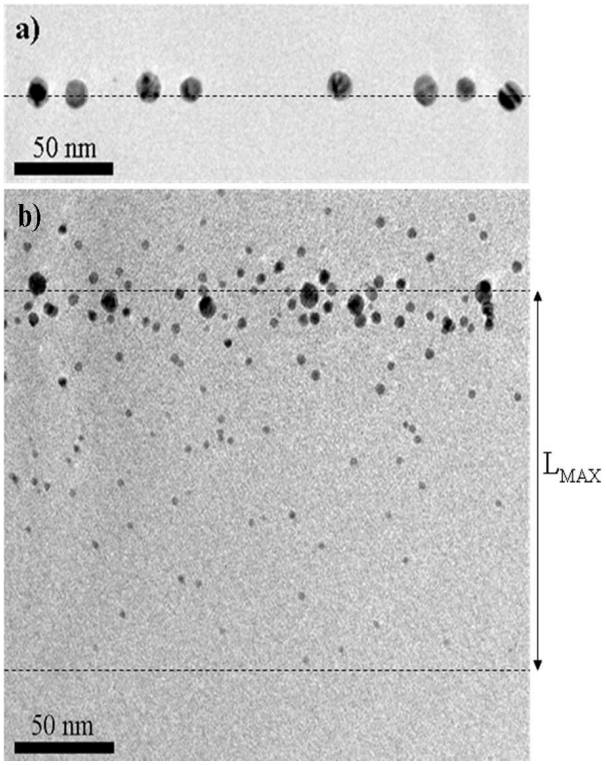

Figure 7.10: Cross-section TEM micrographs of a) unirradiated 15nm Au NPs, and b) irradiated NPs at a fluence of $8 \times 10^{16} cm^{-2}$ and temperature of T=800°C. Dotted line represents the plane containing the NPs and L_{MAX} is the maximum distance at which precipitates are found.

Damask theory predicts the existence of two temperature regimes: i) below a threshold temperature, ballistic displacements drive the diffusion of the solute. In this regime the diffusion coefficient does not depend on the temperature, i.e. D_1^I=Const. ii) above the threshold temperature, defects become mobile and the diffusion coefficient becomes T-dependent, i.e. $D_2^I \sim$Exp(-E_a/k_BT). Experimental data have been fitted using a linear combination of these two diffusion terms:

$$D^I(T) = D_1^I + D_2^I(T) = A + B \cdot Exp(-E_a/k_B T) \tag{7.16}$$

where E_a is the total activation energy for silica defects and A and B are two constants. On figure 7.11 the dotted curve represents the fit of the experimental date with this equation. The best fit gives an activation energy E_a=1.1eV and A=3.8×10^{-16}cm^2.s^{-1} and B=5×10^{-8}cm^2.s^{-1}.

Evolution of the parameter Δ with temperature

The evolution of Δ(T) with temperature is estimated injecting φ, q, λ, D^I(T) and C_∞ into equation 7.9, e.g. $\Delta = q\varphi\lambda^2/DC_\infty$. In figure 7.12a,

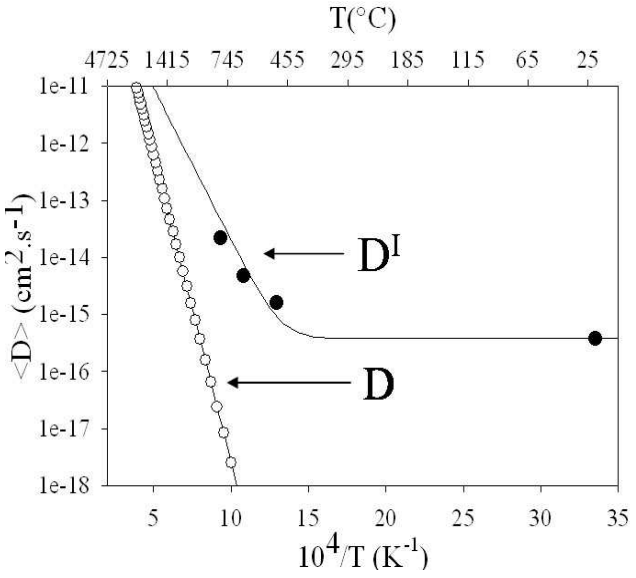

Figure 7.11: Diffusion coefficient of gold into silica under thermodynamic conditions, D(T), (open circles) and under irradiation, $D^I(T)$, (full circles). For the latter the experimental points have been fitted using equation 7.16.

Δ(T) is reported for temperatures ranging from 20 to 5000°C, whereas in figure 7.12b the evolution of Δ(T) is shown for temperatures ranging from 900 to 1800°C. Δ(T) decreases very rapidly and becomes smaller than 1 for temperatures larger than about 1150°C. We will see in the next sections the role played by Δ on both the steady-state concentration for a planar interface, ${C^I}_\infty$, and the capillarity length under irradiation, ${R^I}_c$.

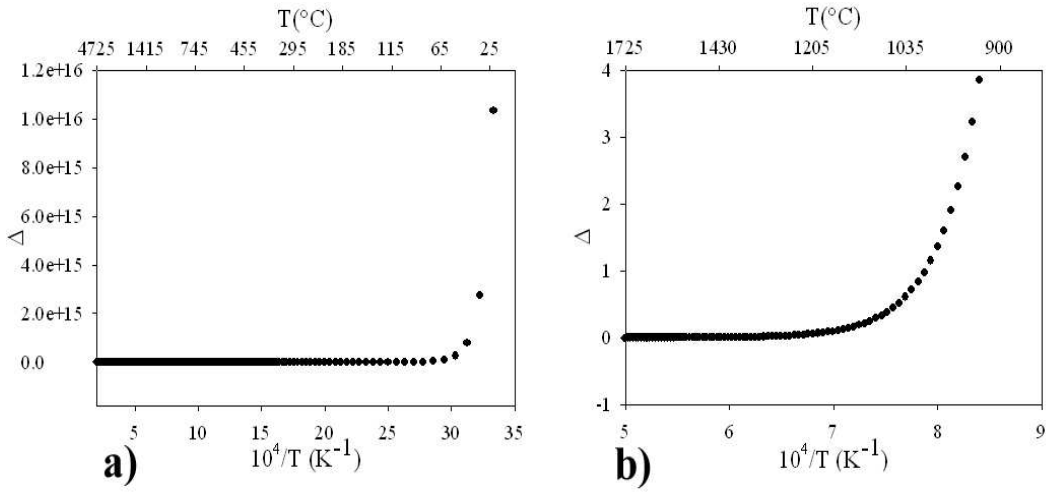

Figure 7.12: a) global evolution with temperature of the ballistic parameter Δ. b)focus on the temperature range 5-9$\times 10^4$/T (K^{-1}).

Steady-state concentration for a planar interface with temperature, C^I_∞

Steady-state concentration with temperature, C^I_∞, can be easily obtained by injecting the value of Δ into equation 7.10. On figure 7.9, full circles represent the equilibrium concentration for a flat interface, C_∞. The corresponding value under irradiation, C^I_∞, is represented on the same figure by the open circles. At low temperatures, e.g. below 500°C, C^I_∞ does not depend on the temperature. It worth mentioning that this temperature is close to the activation temperature for defects in silica, see e.g. Chapter 4. Increasing the temperature up to 1300°C a rapid decreasing of C^I_∞ is observed, until C^I_∞ reaches the thermodynamic value. For larger temperatures, $\Delta \leq 0.2$, the two values evolve in the same way. Thus above about 1300°C the ballistic term becomes negligible and the system is completely driven by the thermodynamic.

Capillarity length R^I_C under irradiation with temperature

The thermodynamic evolution of the capillarity length writes, $R_c = 2\sigma V_a / k_B T$ and is reported in figure 7.13a (full circles). The value for σ and V_a are 4x10^{-4} J.cm^{-2}[24], and 1.6x10^{-23} cm^3 [25], respectively. Capillarity length under irradiation writes $R^I_C = (R_c - 5\lambda\Delta/4)/(1+\Delta)$, equation 7.11. R^I_C depends on the characteristic displacement length, λ, and on the ballistic parameter Δ, which have been previously determined. Its evolution for temperatures ranging from 20 to 5000°C is given in figure 7.13a, open circles. The evolution of R^I_C from 400 to 1800°C is shown in figure 7.13b. From the

inspection of this figure four different regimes can be defined:

i) for irradiation in the range 30-500°C the value of R_c^I is negative and nearly independent on the temperature. Here, ballistic effects dominate, $\lambda\Delta \gg 4/5R_c$ (regime I).

ii) for temperature larger than about 1300°C, the value of R_c^I evolves as the thermodynamic one, R_c. Here, thermal effects dominate, $\lambda\Delta \ll 4/5R_c$ (regime IV).

iii) in the intermediate regime, 800-1700°C, R_c^I becomes T-dependent and increases toward its thermodynamic value, R_c. At a temperature of about 850°C, R_c^I becomes zero. This point corresponds to the equilibrium between the thermal and the ballistic forces. From this threshold temperature, T_c, two sub-regions can be defined. For $T<T_c$, R_c^I is still negative but the thermal contribution is becoming comparable to the ballistic one, i.e. $\lambda\Delta \geq 4/5R_c$ (regime II). On the other hand, for $T>T_c$ the thermal contribution becomes dominating over the ballistic one, i.e. $\lambda\Delta \leq 4/5R_c$ (regime III).

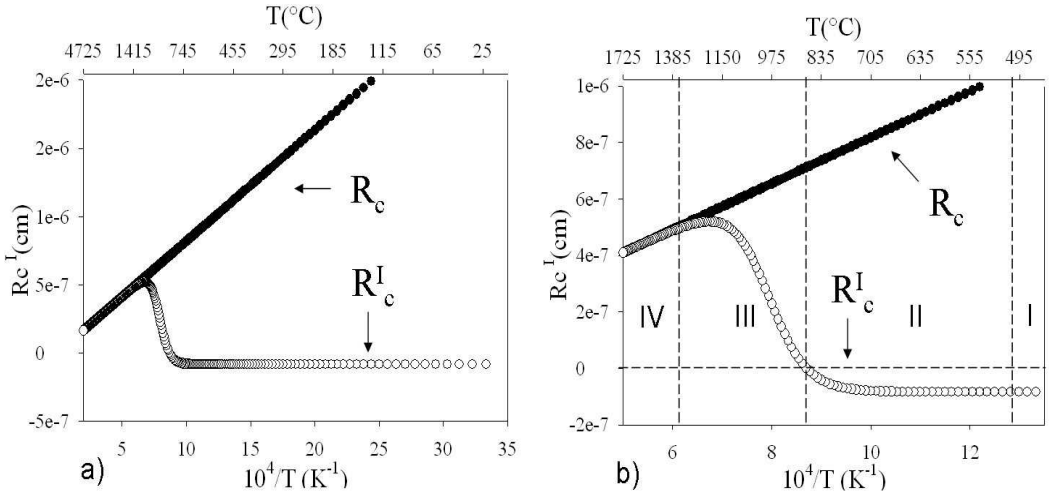

Figure 7.13: a) global evolution of the capillarity length under thermodynamic conditions, R_C, (full circles) and under irradiation, R_C^I, (open circles). b)focus on the temperature range 5-13×10^4/T (K^{-1}) showing the existence of four regimes for R_C^I.

Steady-state concentration for a spherical NP with temperature, $C^I(R_s)$

Finally, using the estimation for both C_∞^I and R_c^I, we obtain the experimental estimation of the ion-driven steady-state concentration for a spherical NP , $C^I(R_s)=C_\infty^I(1+R_c^I/R_s)$. This equation corresponds to the the Gibbs-Thomson relationship under irradiation.

Each gray curve of figure 7.14a represents the evolution with T of $C^I(R_s)$ for a NP of a given radius. In the figure R_s is between 0.85 and 3.5 nm.

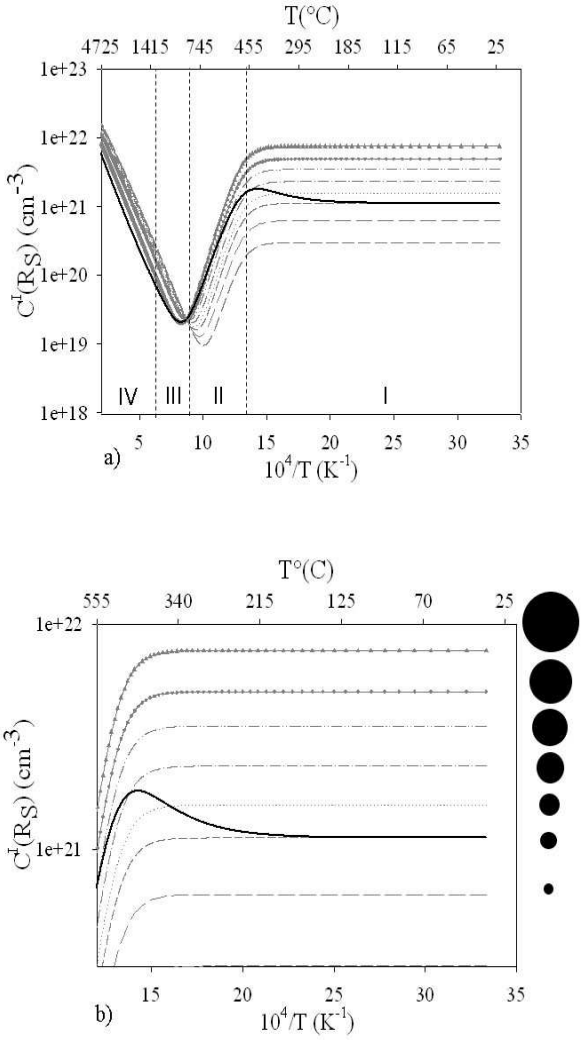

Figure 7.14: a) Temperature dependence of steady-state concentration with NP size, $C^I(R_s)$. Bold curve represents the experimental steady-state solubility. b) focus on the low temperature range, 12-35$\times 10^4$/T (K^{-1}), for $C^I(R_s)$.

Three different regimes can be observed

i) For low temperatures, regime I, the steady state concentration for small NPs is smaller than that for the larger ones, as expected for the IOR regime.

ii) above T=500°C, due to the increasing of thermal effects (regime II), all concentration curves, $C^I(R_s)$, are strongly reduced. They come closer to each other converging toward a unique point. At T_c=840°C, all curves pass through the same point. As previously mentioned, this temperature corresponds to the condition R_c^I=0. At this special temperature all precipitates have the same concentration.

iii) Above 840°C, regime III, an inversion of the value of $C^I(R_s)$ with size is observed. The steady-state concentration for the smaller NPs becomes larger than those of the larger ones, as expected for a classical OR regime.

iv) For temperature larger than about 1300°C, the steady state concentration follow a purely classical thermodynamic behavior(regime IV).

Beyond the Heinig-Strobel model: the steady-state concentration for the equilibrium size under irradiation, $C^I(R_s^{eq})$

Heinig-Strobel model allows to obtain an experimental estimation for the evolution of $C^I(R_s)$ with temperature for all the NP sizes. However, the model cannot be used to estimate the steady-state size, R_s^{eq}, and thus the corresponding steady-state concentration, $C^I(R_s^{eq})$. Nonetheless, the R_s^{eq} and its evolution with T can be experimentally estimated from figure 7.2.

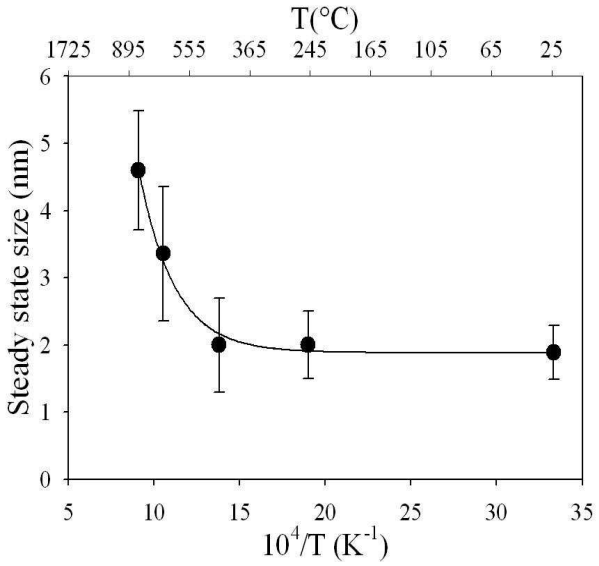

Figure 7.15: Temperature dependence of the steady-state size of pristine 3.6nm Au NPs irradiated with 4MeV Au ions up to a fluence of 8×10^{16}cm^{-2}. Experimental data have been fitted with equation 7.17.

Figure 7.15 shows the evolution of R_s^{eq} with T. Experimental data have been fitted using a two regimes equation similar to that used for the diffusivity, $D^I(T)$:

$$R_s^{eq}(T) = A + B \times \exp\left(-C \times \frac{10^4}{T}\right) \tag{7.17}$$

where A, B, C are three constants. The best fit gives A=0.94 nm, B=111.24 nm, and C=0.48 K

Finally, the steady-state concentration with temperature corresponding to the steady-state size is simply obtained by injecting $R_s^{eq}(T)$ into $C^I(R_s^{eq})=C^I_\infty(1+R^I_c/R^{eq}_s)$, e.g. the bold line in figure 7.14.

7.5 Graphic interpretation of the $C^I(R_s)$ curves

An insight into the evolution of both 4nm NPs (section 7.3.1) and 15nm NPs (chapters 3 and 4) can be obtained using a graphic interpretation of figures 7.14(a-b).

First, in figure 7.14(b), a vertical line is drawn at given irradiation temperature, for example T_1=30°C. This line intersects all the $C^I(R_s)$ curves at T_1. In other words, each intersection point relies the steady-state concentration to a given NP size, R_s. These values are reported in figuref 7.16(a) as grey circles.

Second, for T=T_1, the experimental steady-state concentration, i.e. the bold continuous curve, intercepts *one and only one* of all the gray curves. This point defines the equilibrium size under irradiation at T_1 and is represented as a full square on figure 7.16a.

For the physical interpretation we can refer to figure 7.16(d). As in previous sections, the steady-state concentrations are represented by vertical bars. The grey bar corresponds to the equilibrium size under irradiation, R_s^{eq}. In particular, when $R_s>R_s^{eq}$, we also have that $C^I(R_s)>C^I(R_s^{eq})$. Thus, large NPs will be partially dissolved toward R_s^{eq}. On the other hand, when $R_s<R_s^{eq}$, we have that $C^I(R_s)<C^I(R_s^{eq})$ and small NPs can grow toward R_s^{eq}. This evolution is representative of the IOR regime.

Using the same procedure, we obtain the steady-state concentration, $C^I(R_s)$, at T_2=840°C. T_2 corresponds to the temperature at which all the steady-state curves converge toward a unique value, figure 7.14a. It worth noticing that T_2 is also the temperature where the capillarity length under irradiation becomes zero, i.e. R^I_c=0, figure7.13b. To understand how the ensemble of NPs behaves at T_2, we look at figure 7.16b or at its graphical representation, figure 7.16e. For T=T_2, $C^I(R_s)$=constant whatever the initial NP size and the system is in a stationary state and does not evolve under irradiation.

Finally, we analyze the behavior of the NPs when a high-temperature irradiation is considered, e.g. $T_3>T_2$. The correspondence between the NP size, R_s^{eq}, and the steady-state concentration, $C^I(R_s)$, is given in figure 7.16c. Again, the full square represents the equilibrium size under irradiation for T=T_3. The most important feature here, is that the evolution of C^I has a concave shape, and thus reversed with respect the irradiation at T=T_1, e.g. a convex shape. This change radically modifies the behavior of the NPs during the irradiation. Here, larger NPs have lower equilibrium concentration than the smaller ones. Thus, the system evolve toward the growth of larger NPs

at the expense of the smaller ones. This is the classical Ostwald ripening process (figure 7.16f).

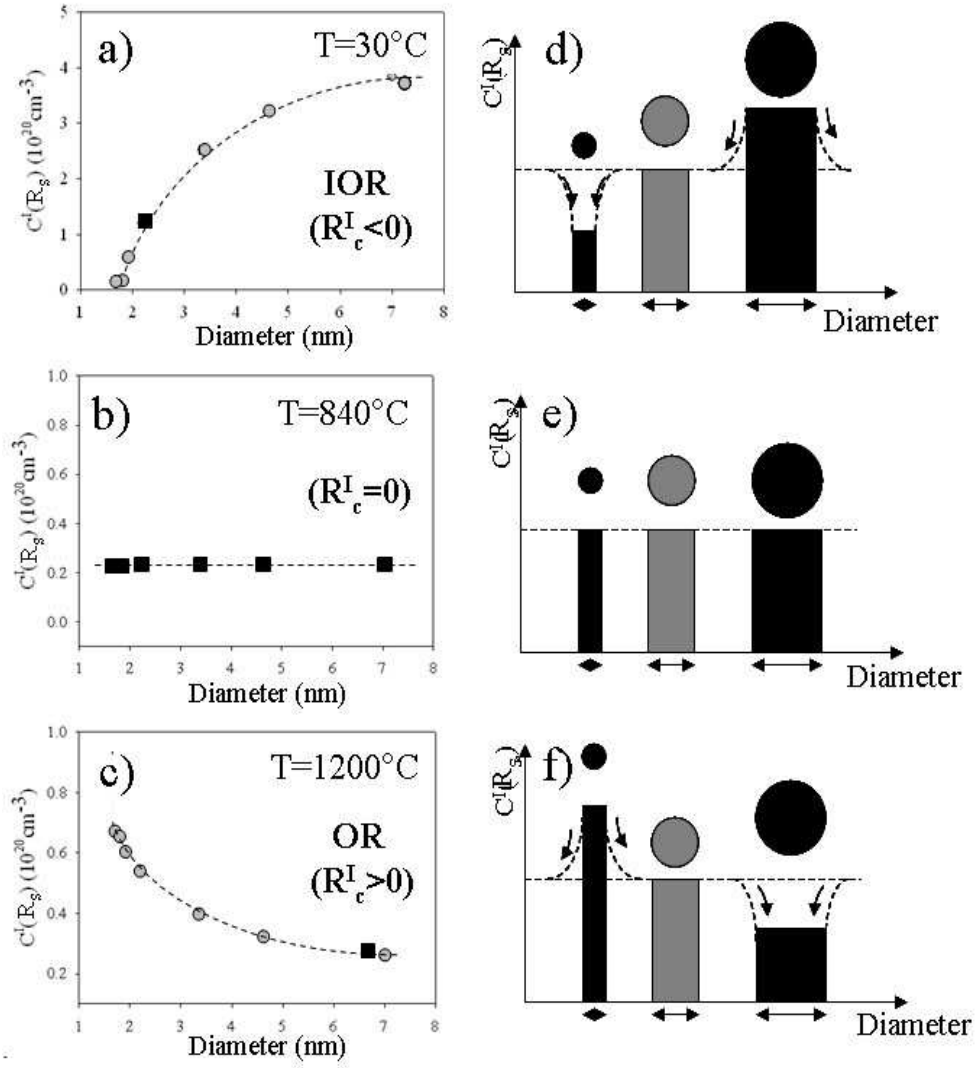

Figure 7.16: Evolution of the steady-state solubility with the NP size for different irradiation temperatures: a) 30°C, b) 840°C, and c) 1200°C. Full squares define the steady-state size at a given temperature. Three regimes are evidenced: a) inverse Ostwald ripening regime, R^I_c<0 , ii) system at the transition temperature Tc, R^I_c=0, and c) classical Ostwald ripening regime, R^I_c>0. Figures d-f) show the corresponding solubility with the NP size.

7.5.1 Interpretation of the experimental results

4nm Au NPs

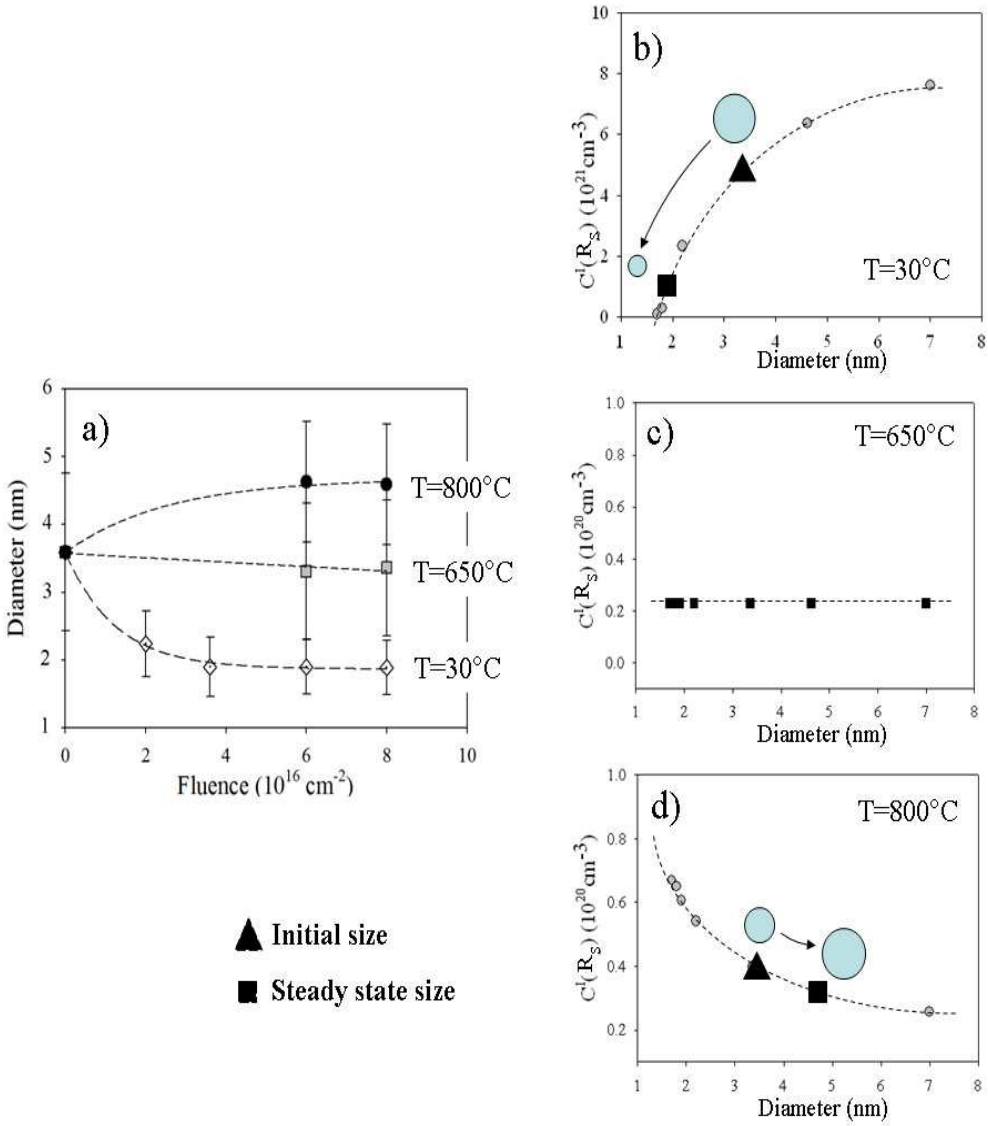

Figure 7.17: a) experimental evolution under irradiation of 3.6nm Au NPs with temperature. b-d) steady-state concentration, $C^I(R)$ with the irradiation temperatures: b) 30°C, c) 650°C, and d) 800°C. Full triangle represents the initial NP size and full square the steady-state size. The evolution of the system is indicated by the arrows.

Figures 7.17(a-d) are used to give an insight into the evolution of 3.7nm Au NPs. The samples have been irradiated with 4MeV Au ions at different temperatures, 30, 650 and 800°C.

i) irradiation at 30°C results in a partial dissolution of the NPs toward 2nm. Figure 7.17b shows that the steady-state size at 30°C is R_s^{eq}=2nm. In this regime, $C^I(4nm)>C^I(R_s^{eq})$. Thus, the energy deposited by the impinging ions allows the system to be driven toward its stationary state.

ii) at 650°C, the NPs do not evolve under irradiation. For this temperature the C^I is nearly independent on the initial NP size, figure 7.17c.

iii) at 800°C, NPs are observed to grow under irradiation. The corresponding steady-state concentration, $C^I(R_s)$, is now reversed and larger NPs becomes more stable than the smaller ones (figure 7.17d).

15nm Au NPs

Figures 7.18(a-c) are used to give an insight into the evolution of 15nm Au NPs. The samples have been irradiated with 4MeV Au ions .

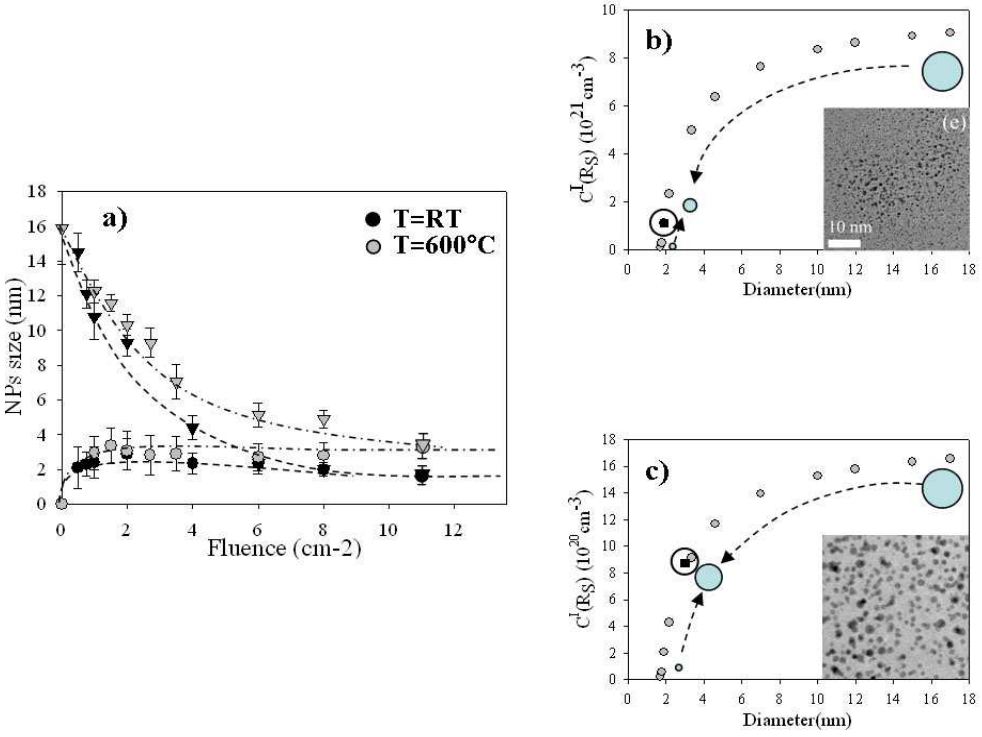

Figure 7.18: a) experimental evolution under irradiation of 15nm Au NPs with fluence at 30°C (black circles) and 600°C (gray circles). In both cases the system evolves toward a steady-state size. However, this size depends on the irradiation temperature. b-c) steady-state concentration, $C^I(R)$ corresponding to the two irradiation temperatures. As the steady-state size at b) 30°C is lower than that at c) 600°C, for the latter NPs can grow toward larger sizes.

We have seen in chapter 4 that irradiation favor the nucleation and

growth of a halo of precipitates around the dissolving central NP. Figure 7.18a) shows the evolution of both these populations at 30 and 600°C. In both cases, the system evolves toward a unique steady-state size. However, this value depends on the irradiation temperature. Figures 7.18(b-c) show the steady-state concentration, $C^I(R_s)$, for these two temperatures. The full square represents the equilibrium size at a given temperature. We can easily observe that the value increases with temperature. On the other hand, for pristine 15nm NPs we have that $C^I(15nm) > C^I(R_s^{eq})$. Thus, they will be partially dissolved by the irradiation. On the other hand, for precipitate clusters, which nucleate around the NP, we have that, at the beginning of the irradiation, $C^I(R) < C^I(R_s^{eq})$. Thus, they can grow toward the steady-state size for which $C^I(R) = C^I(R_s^{eq})$.

7.6 Conclusion

The stability under irradiation of an ensemble of embedded NPs has been studied in detail using a model system. The evolution of the NPs size, density and size distribution have been analyzed for different irradiation temperatures. We show that three regimes can be defined: i) at 30°C, irradiation induces the reduction of the mean NP size, an increase of the NPs density and a narrowing of the size distribution. This corresponds to the IOR regime. ii) at 650°C, irradiation does not modify neither the size nor the size distribution. At the same time, the density of the NPs remains nearly constant. This temperature is close to the critical temperature where ballistic and thermodynamic effects are mutually balanced. iii) at 800°C, irradiation results in a increase of the NPs size and in a broadening of the size distribution function as well as a reduction of the NPs density. This behavior is characteristic of a classic Ostwald ripening process. Our experimental results have been compared to the Heinig-Strobel model. We show that this model correctly describes the IOR process. However, the threshold temperature for the OR-to-IOR transition is not correctly defined and that two new intermediate regimes must be introduced. We experimentally estimate all the parameters contained in the Heinig-Strobel model, i.e. the evolution of the capillarity length with temperature, the diffusivity under irradiation and the steady-state concentration for both planar and curved interfaces. Finally, we redefine the concept of IOR showing that, depending on the steady state size, NPs can either to grow or to be dissolved.

Bibliography

[1] R.S. Nelson, J.A.Hudson, D.J.Mazey, J.Nucl.Mater. 44, 318 (1972)

[2] R.H. Jones, J.Nucl.Mater. 74, 163 (1978)

[3] G. C. Rizza, M. Strobel, K. H. Heinig, and H. Bernas, Nucl. Instrum. Methods Phys. Res. B 178, 78 (2001).

[4] Chapter 3, G. Rizza, H. Cheverry, T. Gacoin, A. Lamasson, S. Henry, J. Appl. Phys. 101 (2007) 01432

[5] P. Mazzoldi, G. Mattei, Rivista de Nuovo Cimento, 28, 1 (2005)

[6] H.J. Frost, K.C. Russell, J.Nucl.Mater. 103-104, 1427 (1981)

[7] H.J. Frost, K.C. Russell, Acta.Metall. 30, 953 (1982)

[8] D.S. Gelles, F.A. Garner, J.Nucl.Mater. 85-86, 689 (1979)

[9] K.C. Russell, Progress in Materials Science 28 (1984) 229

[10] K.H. Heinig, T. Muller, M. Strobel, B. Schmidt, W. Moller, Appl. Phys. A 77 (2003) 17.

[11] G. Martin, Phys.Rev.B 30, 1424 (1984)

[12] R.A. Enrique, P. Bellon, Phys.Rev.Lett 84, 2885 (2000)

[13] R.A. Enrique, P. Bellon, Phys.Rev.B 63, 134111 (2001)

[14] M. Strobel, K.H. Heinig, W. Moller, Mater. Res. Soc. Symp. Proc.647 (2001) 23.

[15] I.M.Lifshitz, V.V Slyozov, J.Phys.Chem.Solids, 19, 35 (1961)

[16] V.C Wagner, Z.Elektrochem 65, 581 (1961)

[17] M. Nastasi, J.W. Mayer, J.K. Hirvonen (Eds.), Ion-solids interactions fundamentals and applications, Cambridge University Press, Cambridge, UK, 1996.

[18] L.Bornstein, Impurities and defects in group IV elements and III-V compounds, vol.III/22b 393 Springer, Berlin 1989

[19] F.Ruffino, M.G Grimaldi, F.Giannazzo, F.Roccaforte, V.Raineri, Nanoscale Res.Lett. 3 454-460 (2008)

[20] D.R Collins, D.K Schroder, C.T Sah, Appl.Phys.letters 8 (12) 323-325 (1966)

[21] F.Ruffino, M.G Grimaldi, C.Bongiorno, F.Giannazzo, F.Roccaforte, V.Raineri, Superlat. and Micros. 44 588-598 (2008)

[22] Y.Menke, M.Ferraris, C.Corbari, J.Fage-Pedersen, J.Non-Cryst. Solids 345&346 366-371 (2004)

[23] G.J Dienes, A.Damask, J.Appl.Phys. 29 (1958) 12

[24] De Marchi, G.Mattei, P.Mazzoldi, C.Sada, A. Miotello, J.Appl.Phys. 92 4249 (2002)

[25] Handbook of Nanostructured Materials and Nanotechnology, edited by F.Gonella and P. Mazzoldi _Academic Press, San Diego, 2000, Vol. 4.

Chapter 8

Summary and Outlook

Several irradiation-based techniques can be used to fabricate nanocomposite materials. These can be divided into three main categories: i) ion-beam direct synthesis, ii) ion-beam indirect synthesis, and iii) ion-beam-modification. Nanocomposites fabricated with these ion-beam related techniques have a number of attractive characteristics. For example, they provide a wide variety of single-element or compound NPs within virtually any solid host matrix. Moreover, they allows to produce high-purity materials with large NPs volume fraction and with accurately determined dopant concentration. Finally, nanocomposite can be ion-driven into novel experimental configurations that are far off-equilibrium.

However, the main and most crucial difficulty in obtaining commercial NPs-based devices is the inability to produce a suitable narrow size and spatial NP distributions. Additional difficulties arise from the damages introduced within the host matrix during the irradiation. Thus, a post-implantation thermal treatment is generally imposed to remove the irradiation-induced defects. The annealing process is also necessary to promote the precipitation of the NPs. However, it results in an enlargement of the final NPs size distribution according to the classical Ostwald ripening process.

The objectives of this thesis are twofold: i) to go further in the description of the behavior of the ion-driven NPs and ii) to overcome the limitations related to the ion-beam techniques providing a guideline methodology to rationalize the synthesis of NPs when ion-beams are used.

In Chapter 2 the fabrication of a model system is described. To give insights into the evolution under irradiation of confined NPs, the precise control over their initial size, depth distribution and concentration is necessary. To satisfy this criterium, a protocol has been developed. Nearly monodisperse chemically-synthesized Au NPs are confined, at a well defined depth, within two silica layers. This is done in several steps: i) a first silica layer is deposited onto a silicon substrate. ii) the silica surface is then

chemically functionalized by an aminosilane group. iii) at the same time, 4nm and 16nm Au NPs are chemically synthesized following the Jana and Turkevich methods, respectively. iv) these NPs are then grafted onto silica surface exploiting the electrostatic interaction between the negative charged citrate, which coats and stabilizes the Au NPs, and the positive charged aminosilane group which recovers the silica surface. The grafting process is simply achieved by immersing the treated sample into the solution containing the Au NPs. The amount of grafted NPs is controlled by the immersion time. v) samples are then recovered by a second silica layer under the same experimental condition as the first one. This allows the Au NPs to be localized within a unique plane at a depth of 320 nm below the sample surface. Finally, in order to stabilize the silica matrix, samples are annealed at 450°C and 900°C for 1h under Ar-H atmosphere.

In Chapter 3 we show that ion irradiation can be used to tune both the size and the size distribution of the embedded NPs. Samples were irradiated with 4MeV Au^{2+} ions at room temperature up to a fluence of $8x10^{16}cm^{-2}$. Irradiation of chemically synthesized 15±2nm Au NPs embedded within a silica matrix promotes the formation of a halo of satellites around the original cluster. We show that the complete dissolution of the NPs results in the formation of a narrow size distribution of small precipitates with a mean size of 2 nm and a standard deviation of 0.4 nm. In addition, we show that the evolution of the NPs can be described as a two steps process: i) in the first regime, i.e for fluences up to $2x10^{16}cm^{-2}$, the original NP acts as infinite source of solute atoms. Nucleation of satellite clusters occurs when the local concentration of solute overcomes the solubility threshold. Their growth is sustained by the dissolution of the pristine NP. ii) In the second regime, the volume of the pristine NP is reduced below a critical value and it cannot sustain any more the growth of the surrounding satellites. Thus whole system, NP plus satellites, evolve toward a unique steady-state size. This regime was interpreted in term of inverse Ostwald ripening mechanism.

In Chapter 4 we widen our investigation by varying both the irradiation temperature and the stopping powers. Samples are irradiated with 4MeV Au ions and 4MeV Br ions for temperature ranging from 30°C up to 800°C and for fluences up to $8x10^{16}$ cm^{-2}. We show that when either the irradiation temperature is increased or the nuclear stopping power decreased, a reduction of the dissolution rate of the embedded NPs is observed. This leads to the formation of a bimodal size distribution, the extend of which can be controlled by varying the temperature, the nuclear stopping power and the irradiation fluence. Besides, the steady-state size of the precipitates is observed to increases with the irradiation temperature. Furthermore, we find a qualitative correlation between the thermal stability of the E' defects and the reduction of the density of the precipitates when the irradiation temperature is above 500°C. Finally, the introduction of several graphs, or schemes, describing the evolution of the size of both NPs and precipitates,

their size dispersion and the size gap has been done with the aim to rationalize the choice of the irradiation condition. The final objective is to enhance the control of the final size distribution of the confined second phase during the ion-beam synthesis.

In Chapter 5, we show that when an initially large NPs size distribution is considered, the study of the grow kinetic of the NPs under irradiation can be problematic. We show that irradiation of NPs with different initial sizes leads to different values of both satellites size and density. In particular, at a fluence of 1.5x10^{16} cm^{-2}, the satellite size linearly scales with the NPs size before to saturate for pristine NPs larger than about 15nm, whereas the density ranges approximately as the inverse of the NPs radius. Moreover, we show that also the shape of the size distribution profile depends on the initial NP size. Thus, to study the kinetic growth of the NPs under irradiation is fundamental to start with the narrowest possible size distribution profile. In this regard, the chemical synthesis of metallic NPs and the following sandwiching between two amorphous layers allows to satisfy this criterium.

In Chapter 6, we use our model system and the results obtained in the previous chapters to investigate the behavior of the NPs under irradiation. In particular, in chapter 3 we have shown that for pristine 15nm NPs, the evolution of the satellites can be described by a two-step process: i) for low irradiation fluences, up to about 2-3x10^{16} cm^{-2}, satellites are observed to grow, directly sustained by the NP dissolution and ii) for fluences higher than about 4 10^{16} cm^{-2}, when the pristine NP is below a critical size, the satellites are partially dissolved by the irradiation. Thus, to describe the satellite kinetics our investigation was limited to the first regime, i.e., for fluences up to 2.2x10^{16} cm^{-2}. We show that the evolution of the precipitate phase under irradiation is successfully described by an Ostwald ripening mechanism in an open system limited by the diffusion. Moreover, we estimate the concentration threshold for nucleation as well as the surface tension and the gold diffusivity in silica under irradiation. To conclude, we estimated the nucleation window. In this respect, further experiments are scheduled to modify this regime in a controlled way by playing both with the irradiation parameters and with the temperature. The final key issue is the optimum control of the nanostructures, when these are synthesized with ion beam-related techniques.

In Chapter 7 direct and inverse Ostwald ripening processes under irradiation are systematically investigated. Samples containing of 4nm Au NPs are irradiated with 4MeV Au ions for fluences up to 8x$10^{16}$$cm^{-2}$ and for temperature ranging between 30°C and 800°C. We observe that the ensemble of NPs evolve toward a steady-state size which increases with temperature. Correspondingly, the size distribution profile (SDP) shows different features depending on the irradiation temperature: i) at room temperature the SDP is nearly symmetric and shifted toward smaller sizes (2nm). ii) At 650°C, the SDP remains close to the initial position and is not modified by the ir-

radiation. Finally at 800°C, the SDP is shifted toward larger sizes, with a log-normal shape toward the smaller sizes. In addition the normalized NPs density was observed to decrease with the temperature. Our experimental results are compared to those of the Heinig-Strobel model. We show that the Heinig-Strobel model correctly describes the IOR process. However, the threshold temperature for the OR-to-IOR transition is not correctly defined and that two new intermediate regimes must be introduced. Moreover, using our model system, all the parameters contained into the Heinig-Strobel model are estimated, i.e. the evolution of the capillarity length with temperature, the diffusivity under irradiation and the steady-state concentration for both planar and curved interfaces. Finally, we redefine the concept of IOR showing that, depending on the steady state size, NPs can either to grow or to be dissolved.

The progress in the control of the properties associated to a nanocomposite basically depends on our understanding on the effects induced by the irradiation onto/into the studied material. We have shown that the possibility to use a model system facilitates the interpretation of the experimental results, allowing, at the same time, to check the existing theoretical models. However, it is impossible to experimentally explore all the reaction pathways. For this reason, we started to examine the dependence of the irradiation parameters on the NPs behavior by means of atomistic computer simulations. In our aim, these simulations will be used with a twofold objective: i) to reproduce the experimental results and ii) to predict the stability of the NPs when the irradiation conditions are changed. Among the different numerical approaches, the Kinetic Monte Carlo (KMC) is the most suitable to simulate the time evolution of the NPs under irradiation. The KMC simulation is a statistical method to describe the spatio-temporal development of a many-particle system in which the particles are positioned on the nodes of a rigid grid. Our simulations are based on an Ising-like model. The key property of the KMC algorithm is the rate at which one process takes place. If the rates are correct, the KMC algorithm gives the correct time scale for the evolution of the simulated system. The key parameter of our simulations is the ratio between i) the thermodynamic and ii) the ballistic jumps. Figure 8.1b-c) show some preliminary results of a NP evolving under irradiation. This simulation qualitatively reproduces our experimental results for the nucleation and growth of satellites precipitates around a pristine NP, 8.1e),f). We are currently working to validate our KMC code. In the next future, our simulations will be coupled to some in-situ experiments, e.g. using a TEM coupled with a beam line.

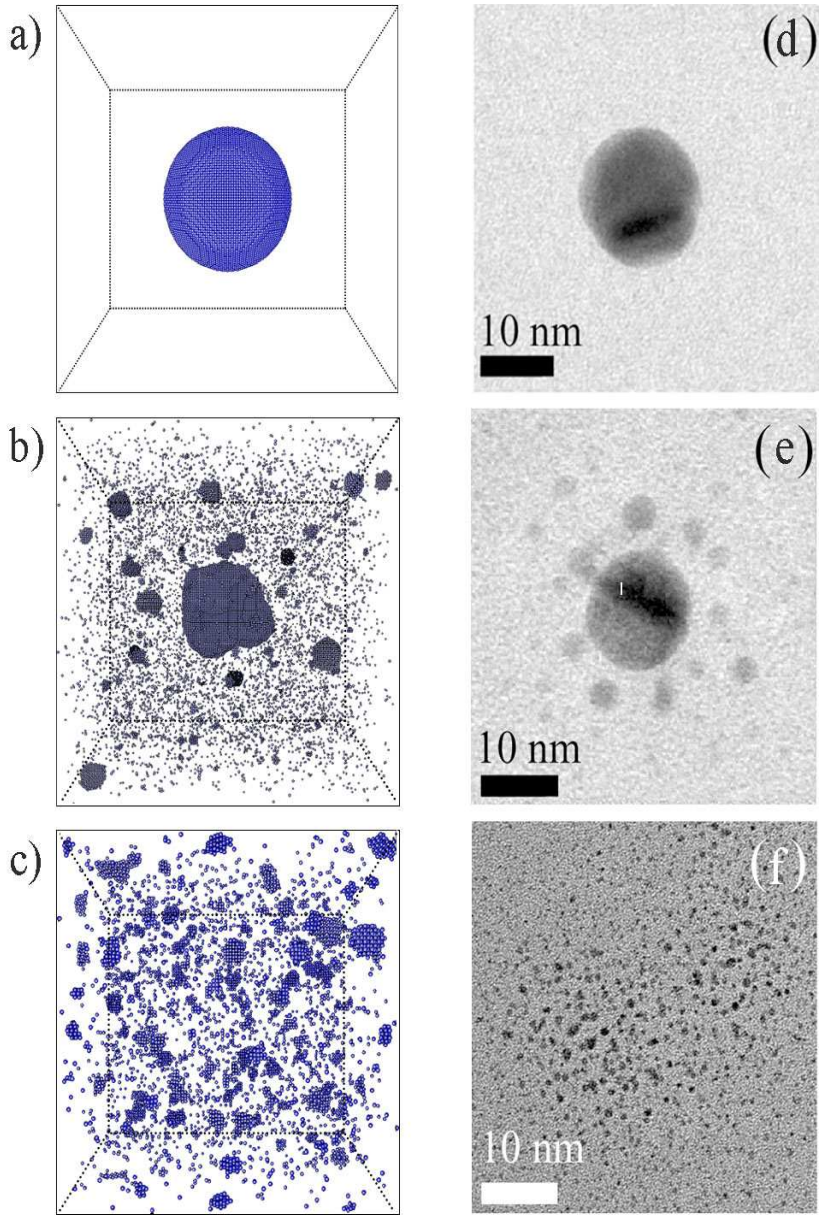

Figure 8.1: Preliminary results of the KMC simulation showing the irradiation-induced satellites nucleation and growth around a pristine spherical NP

Abstract

Nanocomposites fabricated with ion-based techniques have a number of attractive characteristics. However, the main and most crucial difficulty in obtaining commercial NPs-based devices is the inability to produce a suitable narrow size and spatial NP distributions. The objective of this thesis is twofold: i) to go further in the description of the behavior of the ion-driven NPs and ii) to overcome the limitations related to the ion-beam techniques providing a guideline methodology to rationalize the synthesis of NPs when ion-beams are used. Thus, a model system is fabricated. It consists of chemically synthesized metallic nanoparticles sandwiched between two silica layers. We show how the ion irradiation and the temperature can be used to tune the size distribution of the embedded NPs. Moreover, we show that when an initially large NPs size distribution is considered, the study of the growth kinetic of the NPs under irradiation can be problematic. Our model system is than used to investigate in detail the behavior of the NPs under irradiation. We show that the evolution of the precipitate phase under irradiation is successfully described by an Ostwald ripening mechanism in an open system limited by the diffusion. Moreover, the concentration threshold for nucleation as well as the surface tension and the gold diffusivity in silica under irradiation is estimated. Finally, direct and inverse Ostwald ripening processes under irradiation are systematically investigated and the existing theoretical models experimentally checked.

Résumé

Les matériaux nanocomposites fabriqués en ayant recours aux techniques par faisceau d'ions présentent des propriétés très attractives dans les domaines de l'optique, de la photonique et de la plasmonique. Cependant, la difficulté d'obtenir un système avec une distribution de nanoparticules de taille et de distribution spatiale bien contrôlées limite les applications industrielles. L'objectif de cette thèse est double : d'une part, décrire de manière rigoureuse le comportement des nanostructures sous irradiation. D'autre part, rationaliser la synthèse des matériaux nanocomposites en définissant à la fois une méthodologie de travail et en dépassant les limites intrinsèques aux techniques par faisceau d'ions. Pour cela nous avons fabriqué un système modèle composé des nanoparticules métalliques (Au) confinées entre deux couches de silice. Nous montrons comment l'irradiation et la température peuvent être utilisés pour contrôler la distribution en taille des nanoparticules enfouies dans la matrice. En outre, nous montrons que pour étudier la cinétique de croissance sous irradiation, la distribution en taille des nanoparticules doit être la plus étroite possible. Notre système modèle a été ensuite utilisé pour décrire l'évolution de la phase précipité par un mécanisme de mûrissement d'Ostwald dans un système ouvert limité par la diffusion. De plus, nous avons estimé la concentration seuil pour la germination, la tension de surface et la diffusivité de l'or sous irradiation. Pour conclure, les mécanismes de mûrissement d'Ostwald direct en inverse sous irradiation ont été étudiés dans les détails et les modèles existants testés expérimentalement.